EURAMET

Project Title

Comparison on material parameter measurements in the THz spectral range with optical, resonant and VNA based setups

Coordinator, Institute, Country

Alireza Kazemipour, METAS (Switzerland)

EURAMET Registration No.

1514

Subject Field

Electricity and Magnetism

KCDB Identifier

Date

2022-07-31

EURAMET project 1514: Comparison on material parameter measurements in the THz spectral range with optical, resonant and VNA-based set-ups

Djamel Allal[1], Uwe Arz[2], Gregory Gäumann[3], Andrew Gregory[4],
Martin Hudlička[5], Alireza Kazemipour[3], Thomas Kleine-Ostmann[2],
Gia Ngoc Phung[2], Přemysl Maršík[6], Mira Naftaly[4], Handan Sakarya[7],
Xiaobang Shang[4], David Ulm[2], Marcin Wojciechowski[8], Przemysław Zagrajek[9]

[1]Laboratoire national de métrologie et d'essais (LNE), France
[2]Physikalisch-Technische Bundesanstalt (PTB), Germany
[3]Federal Institute of Metrology (METAS), Switzerland
[4]National Physical Laboratory (NPL), United Kingdom
[5]Czech Metrology Institute (CMI), Czech Republic
[6]University of Fribourg (UniFR), Switzerland
[7]Ulusal Metroloji Enstitüsü (UME), Turkey
[8]Central Office of Measures (GUM), Poland
[9]Wojskowa Akademia Techniczna (WAT), Poland

25th July 2022

Glossary

CW	Continuous wave
DDS	Direct digital synthesizer
EM	Electromagnetic
FDS	Frequency-domain spectrometer
FPOR	Fabry-Perot open resonator
GRL	Gated-reflect-line (calibration method)
MCK	Material Characterization Kit
MUT	Material under test
NRW	Nicolson-Ross-Weir extraction method
TDE	Time-domain ellipsometry
TDS	Time-domain spectrometer
TEM	Transversal electro-magnetic (e.g. wave)
TPX	Polymethylpentene (trademark of Mitsui Chemicals Europe GmbH)
TRL	Through Reflect Line (calibration method)
UHMW	Ultra high molecular weight polyethylene
VNA	Vector network analyzer
YAG	Yttrium aluminium garnet ($Y_3Al_5O_{12}$)

Contents

1 Introduction **1**

2 Participants **1**

3 Traveling standards and measurement schedule **1**

4 Measurement quantities **1**

5 Measurement set-up and data analysis **2**
5.1 GUM set-up 2
5.2 LNE set-up 4
5.3 METAS 5
5.3.1 MCK set-up 5
5.3.2 FDS set-up 10
5.4 NPL 11
5.4.1 MCK set-up 11
5.4.2 TDS set-up 12
5.4.3 Open resonator set-up 13
5.5 PTB 15
5.5.1 MCK set-up 15
5.5.2 Free-space quasioptical system 16
5.6 UME set-up 17
5.7 WAT set-up 20
5.8 UniFR set-up 22

6 Results **24**
6.1 All materials measured using various methods 26
6.1.1 All materials measured using TDS method 26
6.1.2 All materials measured using VNA-based methods 33
6.1.3 All materials measured using open resonator-based methods 39
6.1.4 All materials measured using photonic-based methods 44
6.1.5 One material measured using all methods 51
6.2 Material Fused silica, all samples measured by one institute 75
6.3 Material UHMW polyethylene, all samples measured by one institute 80
6.4 Material doped silicon, both samples measured by one institute 85
6.5 Material AF32 Schott, both samples measured by one institute 88
6.6 Evaluation of measurement uncertainty 92

7 Discussion **99**

1 Introduction

This pilot study was part of the EMPIR (18SIB09) TEMMT project [1]. Therein, different methods for material parameter measurements in the THz spectral range were compared. The different measurement setups included photonic-based (TDS, FDS and TDE), resonant methods and VNA based systems, all of which have unique properties like e.g. spectral coverage. The comparison covered frequency range from approximately 20 GHz up to potentially several THz. The exact frequency range was left open and different systems have different frequency coverage. Part of the study was also to evaluate frequency limits of the different setups. A set of reference materials was measured by as many setups as possible. In addition, the measurements were analyzed with different material parameter extraction methods to study and compare different algorithms.

2 Participants

The list of participants is given in Table 1. There is a list of participants corresponding to the EMPIR TEMMT project activity (METAS, LNE, GUM, WAT, NPL), whereas other participants joined the comparison later (UME, PTB, UniFR). CMI helped to analyze results and prepare the comparison report. The list of setups used by participants is given in Table 2.

Acronym	**Institute**	**Country**
METAS	Federal Institute of Metrology	Switzerland
LNE	Laboratoire national de métrologie et d'essais	France
GUM	Central Office of Measures	Poland
NPL	National Physical Laboratory	United Kingdom
WAT	Wojskowa Akademia Techniczna	Poland
PTB	Physikalisch-Technische Bundesanstalt	Germany
UME	Ulusal Metroloji Enstitüsü	Turkey
UniFR	University of Fribourg	Switzerland

Table 1: List of institutes participating in the pilot study.

3 Traveling standards and measurement schedule

Each partner should have measured as many of the reference materials as possible. The aim was to compare the measured magnitude and phase of the transmission coefficient (S_{21}) and the extracted material parameters (dielectric function ε) measured using different setups. In addition, different material parameter extraction methods applied to the same transmission data were compared. The list given in Table 3 contains the complete set of reference materials for the pilot study. Specimens of fused silica and polyethylene have been cut from a single block. The measurement schedule is given in Table 4.

4 Measurement quantities

Each partner should report the dielectric permittivity (real and imaginary part) of the measured samples. The permittivity will be extracted from the measured data based on the method

Institute	Setup	Frequency range (GHz)
GUM	OR20	20
	OR40	40
	OR110	110
LNE	TDS	100 – 5000
METAS	MCK	500 – 750
	FDS	50 – 1200
NPL	MCK	144 – 220
	OR36	ca. 36 ± 1
	OR144	ca. 144 ± 1
	TDS	100 – 5000
PTB	VNA quasi-optical FS1	50 – 75
	VNA quasi-optical FS2	75 - 110
	VNA quasi-optical FS3	110 - 170
	VNA quasi-optical FS4	140 - 220
	MCK01	67 – 110
	MCK02	110 - 170
UME	VNA free-space, quasi-optical	67 - 170
UniFR	ellipsometer	100 - 2500
WAT	TDS 1	100 – 5000
	TDS 2	100 – 5000

Table 2: List of measurement methods employed by particular institutes.

used (VNA-based MCK or free-space quasioptical, resonant, TDS, FDS, open resonator, ellipsometry). Expanded measurement uncertainties ($k = 2$) should be given for the extracted material parameters. If available, the uncertainties of the absolute value and phase of the transmission can be added.

5 Measurement set-up and data analysis

5.1 GUM set-up

The Fabry-Perot open resonator (FPOR) was used for wideband accurate measurement of the dielectric constant and loss tangent in the range of frequency from 20 GHz to 110 GHz. The FPOR was connected to a vector network analyzer (VNA) which measured the transmission coefficient S_{21}. Frequency expanders can be used for frequencies above 50 GHz, see Figure 1. Due to coupling with spurious modes that slightly alter resonant frequencies of the measured modes, the thickness of the sample of known dielectric constant is limited as shown in the Figure 1(c).

The dielectric parameters of the samples can be calculated using following equations. Assuming the relative permittivity is expressed as $\varepsilon_r = \varepsilon_r' + j\varepsilon_r''$, we can write

$$\varepsilon_r' = 1 + \frac{V}{\alpha \Delta V} \frac{f_0 - f_S}{f_0}, \tag{1}$$

$$\varepsilon_r'' = \frac{V}{2\alpha \Delta V} \left(\frac{1}{Q_l} - \frac{1}{Q_e} \right), \tag{2}$$

Sample	Name	Shape/size (mm)	Thickness (μm) $\pm 2\sigma$
1	High-resistivity silicon	⌀100	416.2 ± 2.2
2A1a	Fused silica,	⌀80	2068 ± 4
2A1b	batch A	⌀80	2056 ± 8
2A2a		⌀80	1016 ± 6
2A2b		⌀80	1034 ± 4
2A3a		⌀80	523 ± 10
2A3b		⌀80	520 ± 8
2A4a		⌀13	1968 ± 3
3	Borofloat	⌀100	500.6 ± 0.1
4	TPX	⌀100	6146.5 ± 16.4
5	YAG	⌀60	2504 ± 8
6a	UHMW Polyethylene	⌀80	1850 ± 40
6b		⌀80	4967 ± 6
6c		⌀13	1995 ± 22
6d		75 x 54	1815 ± 14
7a	Doped silicon	⌀100	290.8 ± 0.9
7b		⌀100	595.9 ± 3.4
8a	AF32 Schott	⌀100	501 ± 1
8b		⌀100	502 ± 3
9	HR Si etalon	⌀50	3065.7 ± 3.7

Table 3: List of specimens used in the pilot study.

	GUM	LNE	METAS	NPL	WAT	PTB	UME	UniFR
Oct 2020	X				X			
Nov 2020	X				X			
Dec 2020			X					
Jan 2021			X	X				
Feb 2021				X				
Mar 2021		X						
Apr 2021		X						
May 2021						X		
Jun 2021						X		
Jul 2021						X		
Aug 2021							X	
Sep 2021							X	
Oct 2021								X

Table 4: Measurement schedule.

$$\varepsilon_r' = \varepsilon_{r0}' - \frac{f_0 - f_S}{At}, \tag{3}$$

$$\tan\delta = \frac{\varepsilon_r''}{\varepsilon_r'}, \tag{4}$$

where V is the volume of cavity, α is the constant determined by resonance mode, ΔV is the volume of the sample, f_0 is the empty resonator resonant frequency, f_S is the resonant frequency with specimen, $f_0 - f_S$ is the shift frequency, Q_l is the Q–factor for resonator loaded with a

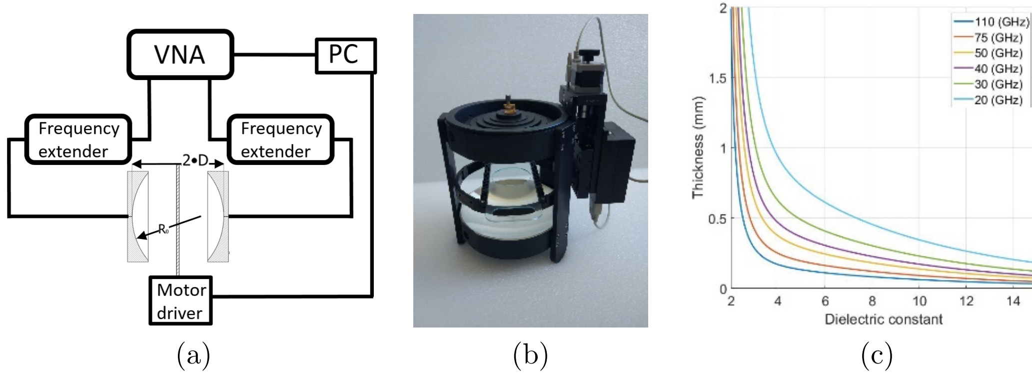

Figure 1: (a) Measurement system with FPOR connected to VNA via frequency expanders. Motor moves the sample to the optimal position, (b) FPOR appearance, (c) limitation.

sample, Q_e is the Q–factor for empty resonator, ε'_{r0} is the relative complex permittivity of empty resonator, A is a scaling factor, t is the thickness of the sample, $\tan\delta$ is the loss tangent. The measurement uncertainty of the real part of the relative permittivity consists of two main components: the uncertainty of the sample thickness and the uncertainty of frequency. The latter is often about a thousand times smaller than the former and can be omitted. The measurement uncertainty of the loss tangent is an order of magnitude greater than the uncertainty of the permittivity because it contains a greater number of measurement uncertainty elements related to the VNA itself.

5.2 LNE set-up

LNE used the TDS system, model TERA K15 from MenloSystems. This system is based on a fibre-coupled configuration and is designed for operation with laser at wavelength around 1.5 μm. Its flexibility allows the THz path to be positioned outside the spectrometer housing, if needed. The block diagram of the TDS is shown in Figure 2. It includes a femtosecond laser source (T-Light), a fibre coupled optical light path with delay line (ODU), THz wave path with linearly polarized THz photoconductive antennas, emitter and detector, and THz optics, lock-in detection electronics, and data acquisition for material parameters extraction.

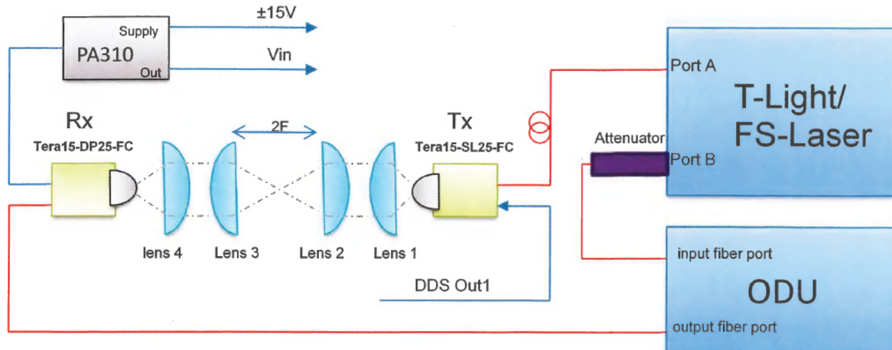

Figure 2: Commercial TDS solution, model TERA K15, from MenloSystems (LNE).

The diagram shows 4 lenses to allow for a focal point to be generated. However, for the measurements in the framework of the TEMMT project [1], lenses 2 and 3 have been removed

to use a collimated THz beam. An adjustment of the antennas positioning was necessary to relocate the THz pulse in the time domain available observation window, as the optical length is initially adjusted by the manufacturer to be used with the four lenses. The DDS allows to generate stable high voltage signals (sine or square waveforms) for lock-in detection, and the PA310 is a kHz range transimpedance amplifier with a factor of 107 V/A. A photograph of the TDS in use with a material sample is shown in Figure 3.

Figure 3: Photograph of the Menlo Systems TERA K15 (LNE).

For the extraction of the material parameter, a reference pulse with an empty THz TDS system and a sample pulse with the sample in the THz beam path are measured. The ratio of the corresponding Fourier spectra obtained by Fourier transform yields the measured transfer function. The thickness and frequency-dependent complex refractive index, and so complex permittivity, of the sample are then calculated in a numerical optimization, by minimizing the difference between the measured and the theoretical transfer function, using an implementation of the Nelder-Mead simplex algorithm.

5.3 METAS

5.3.1 MCK set-up

Measurement results are based on non-contact free-space techniques by using VNA and the associated frequency extensions for the band 500–750 GHz. Non-magnetic materials with relative permeability $\mu_{\mathrm{r}} = 1$ are assumed. The quasioptical device here is a commercially available mode-convertor (Swissto12@ MCK; set of two corrugated horn antennas). The system is supposed to convert waveguide propagation modes to TEM free-space mode on its aperture where the MUT is installed. METAS has been working on the setup optimization and in-depth study of its electromagnetic characteristics (propagation modes, matching, losses, aperture/gap scattering, etc.) and the system calibration. The study of the setup and its optimization is mainly based on theoretical and experimental works of transmission-only extraction methods, whereas both the VNA calibration and the associated frequency extender optimization are performed to minimize the uncertainties of the input parameters (S_{21}, amplitude, and phase). The measurement setup is depicted in Figure 4 and Figure 5.

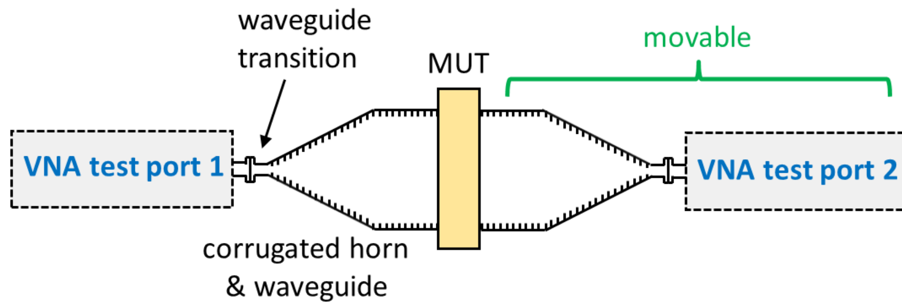

Figure 4: Measurement setup of the MCK.

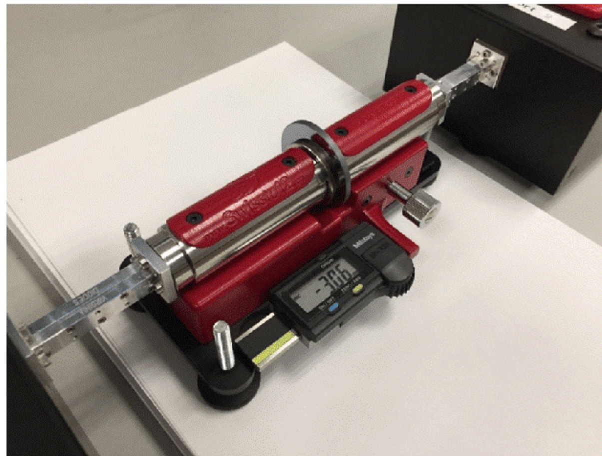

Figure 5: MCK connected to the VNA frequency extension modules with the material under test clamped between the two antennas apertures.

Following text summarizes the procedure for material parameters extraction of METAS. Fabry-Pérot equations describe the S-parameters of MUTs as a function of T and Γ. This is based on multiple reflection and transmission though the material-slab, see Figure 6.

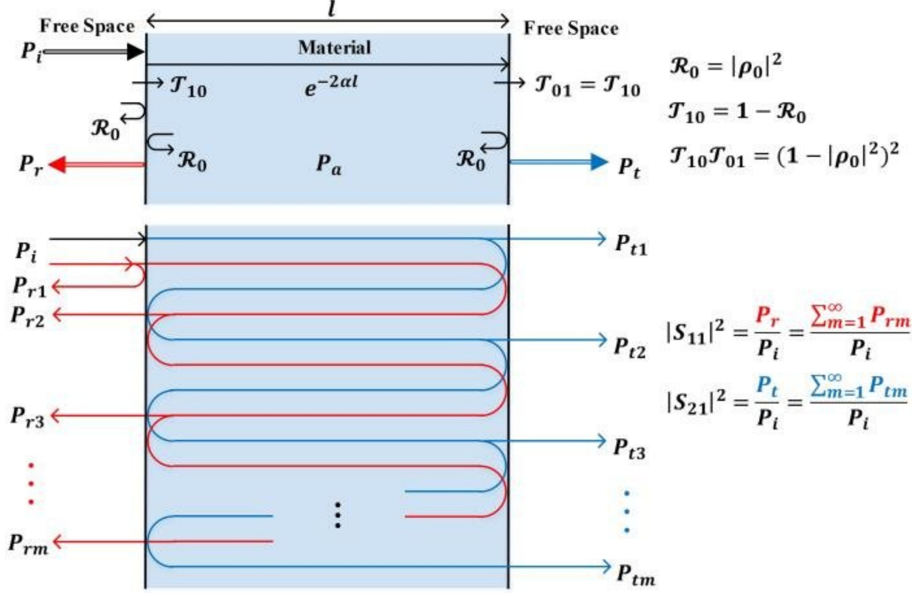

Figure 6: Fabry-Perot oscillations in the material.

Reflection (S_{11}, S_{22}) and transmission (S_{21}, S_{12}) data can be processed to obtain real and imaginary parts of both permittivity ε and permeability μ of the MUT. Various iterative and non-iterative algorithms have been presented for this goal [2], [3], [4]. The classic Nicolson-Ross-Weir (NRW) method [2] deals with Γ and T (see (5), (6) for free-space propagation) to extract ε and μ, simultaneously. The method gives unstable results for low-loss and high-refractive materials when $S_{11} \approx 0$ and $|S_{21}| \approx 1$ at specific frequencies.

$$S_{11} = \frac{\Gamma\left(1 - T^2\right)}{1 - \Gamma^2 T^2}, \tag{5}$$

$$S_{21} = \frac{T\left(1 - \Gamma^2\right)}{1 - \Gamma^2 T^2}. \tag{6}$$

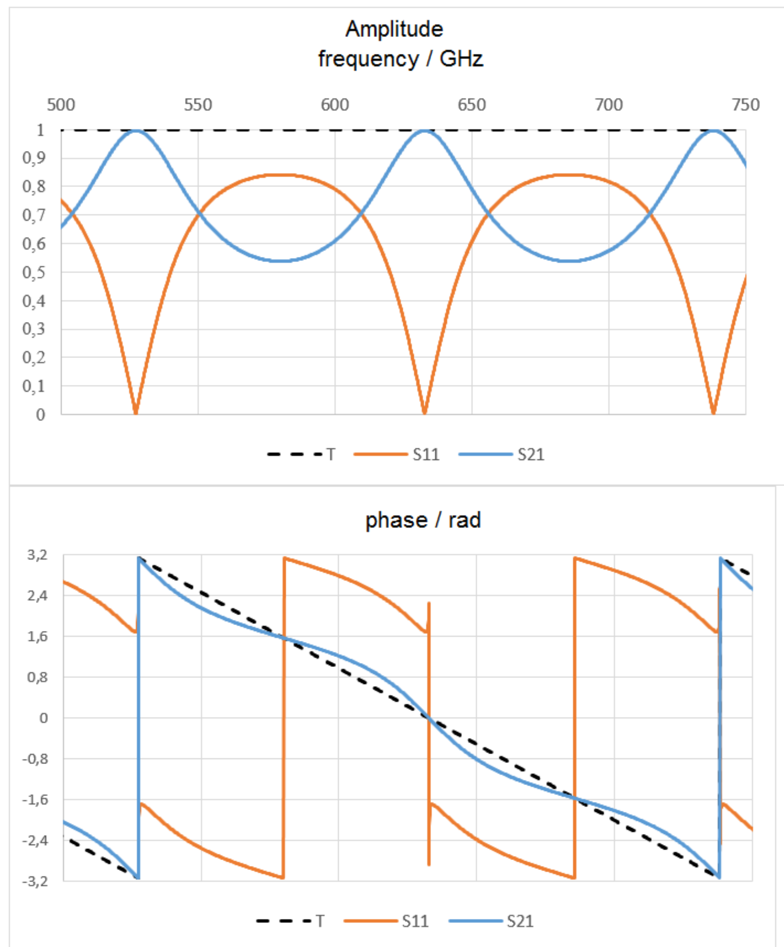

Figure 7: Example (theory) of S_{11}, S_{21} and T of a very low-loss slab: Silicon HRSi with thickness 0.4 mm.

The theoretical curves for a silicon slab are shown in Figure 7, and the realistic case for extracting of T from S_{21} is shown in Figure 8 and Figure 9. Note that only the transmission parameter S_{21} is used for non-magnetic materials.

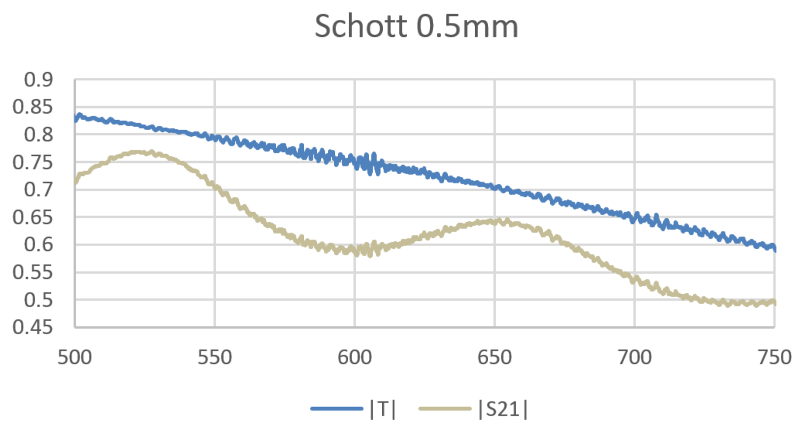

Figure 8: Example of extracted T from S_{21} for a Schott glass (500-750 GHz).

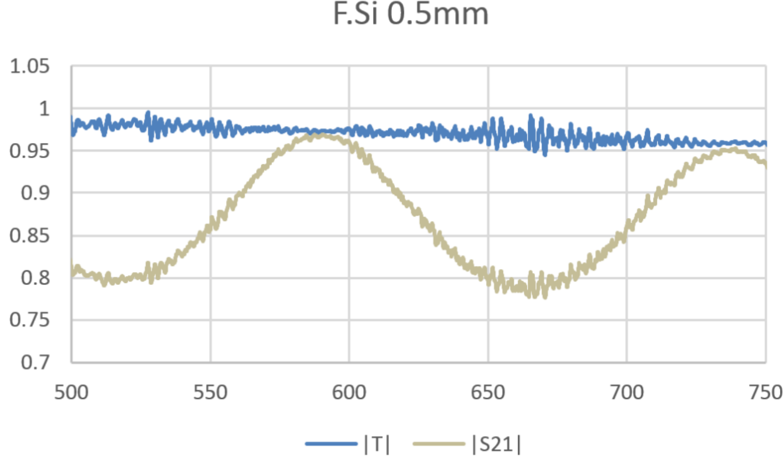

Figure 9: Example of extracted T from S_{21} for a Fused-Silica (500-750 GHz).

The transmission-only method utilizes S_{21} (or S_{12}) parameter on the material slab to derive T and consequently, to extract the permittivity $\varepsilon_r = \varepsilon_r' - j\varepsilon_r''$. The transmission coefficient T is a function of the material thickness d and its permittivity and permeability. For free-space propagation, we can write

$$T = \exp\left(-j\frac{\omega}{c}d\sqrt{\mu_r\varepsilon_r}\right). \tag{7}$$

For the materials which are not very lossy ($\varepsilon_r''/\varepsilon_r' = \tan\delta < 0.1$), T can be separated directly into phase and magnitude parts [5] as follows

$$T = \exp\left(-j\frac{\omega d}{c}\sqrt{\varepsilon'}\right)\exp\left(-\frac{\omega d}{2c\sqrt{\varepsilon'}}\varepsilon''\right). \tag{8}$$

This means the phase and magnitude of T give real and imaginary parts of permittivity, consequently

$$\angle(T) = \angle\left[\exp\left(-j\frac{\omega d}{c}\sqrt{\varepsilon'}\right)\exp\left(-\frac{\omega d}{2c\sqrt{\varepsilon'}}\varepsilon''\right)\right] = -\frac{\omega d}{c}\sqrt{\varepsilon'}, \tag{9}$$

$$\ln(T) = \ln\left[\exp\left(-j\frac{\omega d}{c}\sqrt{\varepsilon'}\right)\exp\left(-\frac{\omega d}{2c\sqrt{\varepsilon'}}\varepsilon''\right)\right] = -\frac{\omega d}{2c\sqrt{\varepsilon'}}\varepsilon''. \tag{10}$$

The phase $\angle(T)$ can be evaluated from $\angle(S_{21})$ easily if the material is not very lossy [6].

$$\angle(T) = \angle(S_{21}) = \frac{n\pi}{2}. \tag{11}$$

It can be shown that at $n\pi$ points the uncertainty, i.e. the sensitivity coefficient, is minimum in the transmission-only method [6]. If we use the transmission-only extraction method, the sample thickness d has very important contribution to the final uncertainty of ε_r', however, the uncertainty factor is $\Delta d/d$, not only Δd. That means the same absolute thickness uncertainty can affect less thicker slabs' ε_r', in general. As for the imaginary part ε_r'', the uncertainty Δd does not have, in general, an important contribution to final result.

5.3.2 FDS set-up

This setup is based on a commercial system which uses photomixers and two CW lasers to generate and detect CW THz radiation (Figure 10). The traceability is established by measuring the optical frequencies of the two CW lasers with a reference wavemeter. Test measurements of different materials have been performed to further improve the setup performance. METAS have precisely defined how each spectrometer should be characterized and have successfully applied different methods for material parameter extraction.

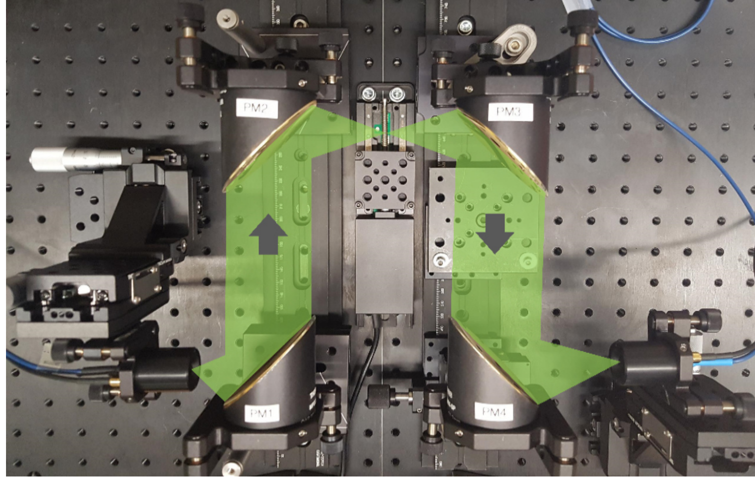

Figure 10: THz frequency-domain spectrometer. Black cylinders are photomixers, green area indicates THz path which is guided via parabolic mirrors.

The alignment of the free-space spectrometer was optimized, as well as the instrument control software and the material parameter extraction methods. Further, calibration artefacts for the frequency scale as well as for the linearity of the amplitude scale have been purchased and measured. From the complex transmission data and the previously determined specimen thickness values, the material parameters have been extracted via the standard method for all materials. In this standard method the Fresnel transmission coefficient equation is inverted to get the complex refractive index. From the complex refractive index all other material properties like the permittivity or the absorption coefficient can be determined. Some results of system testing (power and transmission) are shown in Figure 11 and Figure 12.

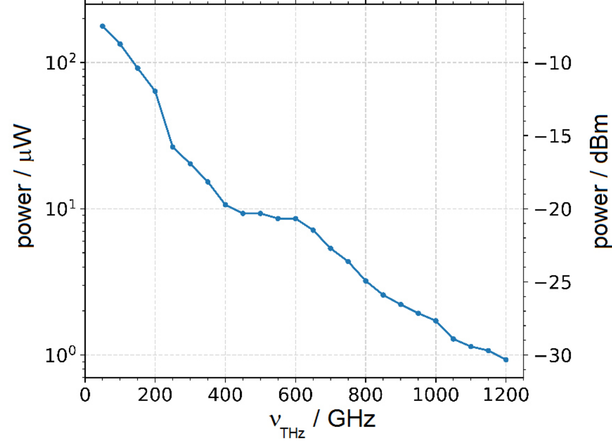

Figure 11: Optical power output in dependence of THz frequency of the optical synthesizer.

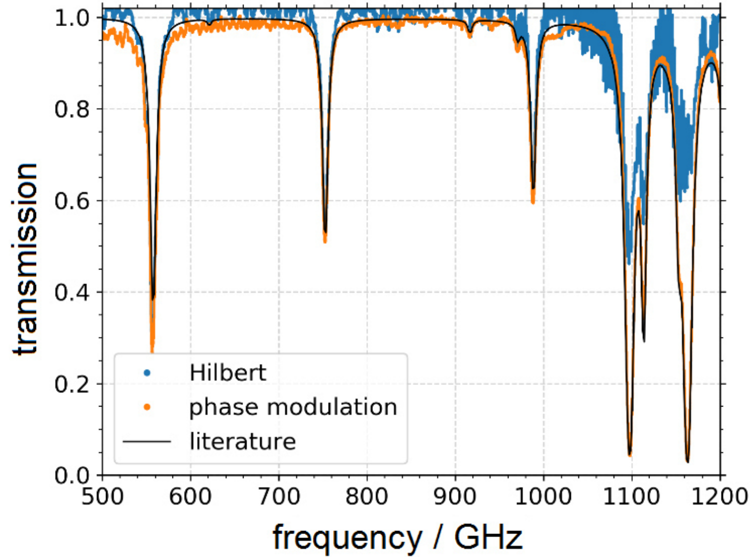

Figure 12: THz field transmission through humid air determined by the Hilbert transform method and the phase modulation method. Literature data from simulations is taken from [2] and the assumed path length is optimized for the best fit to the measured data.

5.4 NPL

5.4.1 MCK set-up

The MCK system of NPL uses a gated-reflect-line (GRL) calibration technique that is carried out at the ends of the antennas prior to making measurements of S-parameters. The GRL method requires a simple zero-length "Thru" standard and a metallic reflecting plate as the "Reflect" standard. The "Thru" standard is realized by closing the gap between the two halves of the corrugated antennas. The "Reflect" standard is realized by placing a short circuit (a 1 mm-thick metal shim, provided with the MCK) between the two halves of the antennas. Time-domain gating, a useful technique for free-space measurements, is employed here to separate the wanted signals from the spurious reflections generated elsewhere in the measurement system (e.g., due to the connections between the MCK and the test ports of the VNA, and so on). A dedicated

software is supplied with the MCK for data analysis, which allows computation of the dielectric constant and loss tangent directly from measured S_{11} and S_{21} (or S_{22} and S_{12}). In addition, a well-known algorithm (NIST precision model) has been used to calculate the dielectric constant and loss tangent of several materials. It was shown that results extracted using the MCK software agree extremely well with those extracted using the NIST precision model [7].

To assess and quantify the effect of sample thickness on the extracted ε' and tanδ, the thickness utilized in extraction is slightly varied. The study was carried out on Sample 6b (the UHMW polyethylene sample with the thickness of 4.970 mm). It was found that a small variation in thickness used for extracting produces a significant change in the extracted ε' and tanδ. Specifically, a deviation from -20 μm to +20 μm ($\pm$4 %) of the thickness used in extraction brings a significant decrease of the value of extracted ε', centred at 2.273 (falling from +8.5 % to -7.6 %) and an increase in tanδ, centred at 0.0011 (rising from -9.9 % to +9.1 %). This indicates that sample thickness plays an important role in the extracted material properties at millimetre-wave frequencies and should be measured as accurately as possible. Non-ideal sample flatness could contribute significantly to the uncertainty of the measurement of extracted material properties.

5.4.2 TDS set-up

Terahertz time-domain spectroscopy (THz TDS) measurements were carried out using a Tera-Flash Pro spectrometer from Toptica Photonics set up in a standard optical configuration with four $F/2$ parabolic mirrors, see Figure 13. The THz beam path was purged with dry air to eliminate absorption from atmospheric water vapor. Samples were placed in the collimated section of the beam, and laser alignment was used to ensure that they were positioned normal to the THz beam. The frequency resolution was 10 GHz.

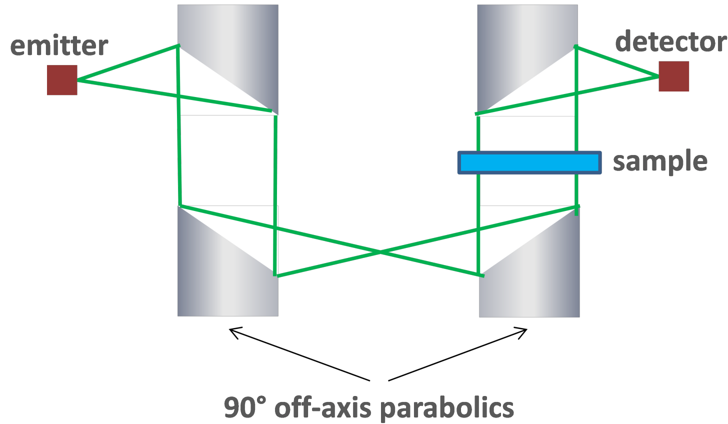

Figure 13: THz beam path for TDS measurements (NPL).

Fourier transform was applied to the time-domain data to obtain the frequency-dependent field amplitude ($E\,(f)$) and phase ($\phi\,(f)$), see Figure 14.

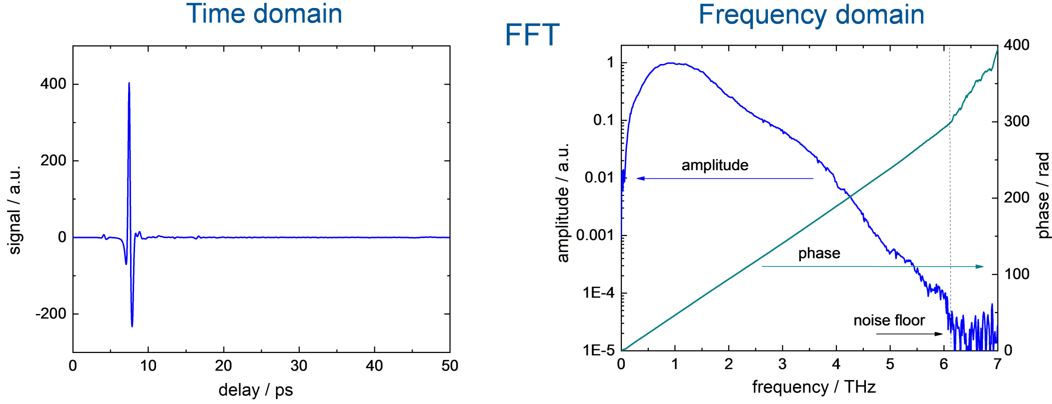

Figure 14: Time-domain data from the instrument (left); the frequency-dependent amplitude and phase calculated by applying FFT (right).

The frequency-dependent (f) refractive index $(n(f))$ and absorption coefficient $(\alpha(f))$ of each sample were calculated using the standard equations

$$n(f) = 1 + \frac{(\phi(f) - \phi_{ref}(f))\,c}{2\pi f d}, \tag{12}$$

$$\alpha(f) = -\frac{2}{d}\ln\left[\frac{(n+1)^2}{4n}\frac{E_s(f)}{E_{ref}(f)}\right], \tag{13}$$

where c is the speed of light, d is the sample thickness, and the subscripts s and ref refer to the sample and reference data, respectively. THz TDS has an important advantage in measurements of THz optical properties of materials, in that it enables unambiguous, straightforward determination of refractive index and absorption coefficient.

The measurement uncertainty had two main components: uncertainty in sample thickness; and measurement repeatability. Sample thickness was measured 10 times with a calibrated micrometer; the mean value was used in calculating the absorption coefficient and refractive index, and standard deviation was used in calculating the uncertainty. Each sample was measured 4 times, each time removing it from the beam path and replacing it. The mean of measurements was used in calculating the absorption coefficient and refractive index, and standard deviation was used in calculating the uncertainty.

5.4.3 Open resonator set-up

Permittivity and loss tangent were extracted by measurement of the Q-factor and frequency of resonances of plano-concave open resonators (Figure 15) that operate at approximately 36 GHz and 144 GHz. For the TEMMT project, specimens of fused quartz and UHMW polyethylene were measured. During each experiment, additional measurements were made on reference specimens (single-crystal quartz at 36 GHz, and YAG at 144 GHz) to demonstrate that the instrumentation and software were operating correctly. Both resonators are of similar design, and use coupling holes in the concave mirror to excite Gaussian-beam mode resonances. Historically, Klystron-based detection systems were used to measure the Q-factor and frequency of resonances. In the TEMMT project, these quantities were fitted [8] to measurements of complex transmission coefficient (S_{21}) made with a Vector Network Analyser (VNA). High Q-factors are obtained (over 100 000 for the empty resonators) and, in consequence, very low losses can be measured.

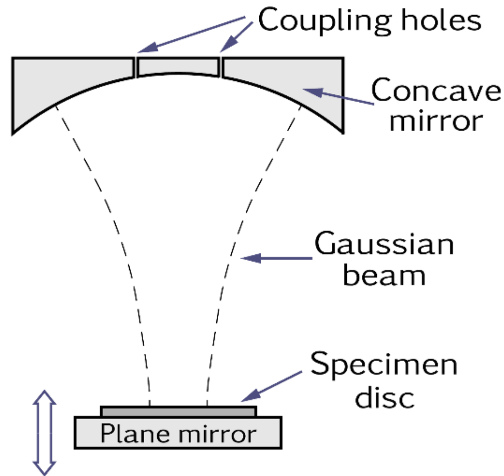

Figure 15: Schematic of plano-concave open resonator.

Open resonators resonate at a number of axial resonant modes (the axial mode number is the number of half wavelengths between the mirrors). The cavity can be tuned to a particular resonance by changing the frequency, or by adjusting the cavity length by using the micrometer that supports the plane mirror. In addition to the fundamental TEM_{00} axial modes used for measurement, higher-order modes are also present. Therefore, a procedure to identify the fundamental axial modes is always needed prior to measurements. This makes use of the fact that the wavelength of higher order modes differs slightly from that of the fundamental. It is observed that the number of higher-order-modes that are excited can be reduced by increasing the length of the cavity.

There are two possible methods of using open resonators: The fixed-frequency equivalent-length method used for many years at NPL [9], and the variable-frequency fixed-length method [10] which was implemented at NPL during the TEMMT project. Measurements were made by both techniques were in good agreement. The presence of higher-order modes is always an issue because they may coincide with fundamental modes, which causes error in measured Q-factors. Measurements were made at a few axial modes to allow erroneous measurements to be identified and excluded.

For plano-concave open resonators, the lowest uncertainties are obtained when specimens are a multiple of half a wavelength thick in the medium of the material. It is well-established that specimens with a length of a few half wavelengths can be measured. Thin polymer specimens are difficult to measure because they tend to become dished or warped, resulting in air gaps beneath them and the plane mirror. This was an issue for the TEMMT UHMW polyethylene specimens, particularly at 144 GHz. The technique can be used to measure two tensor components of permittivity and loss tangent for uniaxial anisotropic materials because the Gaussian beam is plane-polarised. This is achieved by rotating specimens. If the tensor components are not aligned ($0°$ or $90°$) with the E-field then mode splitting can occur. Such mode splitting, however, can also occur if the specimen is warped (Figure 16).

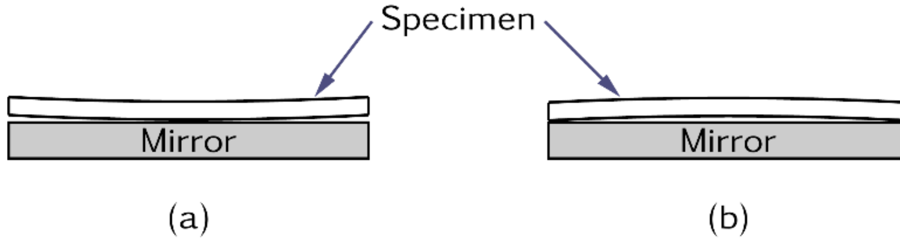

Figure 16: A dished specimen. When the specimen is in contact with the centre of the mirror as shown in (a), measurements are more accurate results than when there is an air gap, as shown in (b).

5.5 PTB

5.5.1 MCK set-up

Two different material characterization kits (MCKs) were used, one for the WR10 frequency range (67-110 GHz according to the manufacturer), and one for the WR06 frequency range (110-170 GHz). Useful results could be obtained in the frequency ranges 70-105 GHz for the WR10-MCK and 105-170 GHz for the WR06-MCK, respectively.

For the calibration a two-tier approach was employed. The first-tier calibration (TRL) was performed in the respective waveguide band, setting the reference plane at the waveguide flanges. Then, a second-tier (multiline) TRL calibration [11] using the implementation details of [12] was performed in the MCKs. Similar to TRL, multiline TRL (mTRL) offers high accuracy and needs only minimal knowledge of the standards used. Additionally, it helps to avoid the bandwidth limitations of TRL and provides higher accuracy over a wider frequency range. The Thru standard was realized by connecting the two antennas directly, and the Short standard made use of the shorting plate provided by the manufacturer. The reference planes of the mTRL calibration were defined at the MCK flanges, i.e. directly at the end of the corrugated waveguides. In our newly developed method, instead of the corrected S-parameter measurements of the samples, the propagation constant determined by multiline TRL was used to extract the dielectric material parameters. As the single-mode propagation assumption in multiline TRL is not fulfilled in the entire frequency range, the propagation constant exhibits artifacts at certain frequencies. Therefore, to avoid time-domain gating, post-processing steps including outlier rejection and filtering were applied in the frequency domain. Details of the procedure will be given in a separate publication.

The results for the complex permittivity are shown in Figure 17 for a selection of three UHMW polyethylene samples in the WR06 band. For the first time, all available samples thicknesses could be combined to give a better result than the measurements from the individual thicknesses. Due to the multiline algorithm, the uncertainties in the extracted dielectric material parameters are reduced in comparison to the individual sample measurements. Also, some of the peculiarities occurring for individual samples at certain frequencies (see, e.g., relative permittivity measurement of Sample 6a at 160 GHz) are significantly mitigated due to the multiline process. The preliminary uncertainty estimates contain contributions from the sample thicknesses, from the waveguide calibration standards involved in the first-tier calibration, from the VNA instrumentation and from the sample insertion repeatability.

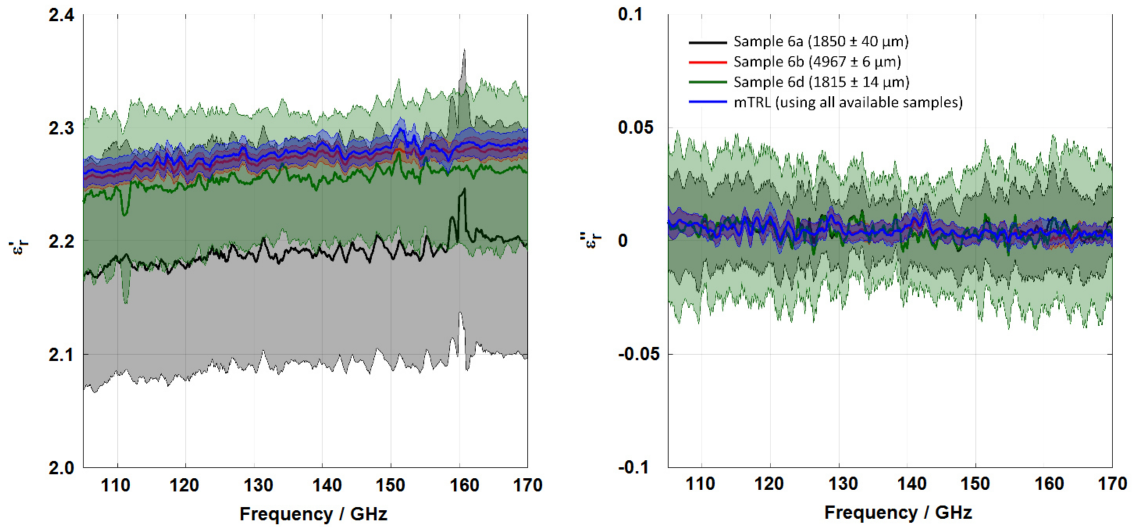

Figure 17: Dielectric parameter extraction results (solid lines) and expanded uncertainties (shaded areas, $k = 2$) of the newly developed MCK extraction method for three individual thicknesses of UHMW polyethylene and for the multiline combination of these thicknesses.

5.5.2 Free-space quasioptical system

Both the measurement setup and the extraction algorithm of the quasi-optical material characterization setup used at PTB are described in detail in [5]. Figure 18 shows a drawing of PTB's quasi-optical measurement system. With the help of a commercially available VNA setup (consisting of a VNA and two mm-wave converters), the transmission coefficient of a material sample is determined when being excited with a plane wave. Here, 90° off-axis parabolic mirrors are used to reduce the overall size of the system and to achieve a plane wave condition at the samples' location.

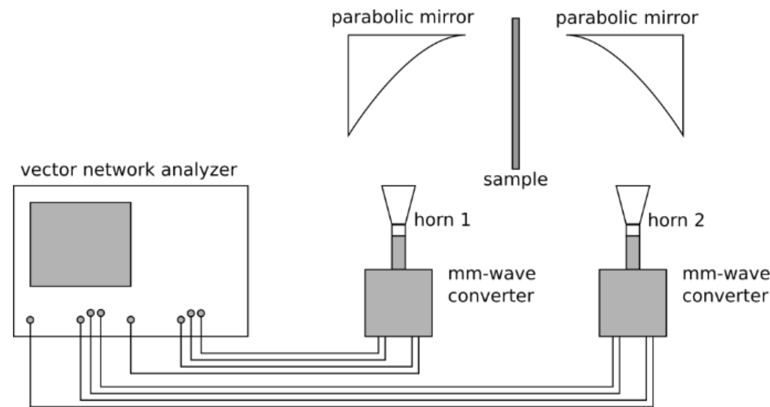

Figure 18: Drawing of the quasi-optical setup (PTB).

The calibration of the measurement-system is done in a two-tier approach: First, a full system error correction is performed, placing the reference planes at the feed points of the horn antennas, and then the transmission factor of the empty system is measured, allowing the reference planes to be shifted to the samples surfaces. Time gating is used to reduce the effect of unwanted reflections inside the measurement setup. After finishing the measurement, the

algorithm presented in [5] is used to determine the (complex-valued) relative permittivity of the material sample. The big advantage of this algorithm is that only the transmission factor and the sample thickness are required for the material parameter extraction. Due to the underlying principle, this algorithm is only suitable for the characterization of low-loss dielectrics.

5.6 UME set-up

UME used a free space measurement setup with VNA and horn antennas for the 67 GHz – 115 GHz and 110 GHz – 170 GHz frequency band. Measurement were performed at two different antenna distances.

- Measurements performed very close to each other (0 cm for both frequency bands),
- Measurements performed at the Fresnel distance (20 cm for WR10, 10 cm for WR6.5).

Measurements for each frequency band were performed first in the absence of samples and then by positioning the samples in the middle of the antennas. Schema of the measurement setup is given in Figure 17.

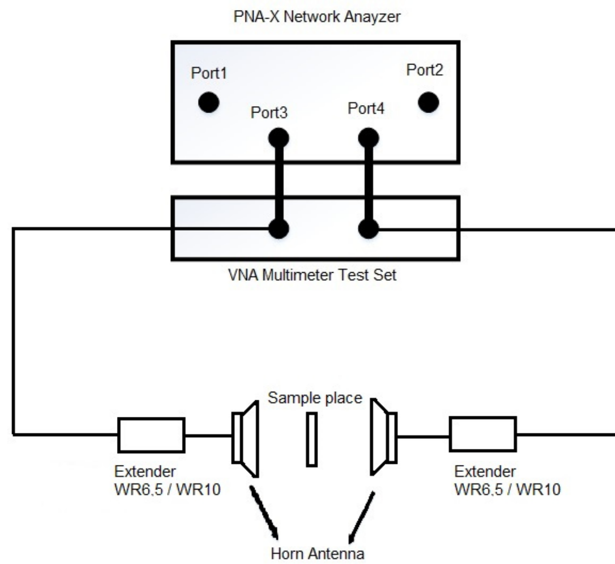

Figure 19: Drawing of the measurement setup (UME).

The list of the equipment used at the measurement setup is given below.

- Keysight N5247B PNA-X Network Analyzer
- Keysight N5292A VNA Multimeter Test set
- VDI Extender WR6.5 110-170 GHz Model VNAX
- VDI Extender WR10 65-115 GHz Model VNAX
- VDI 6.5 VNAX Calibration Kit N5262AC06

– VDI 10.0 VNAX Calibration Kit N5262AC10

– Horn antennas for 65-110 GHz frequency band

– Horn antennas for 110-170 GHz frequency band

The data measured by UME suffer from bad VNA calibration and thus the extracted permittivity values are not reliable and comparable to other participants. TRL calibration was performed, however, most probably the measurement reference plane was wrong which resulted in wrong measured S-parameters. Due to the measurement schedule, it was not possible to repeat the measurements. UME requested to exclude their data from the comparative graphs of the pilot study. Figures 20 to 26 show several examples of the extracted dielectric constant for illustration.

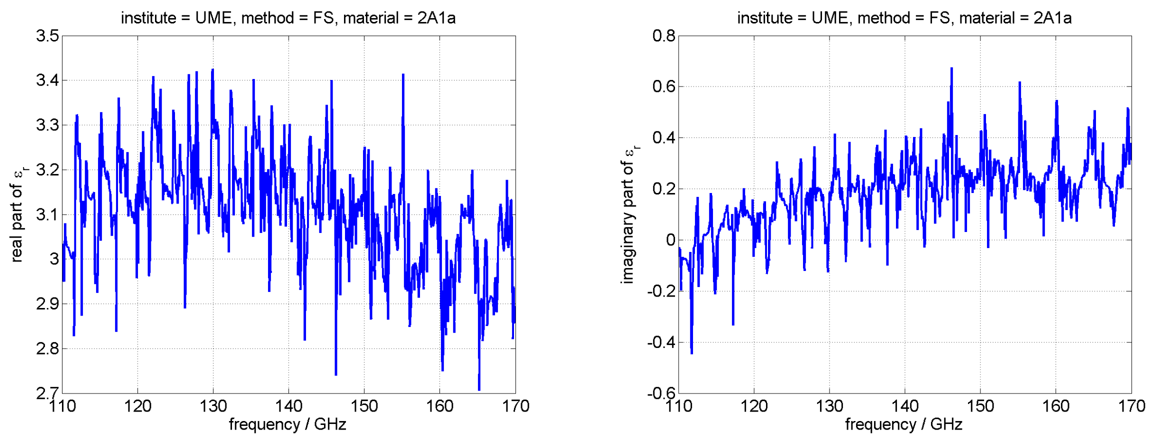

Figure 20: UME FS 2A1a (real + imaginary part of ε_r) 0cm WR65.

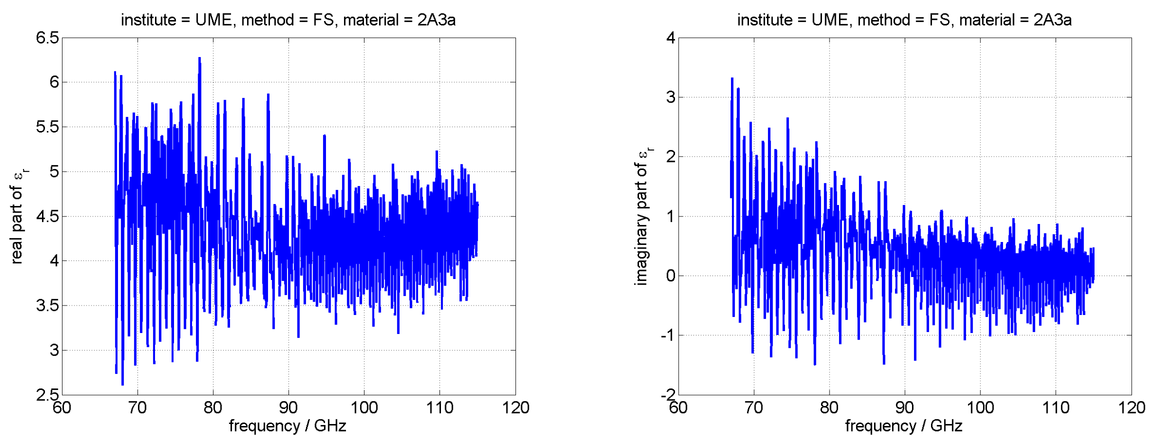

Figure 21: UME FS 2A3a (real + imaginary part of ε_r) 20cm WR10.

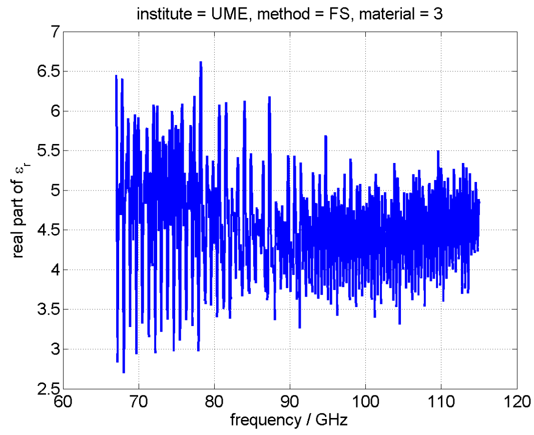

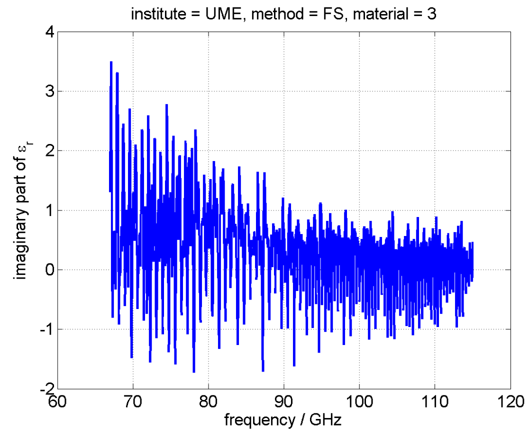

Figure 22: UME FS 3 (real + imaginary part of ε_r) 20cm WR10.

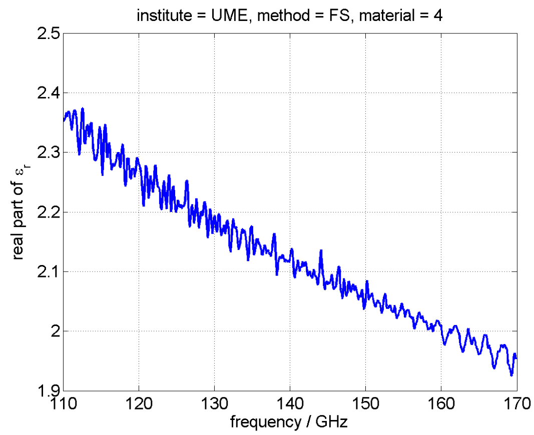

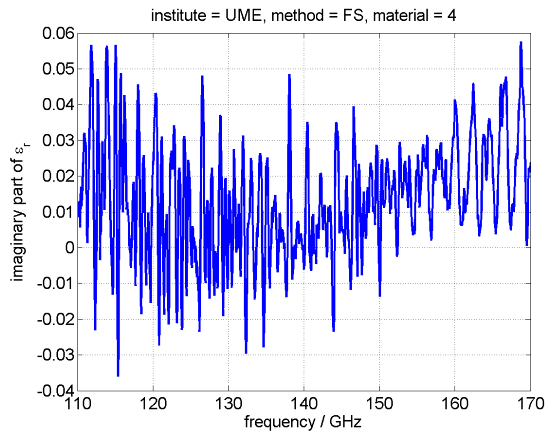

Figure 23: UME FS 4 (real + imaginary part of ε_r) 10cm WR65.

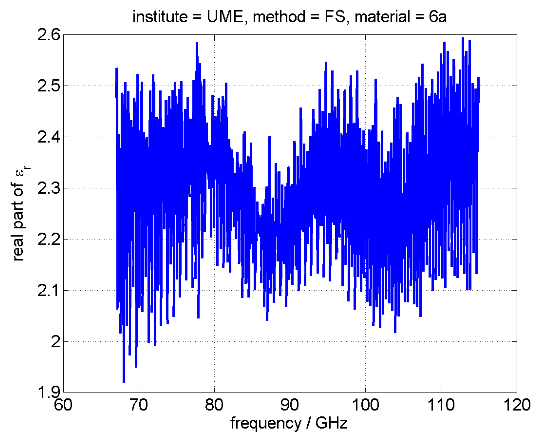

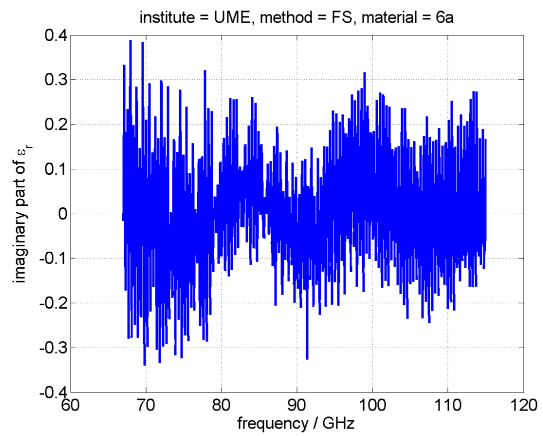

Figure 24: UME FS 6a (real + imaginary part of ε_r) 20cm WR10.

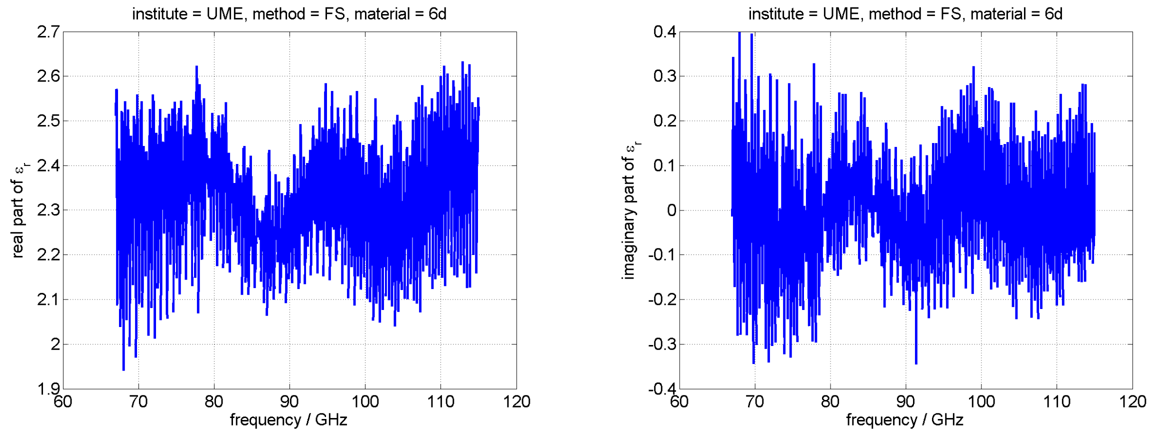

Figure 25: UME FS 6d (real + imaginary part of ε_r) 20cm WR10.

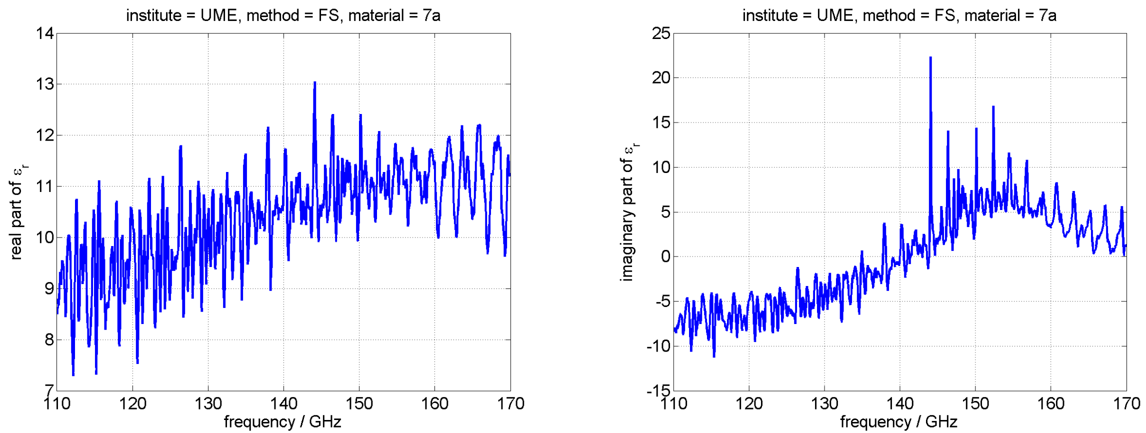

Figure 26: UME FS 7a (real + imaginary part of ε_r) 10cm WR65.

5.7 WAT set-up

WAT used the commercial TPS spectra 3000 system from TeraView company (TDS). All measurements were done in the chamber with dry air. The photograph of the system is shown in Figure 27 and the scheme of a measurement setup is shown in Figure 28.

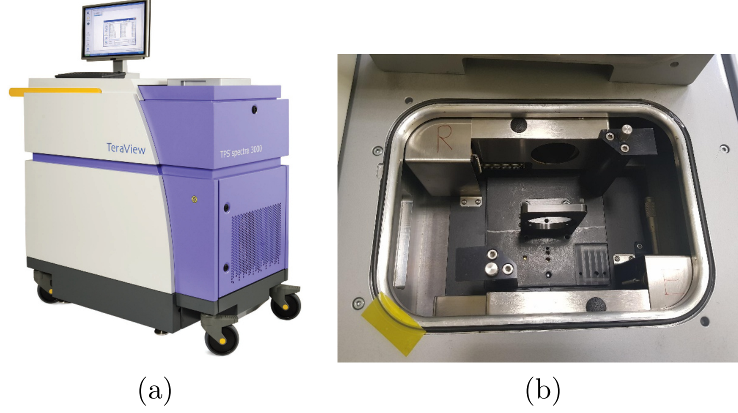

(a) (b)

Figure 27: General view of the TPS spectra 3000 system (a) and the sample chamber (b).

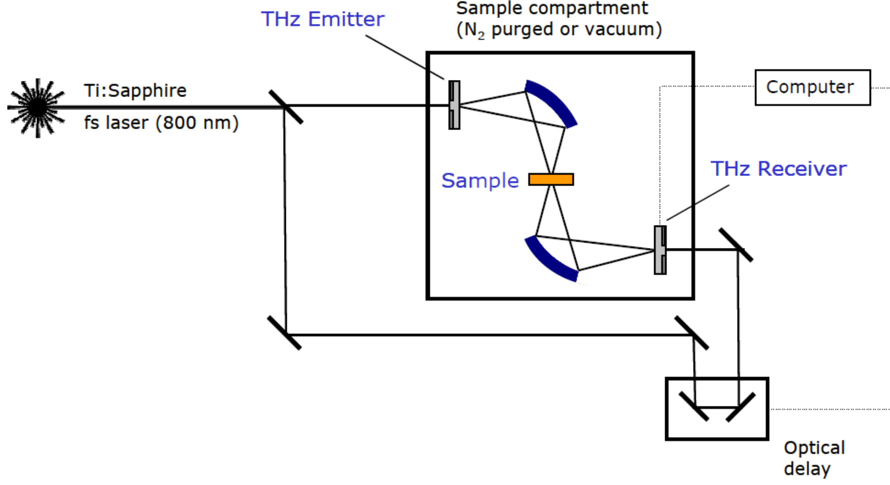

Figure 28: The scheme of measurement setup of the TPS spectra 3000 system.

In the TDS method the signal in time domain is acquired. The frequency (f) is calculated by a firmware by Fourier transform. As a reference the empty setup is measured, next the measurement with the same parameters is performed with sample inserted into the chamber. Collected values are transmission - $T(f)$ and phase difference $\varphi(f)$. The phase difference is linearized by firmware but does not start exactly form "0" point. Additionally, it was shifted manually to start from "0" for frequency $f = 0$. The values of refractive index $n(f)$, dielectric constant $(\mathrm{Re}(\varepsilon),\ \mathrm{Im}(\varepsilon))$ could be calculated by firmware if the sample with thickness L is inserted. The values of refractive index and dielectric constant were calculated from equations:

$$n(f) = \frac{c\phi(f)}{2\pi f L} + 1, \tag{14}$$

$$\kappa(f) = \frac{c}{2\pi f L} \ln\left[\frac{1}{|T(f)|}\frac{4n(f)}{(n(f)+1)^2}\right], \tag{15}$$

where c is the speed of light, $\varepsilon' = n^2 - \kappa^2$, $\varepsilon'' = 2n\kappa$. As visible in Figure 28, the incident beam is convergent. Nevertheless, the Gouy shift correction was not implemented. To determine

appropriate correction factors, displacement of some optical elements in the setup should be done which was not possible.

5.8 UniFR set-up

The University of Fribourg used the ellipsometry technique. Spectroscopic ellipsometry is a reflection-based technique. It measures the change of polarization state reflected from the sample under oblique angle of incidence, and is conventionally written as the ellipsometric ratio

$$\rho = \frac{r_p}{r_s} = \tan\psi \exp(i\Delta), \tag{16}$$

where r_p and r_s are the Fresnel's coefficients for p- and s-polarized light, ψ and Δ are the ellipsometric angles. In the simplest terms, ellipsometry can be understood as measurement of the p-polarized reflection - which is more sensitive to sample properties - with the s-polarized reflection serving as a reference. In the ellipsometric configuration the p- and s-polarized components are incident on the sample together and their amplitude ratio is controlled by the polarizer. The reflected beam is generally elliptically polarized. Measuring the ellipticity and tilt of the reflected state allows one to measure the amplitude ratio between the reflected p- and s-polarized components, $|r_p| / |r_s|$, as well as their mutual phase shift Δ.

Time domain THz spectroscopy can measure amplitude and phase of the reflected waves and initial proposals for TD-THz ellipsometers employed simplified measurement scheme, measuring the complex E_p and E_s with 2 time-domain scans and dividing them in frequency domain [13]. Our approach consists of recording the spectra for several positions of the polarizer and analyzer – this allows for calibration for offsets between the nominal and actual azimuths of the polarizers.

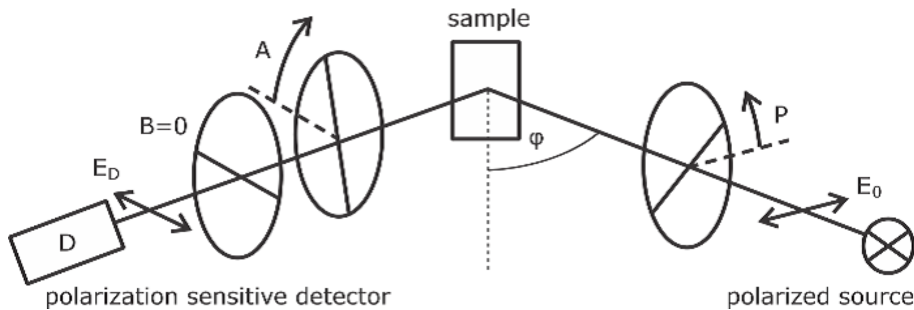

Figure 29: Spectroscopic ellipsometry principle.

The principle of the method is illustrated in Figure 29. Fixed THz source antenna is polarized in plane of incidence, then symmetric polarizer settings (we use $P = \pm 30°$) yield equal field strengths on the sample. Detector antenna is also oriented in the plane of incidence, and between the sample and the detector two analyzers are positioned. First one, closer to the sample serves as rotating analyzer (A). The second analyzer (B) is oriented with the transmission axis in the plane of incidence ($B = 0$), assuring the horizontal polarization for the detector (detector antenna has non-ideal polarization selectivity).

The home-built instrument is based on Menlo Systems CFiber 780 nm laser, with app. 100 fs pulses, 100 MHz repetition rate and 65 mW average power. Emitter antenna is Laser-Quantum TeraSED and detector antenna is Menlo systems TERA8-1. Each polarizer component (P, A, B) is a tandem of two free-standing wire-grids (Specac GS57201). The THz beam path

is enclosed in dry-air purged boxes, apart from 15 cm path in the sample space. The emitter arm can be rotated to set the angle of incidence between 45° and 90°. To avoid the need of a realignment of the free space path of the pump laser, the fixed part of the path is coupled to the movable arm along the axis of rotation of the emitter arm, as sketched in Figure 30. Sample is then positioned with the help of pre-aligned laser pointer, installed in the emitter box. Our system is equipped with a He-flow cryostat and used for unconventional oxide thin films and single crystals, often in combination with infrared ellipsometry [14], [15], [16], [17]. In this respect, the samples studied in the TEMMT project were too large and difficult to position.

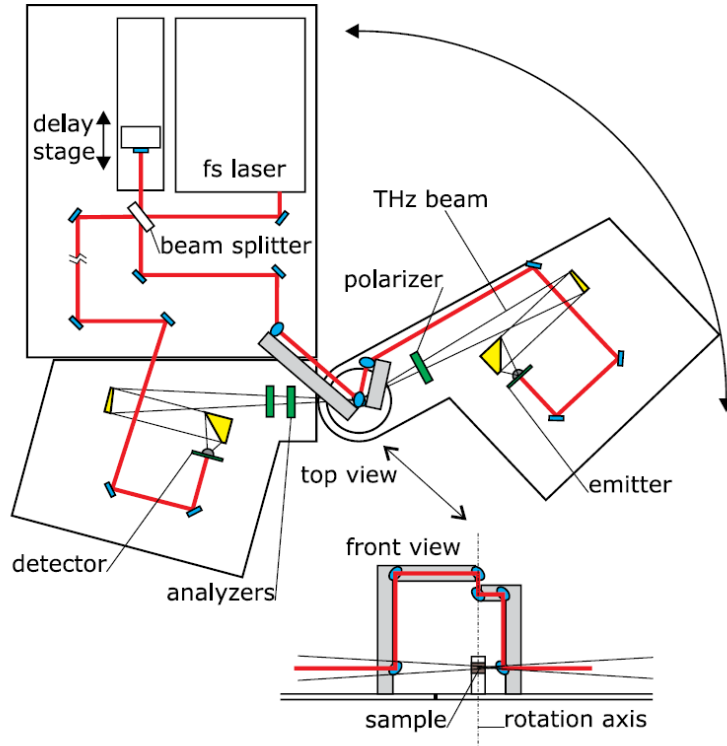

Figure 30: Ellipsometry measurement setup .

The measurement procedure was as follows. All samples were measured at 4 angles of incidence ϕ = 60°, 65°, 70°, 75°. At each, we repeated 3× pair of measurements with opposite polarizer azimuth, $P = \pm 30°$. For each P setting, sequence of 5 analyzer azimuths is followed (A = 0°, 36°, 72°, 108°, 144°). Complete time-domain signal is measured at each of these conditions. Time domain window was set starting 9 ps before the main reflection and long enough to capture all multiple reflections visible above the noise level. For most of the samples the TD range was 88 ps, apart from the thicker TPX (sample #4), YAG (sample #5) and Polyethylene (sample #6b) – for those the TD range was 136 ps. Usable frequency domain range is 0.1 - 3 THz. Each rotating analyzer sequence provides FD spectrum of the ellipsometric angles ψ and Δ. The spectra from the 6 repetitions (3× $P = 30°$ and 3× P = -30°) are corrected for the offsets of polarizer and analyzer, and then averaged. The offsets were determined a-priori on a known sample of weakly doped Germanium, opaque in the THz range. Resulting spectra were analysed with the well-known transfer matrix method on an optical model air-slab-air. We used the nominal slab thickness given in the project's sample documentation. The material dielectric function is then obtained from point-by-point fitting the spectra for the 4 angles of

incidence together. The resulting spectra were not further treated by any smoothing. Some of the results suffer from imperfect removal of the Fabry-Perot oscillations, particularly the glasses: Borofloat (sample #3) and Schott (sample #8).

As a self-normalized reflection-based technique, ellipsometry does not need to rely on the sample transparency. However, all samples in this project were transparent, and were measured with time-domain span long enough to capture multiple reflections. As a result, the obtained spectra contain both the reflection ellipsometry (first THz pulse reflected from the front surface) and transmission information (subsequent multiple reflections). Accuracy of the material parameter estimates thus depends on two independent input parameters: the angle of incidence, and the given thickness. Both of them might suffer from systematic errors, so at any spectral point, the fit algorithm might need to find best match to the data (ψ, Δ at four angles of incidence) with conflicting and varying impact of the angle of incidence and thickness errors. It should be noted that the UniFr TD-THz setup might suffer from small constant offset of the angle of incidence. Additional uncertainty applies for each individual sample and angle of incidence setting, as the positioning and alignment was hindered by the large size of the specimens. Due to the time constrain of this project, we could not develop an optimal approach for mounting and alignment of the large samples. Particularly, the Polyethylene samples (#6) were difficult to align due to their rough surface, which did not provide specular reflection of the alignment laser. Finally, ellipsometry on finite-size samples suffers from artefacts due to polarization dependent diffraction [18]. They are not very strong thanks to the sufficient size of the samples but might still be responsible for the discrepancies in the low-frequency end of the spectra.

6 Results

The measurement comparison generated large amount of data in different frequency bands, whereas the results have been obtained using different measurement methods. The measured data have been compared according to various criteria and will be presented in following sections. The purpose of this pilot study was to gain experience with particular measurement setups. Some of the participants have not calculated the measurement uncertainty due to lack of expertise and thus the measured results are not easily comparable. Figure 31 shows the overview of samples measured by particular institutes and methods. The numbering of samples corresponds to the list of materials given in Table 3.

	GUM OR	LNE TDS	METAS FDS	METAS MCK	NPL MCK	NPL OR	NPL TDS	PTB FS	PTB MCK	TUBITAK FS	UniFR TDE	WAT TDS
1	x	x	x	x	x		x		x	x	x	x
2A1a		x	x	x	x	x	x	x	x	x	x	
2A1b		x	x		x	x	x	x	x	x		
2A2a		x	x	x	x	x	x	x	x	x	x	
2A2b		x	x	x	x	x	x	x	x	x		
2A3a		x	x	x	x	x	x	x	x	x	x	
2A3b		x	x		x	x	x	x	x	x		
2A4a										x		x
3	x	x	x	x	x		x	x	x	x	x	x
4		x	x	x	x		x	x	x	x	x	x
5		x	x	x	x	x	x		x	x	x	x
6a	x	x	x	x	x	x	x	x	x	x	x	x
6b		x	x	x	x	x	x	x	x	x	x	
6c		x								x		x
6d		x		x	x	x	x	x	x	x		
7a		x	x	x	x		x		x	x	x	x
7b		x	x	x	x		x		x	x	x	x
8a	x	x	x	x	x		x	x	x	x	x	x
8b		x	x		x		x	x	x	x		x
9			x	x								

Figure 31: Overview of measurements performed by particular institutes and methods. Some institutes provided measured data only (green entries), some also provided the measurement uncertainty (light blue entries).

6.1 All materials measured using various methods

This section shows all the material samples from Table 3 measured using one particular method (i.e., TDS, FDS, FS, MCK, OR or TDE) or measured using methods that fall into the same group (i.e., VNA-based, photonic-based). Some of the samples were cut from the same piece of bulk material (i.e. #2 Fused silica, #6 UHMW Polyethylene, #8 AF32 Schott) and thus it may be interesting to see in Sections 6.2 to 6.5 how particular extraction methods are dependent on the sample thickness when measured by the same laboratory. The material #7 Doped silicon was represented by two different samples with different dopings, not cut from the same piece of bulk material.

6.1.1 All materials measured using TDS method

This section shows all the material samples from Table 3 measured using TDS method (NPL, LNE, WAT), where applicable.

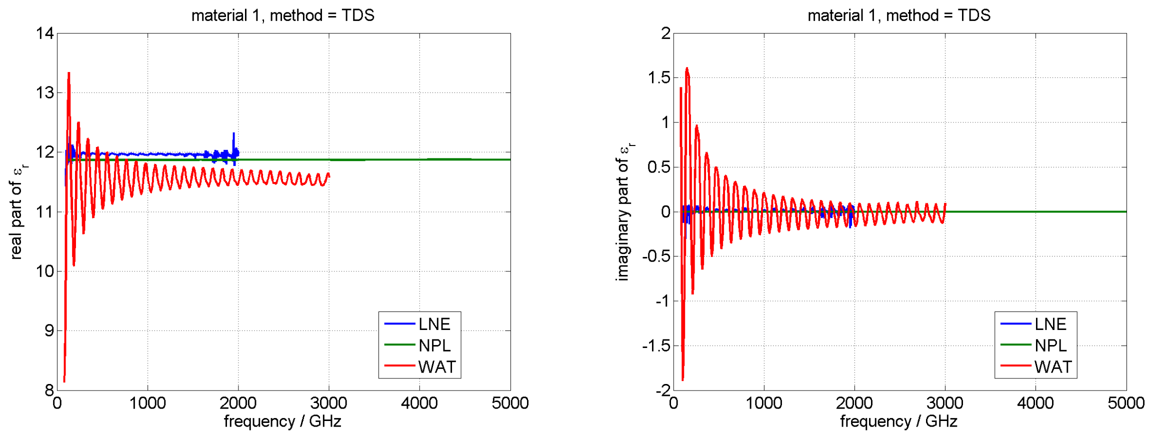

Figure 32: Material 1 (real + imaginary part of ε_r) measured using TDS.

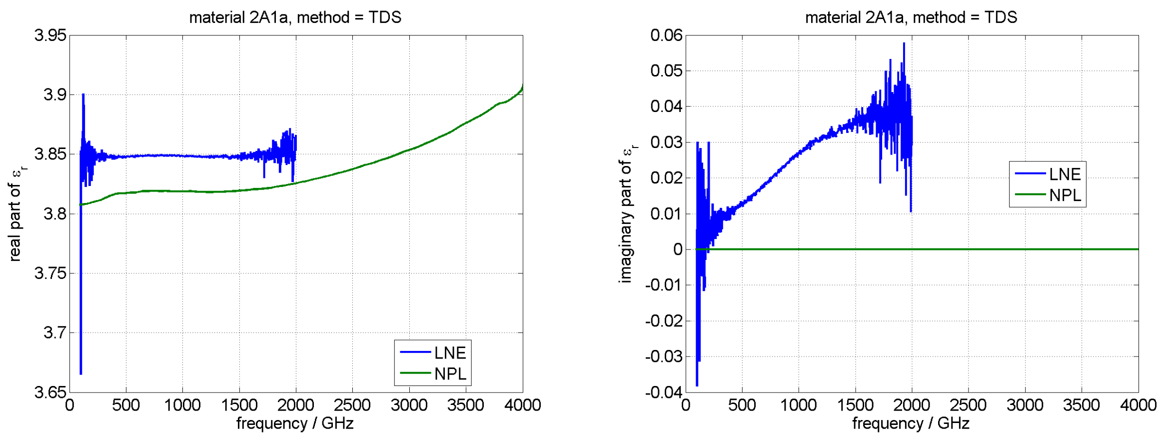

Figure 33: Material 2A1a (real + imaginary part of ε_r) measured using TDS.

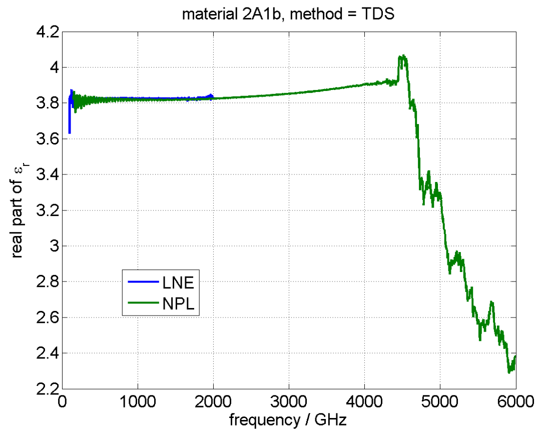

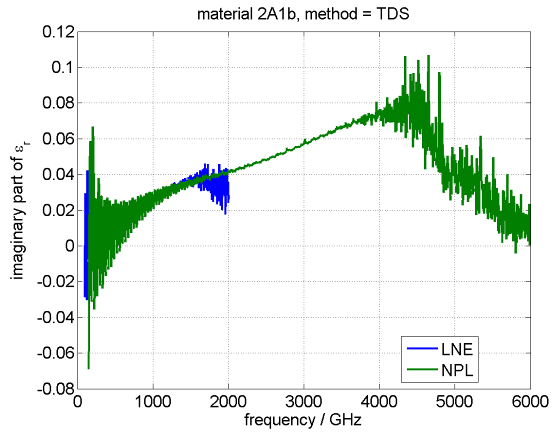

Figure 34: Material 2A1b (real + imaginary part of ε_r) measured using TDS.

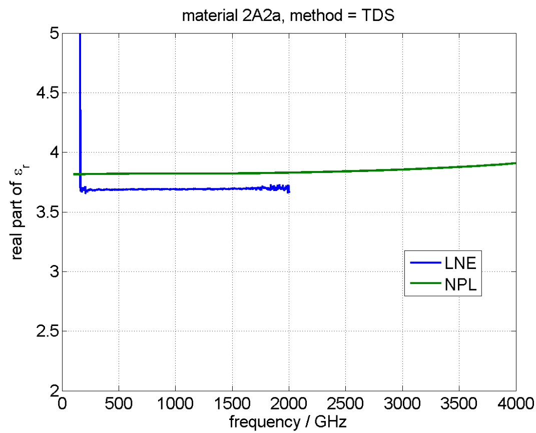

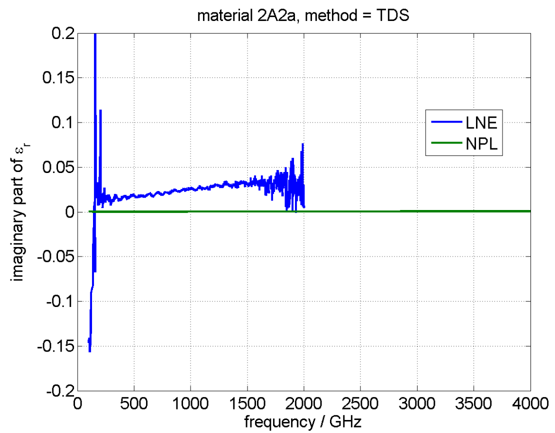

Figure 35: Material 2A2a (real + imaginary part of ε_r) measured using TDS.

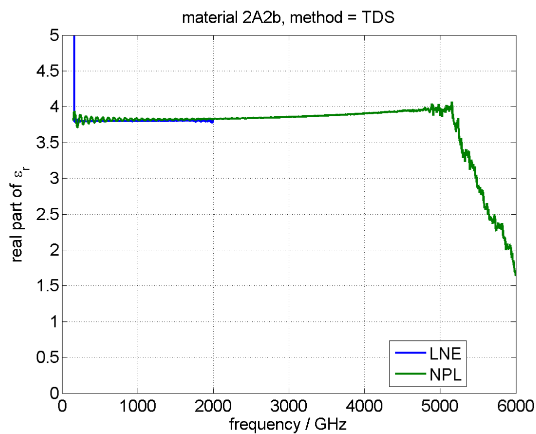

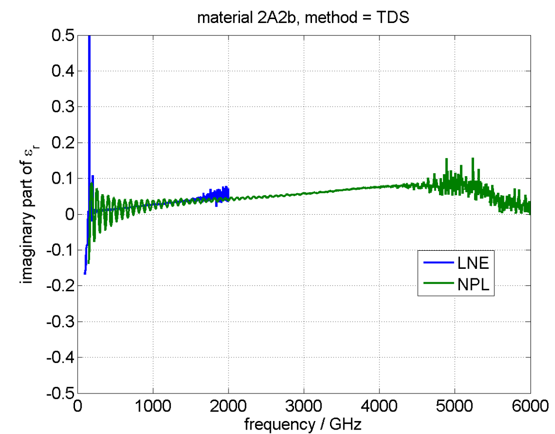

Figure 36: Material 2A2b (real + imaginary part of ε_r) measured using TDS.

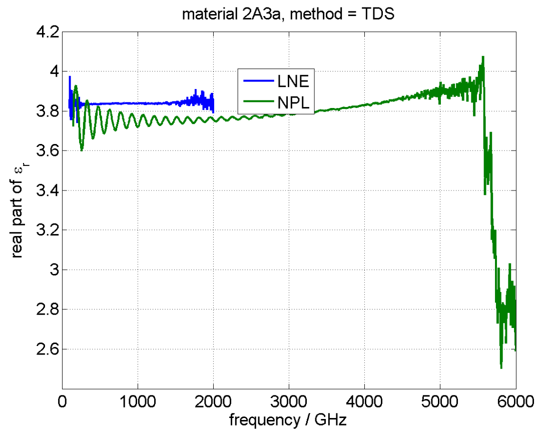

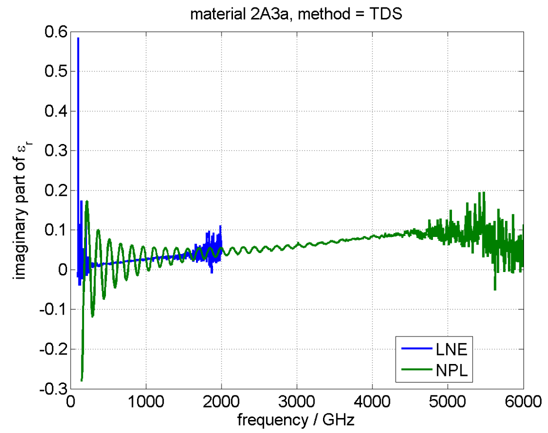

Figure 37: Material 2A3a (real + imaginary part of ε_r) measured using TDS.

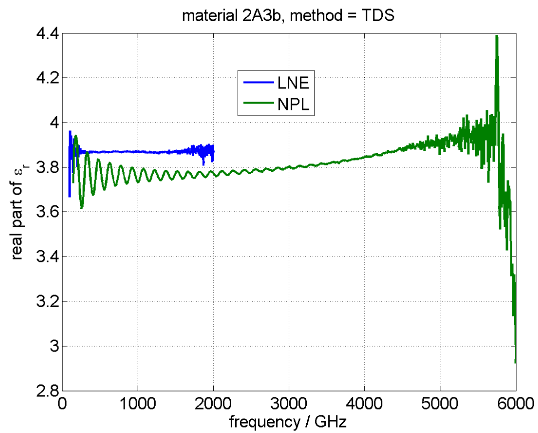

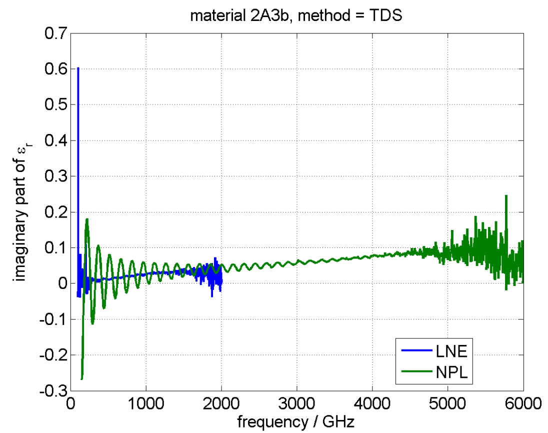

Figure 38: Material 2A3b (real + imaginary part of ε_r) measured using TDS.

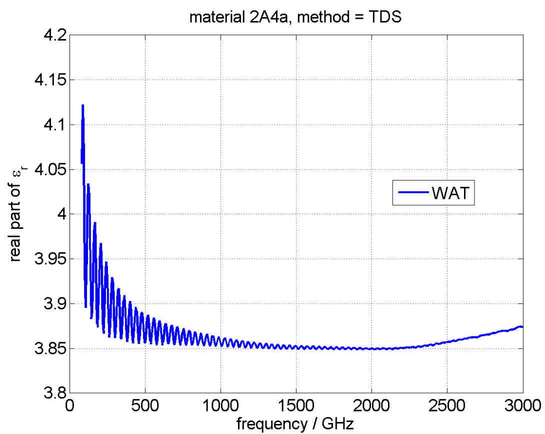

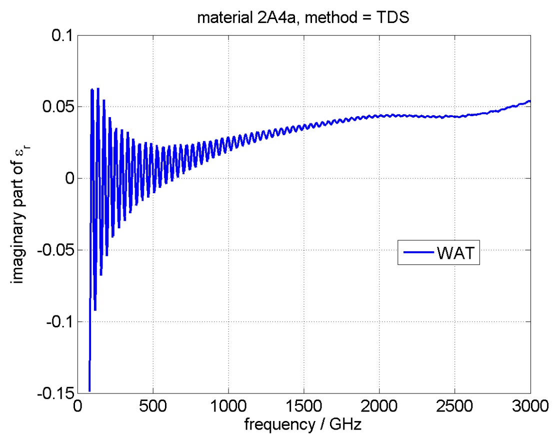

Figure 39: Material 2A4a (real + imaginary part of ε_r) measured using TDS.

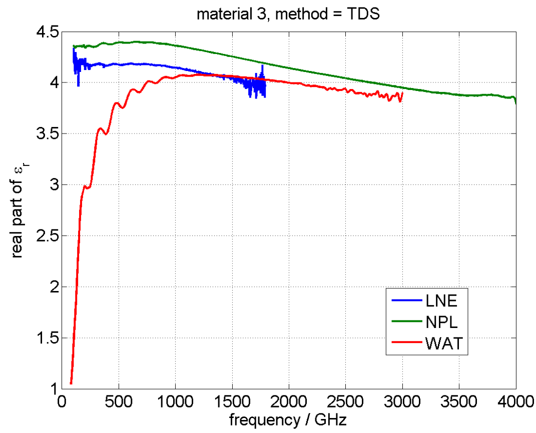

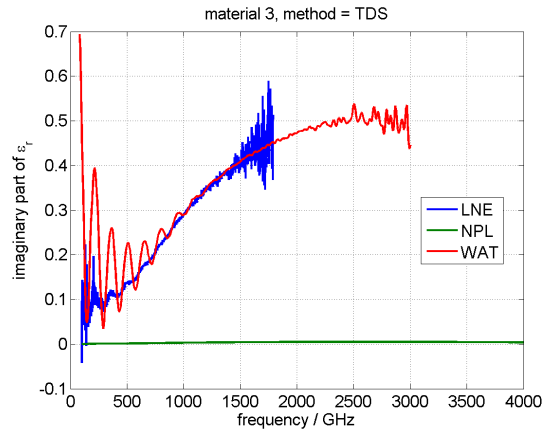

Figure 40: Material 3 (real + imaginary part of ε_r) measured using TDS.

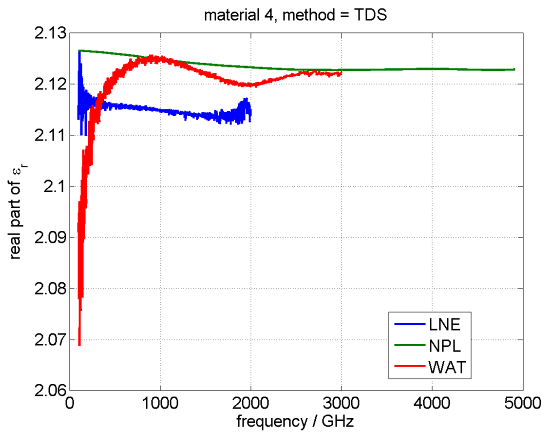

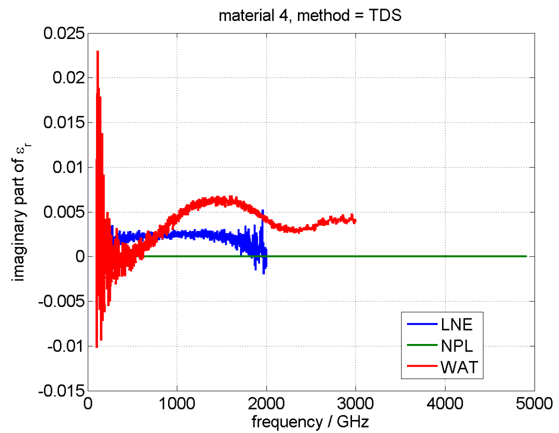

Figure 41: Material 4 (real + imaginary part of ε_r) measured using TDS.

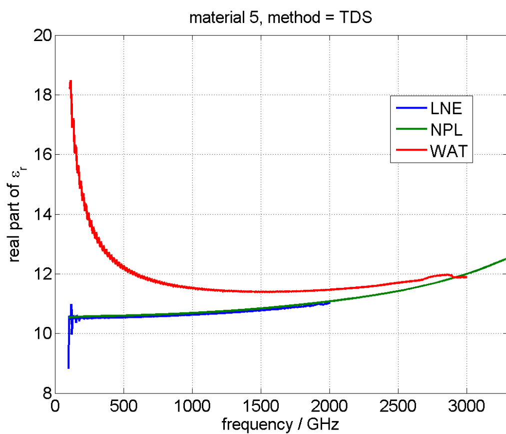

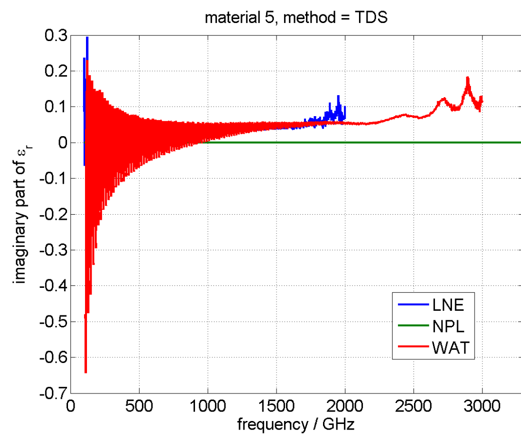

Figure 42: Material 5 (real + imaginary part of ε_r) measured using TDS.

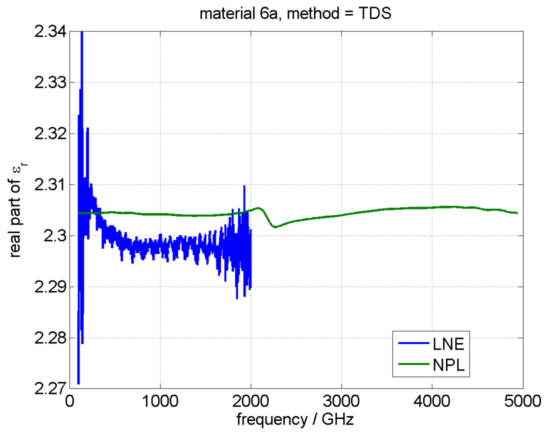

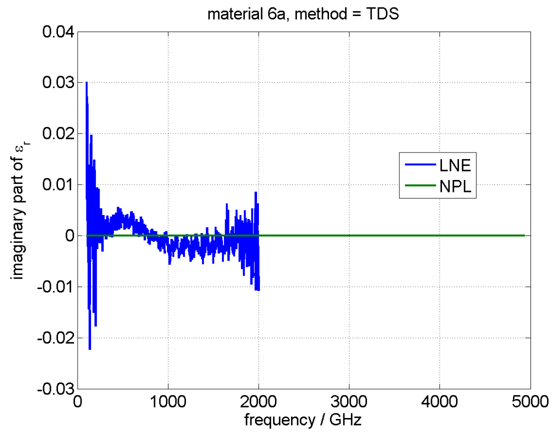

Figure 43: Material 6a (real + imaginary part of ε_r) measured using TDS.

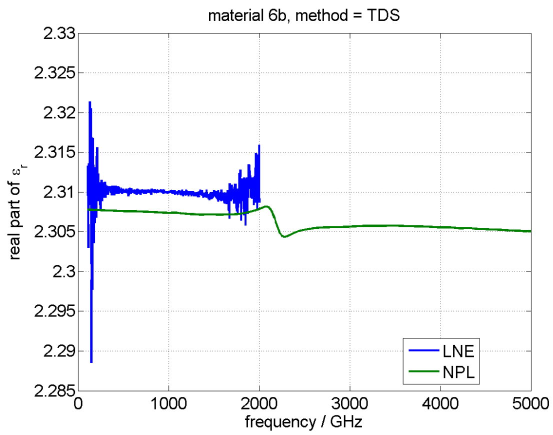

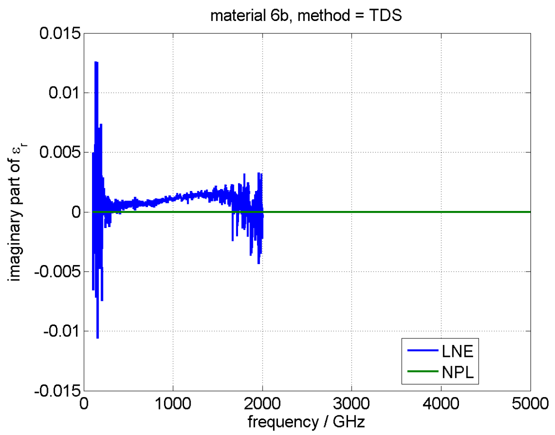

Figure 44: Material 6b (real + imaginary part of ε_r) measured using TDS.

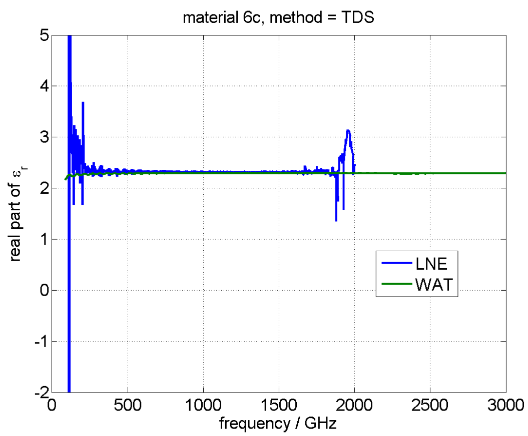

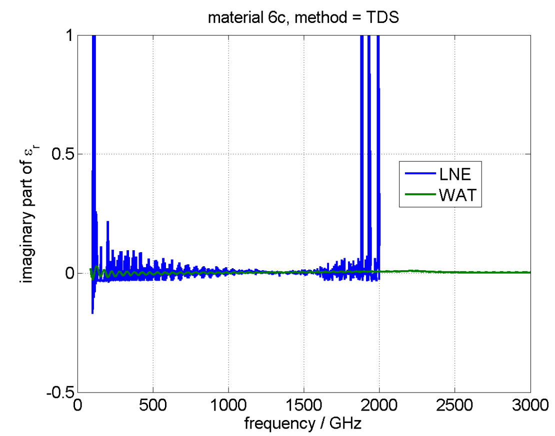

Figure 45: Material 6c (real + imaginary part of ε_r) measured using TDS.

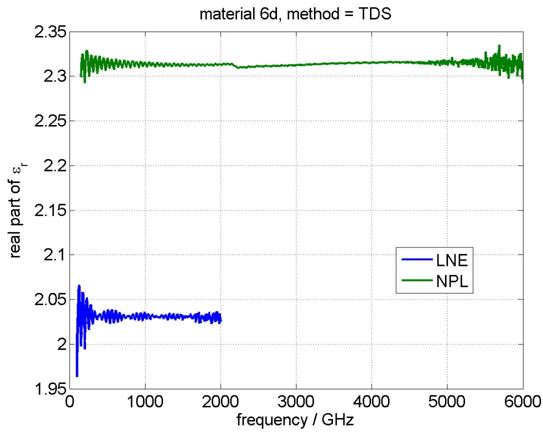

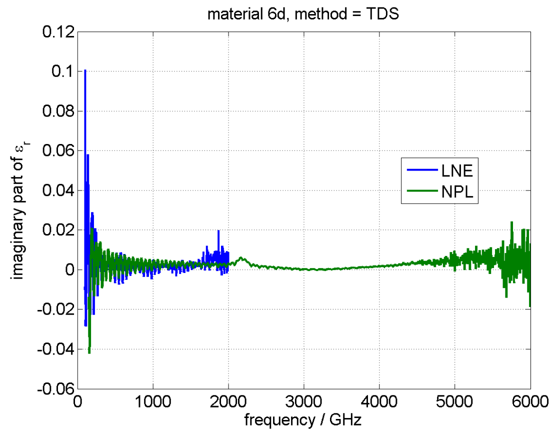

Figure 46: Material 6d (real + imaginary part of ε_r) measured using TDS.

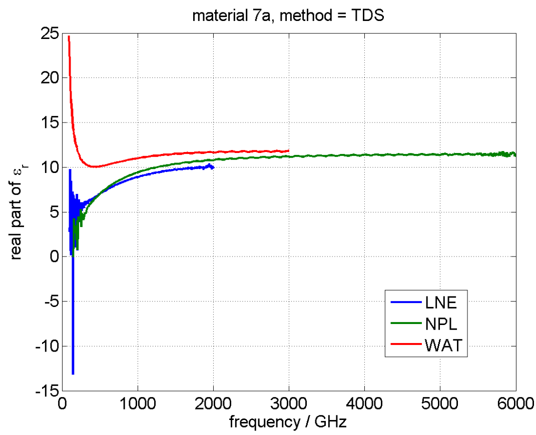

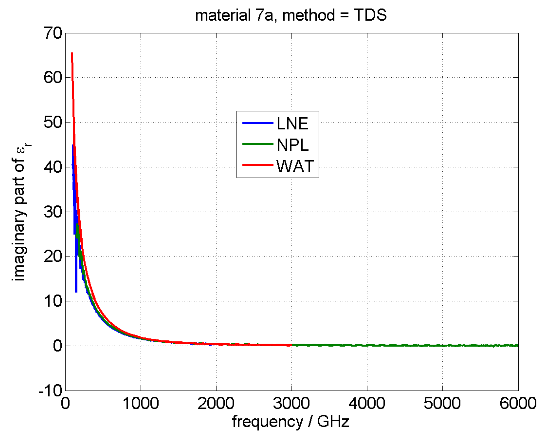

Figure 47: Material 7a (real + imaginary part of ε_r) measured using TDS.

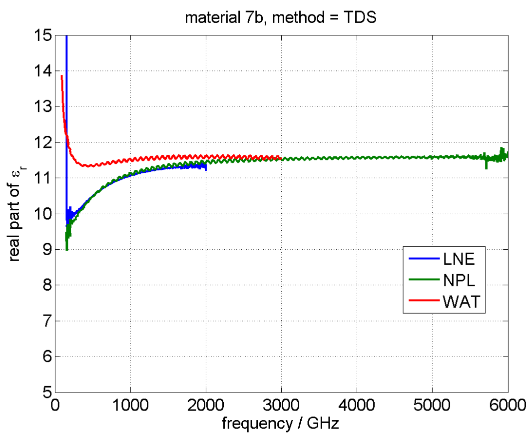

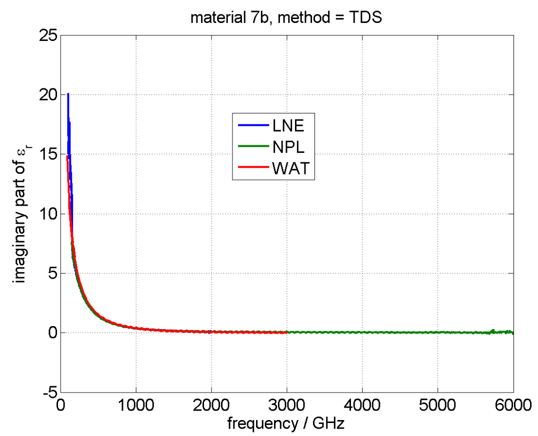

Figure 48: Material 7b (real + imaginary part of ε_r) measured using TDS.

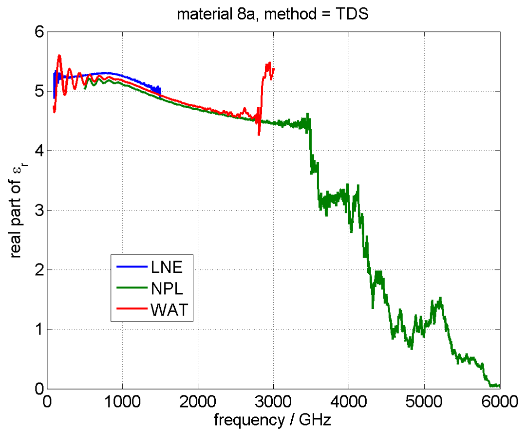

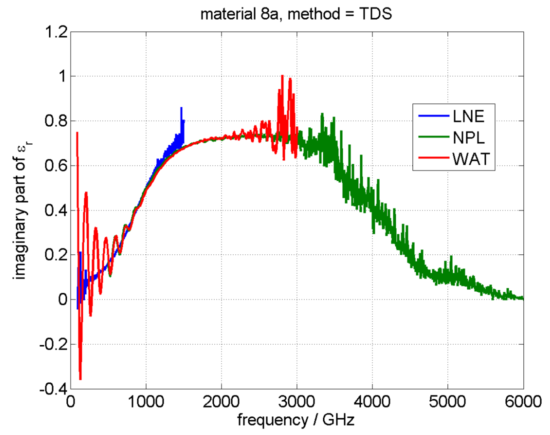

Figure 49: Material 8a (real + imaginary part of ε_r) measured using TDS.

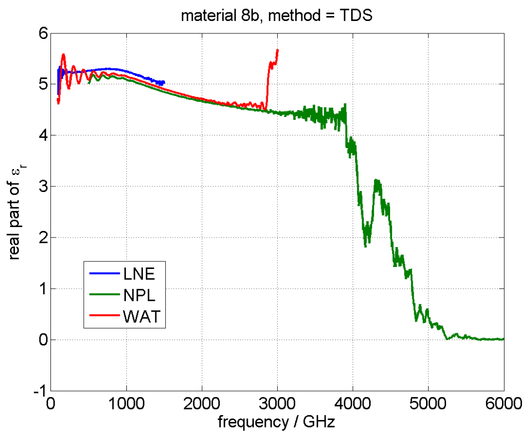

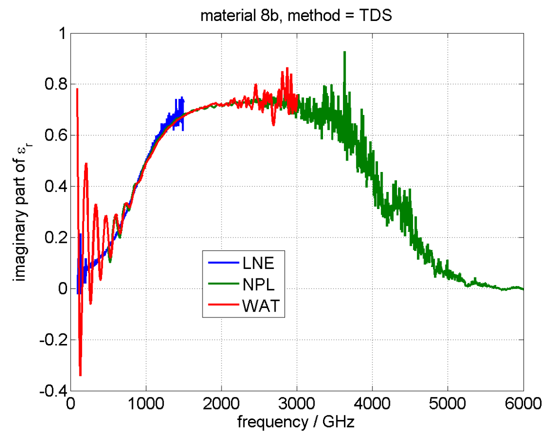

Figure 50: Material 8b (real + imaginary part of ε_r) measured using TDS.

6.1.2 All materials measured using VNA-based methods

Comparison of all the material samples from Table 3 measured using VNA-based setups of METAS (MCK), NPL (MCK) and PTB (MCK, FS). Data of UME have been excluded from the comparative graphs. The rapid oscillation observed in the extracted dielectric constant and loss tangent is due to the spurious signal reflections inside the MCK. Filtering techniques (e.g., time-gating and Savitzky-Golay filter) can be used to clean up the data and produce smooth results when required [19]. The misalignment between frequency bands for the MCK measurements of the institute PTB is probably caused by the fact that the MCKs are most likely designed to operate best in the middle of the respective waveguide band. This means that e.g. mode purity and other propagation characteristics of the MCK will suffer at the edges of the frequency bands.

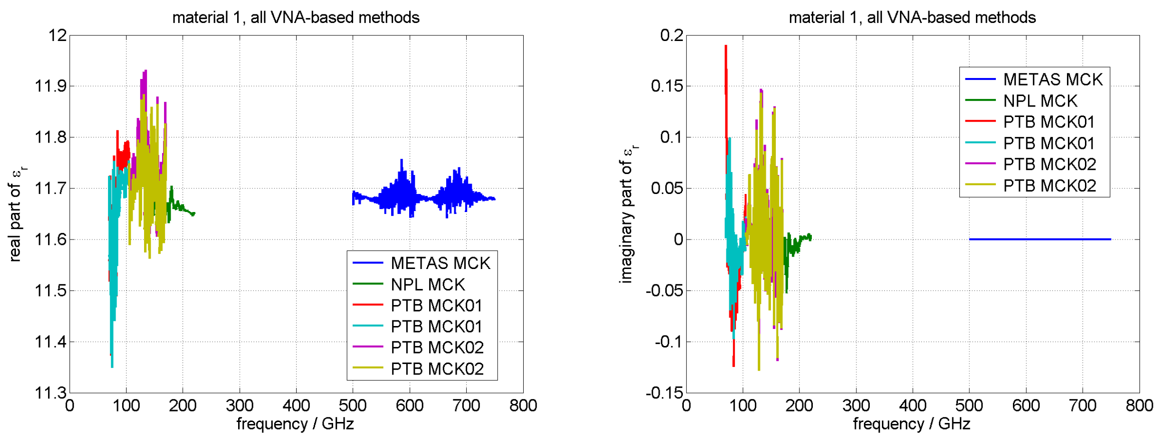

Figure 51: Material 1 measured by VNA-based methods.

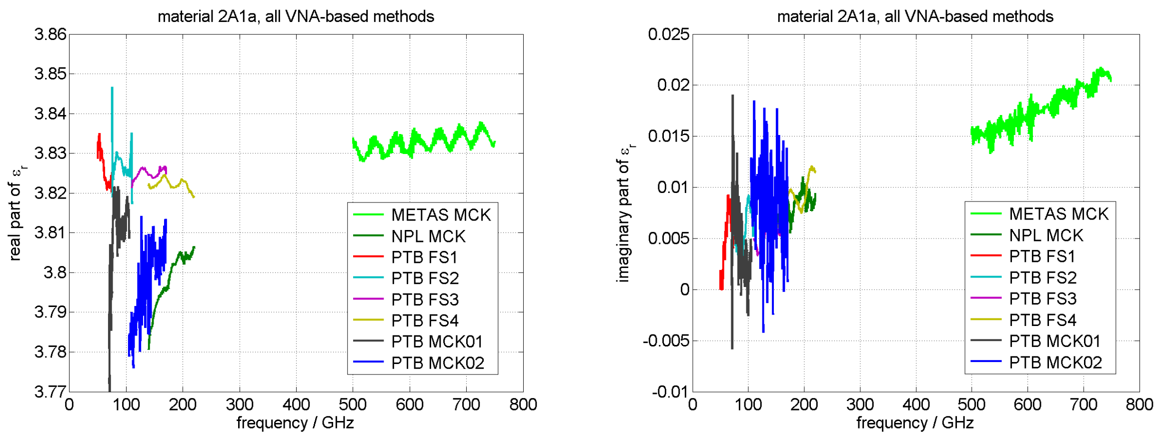

Figure 52: Material 2A1a measured by VNA-based methods.

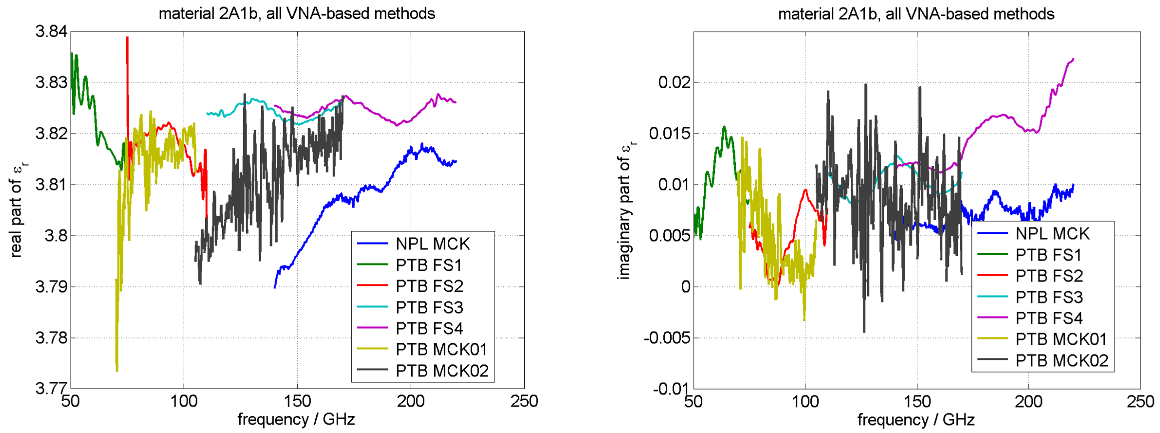

Figure 53: Material 2A1b measured by VNA-based methods.

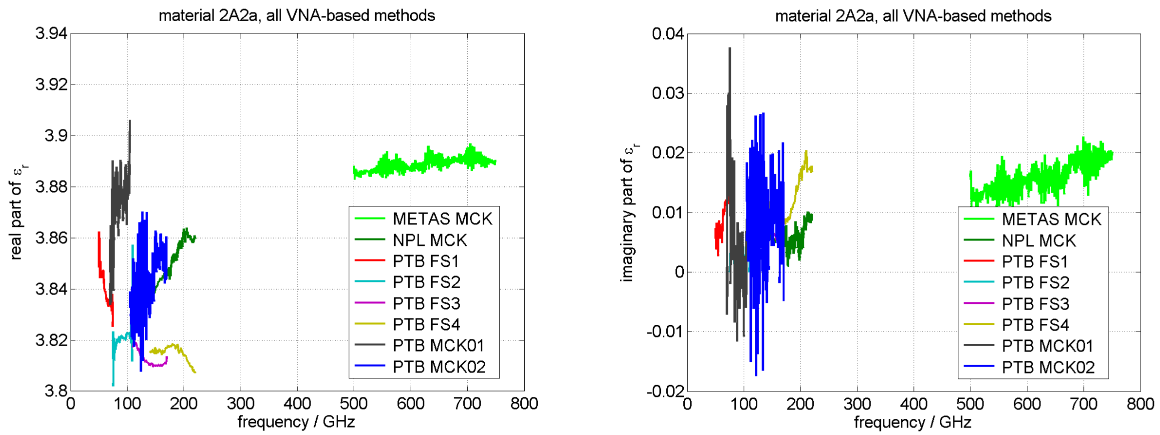

Figure 54: Material 2A2a measured by VNA-based methods.

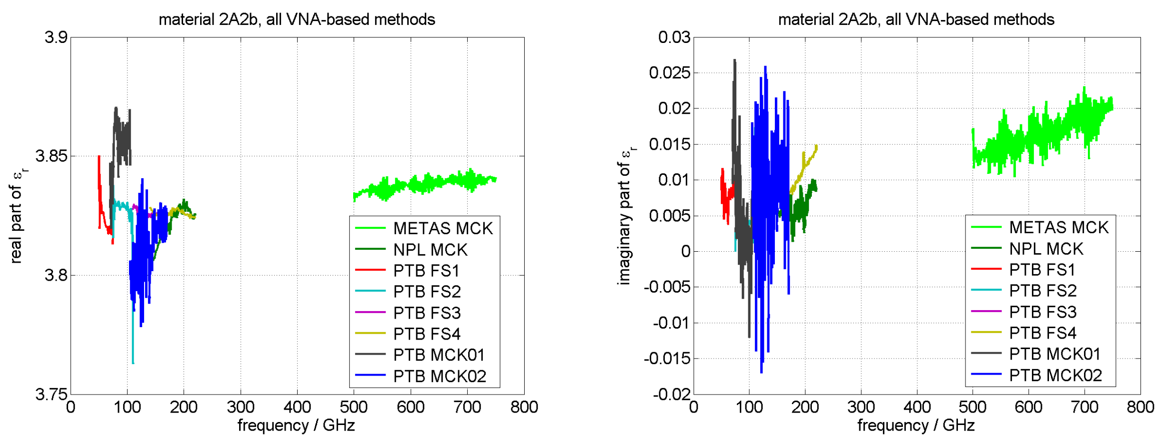

Figure 55: Material 2A2b measured by VNA-based methods.

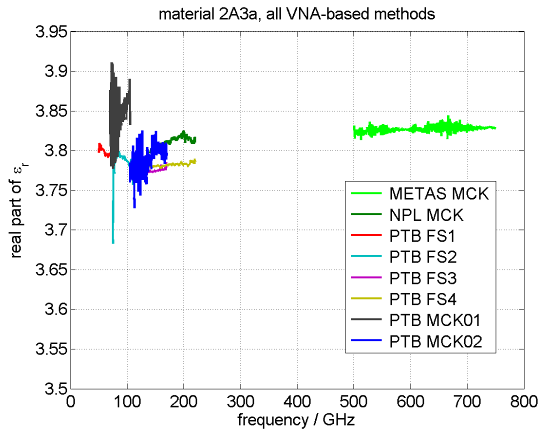

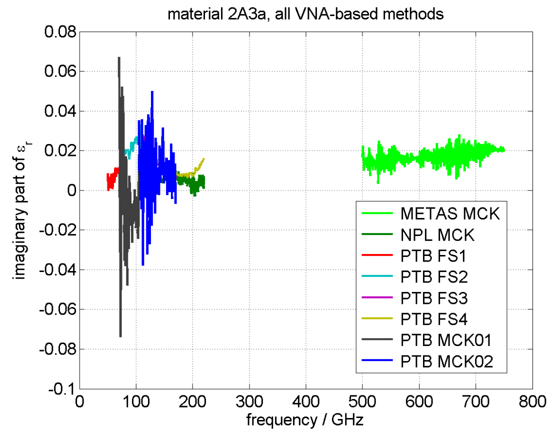

Figure 56: Material 2A3a measured by VNA-based methods.

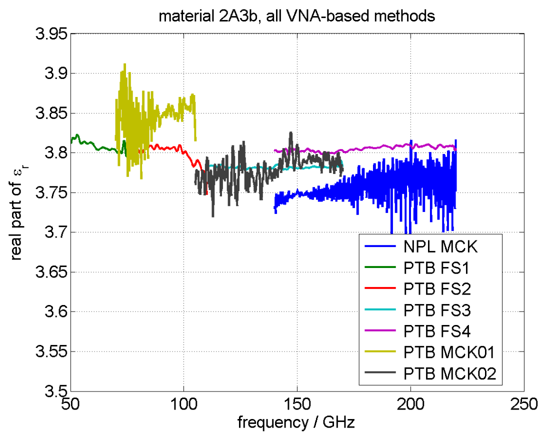

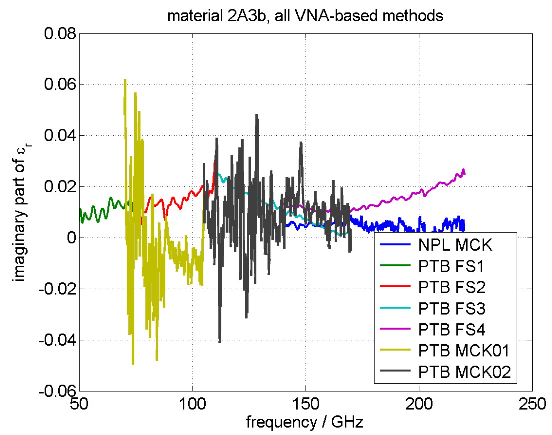

Figure 57: Material 2A3b measured by VNA-based methods.

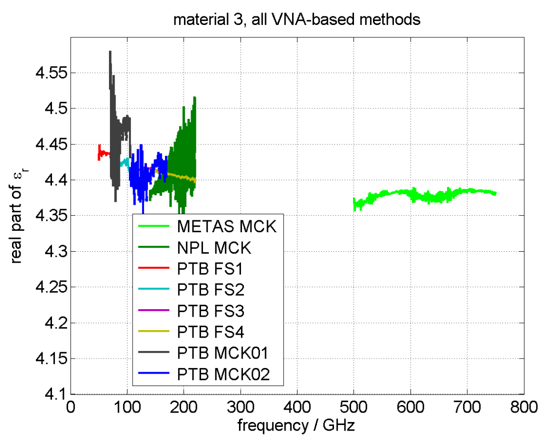

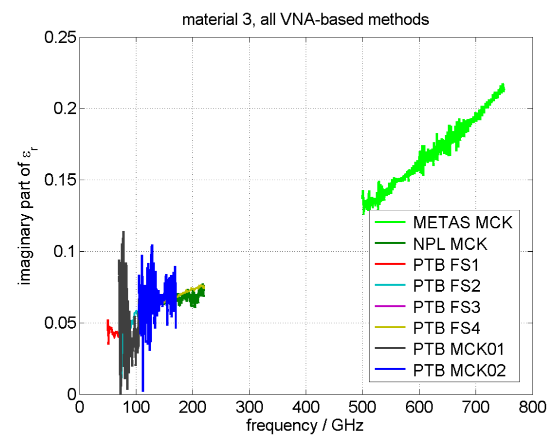

Figure 58: Material 3 measured by VNA-based methods.

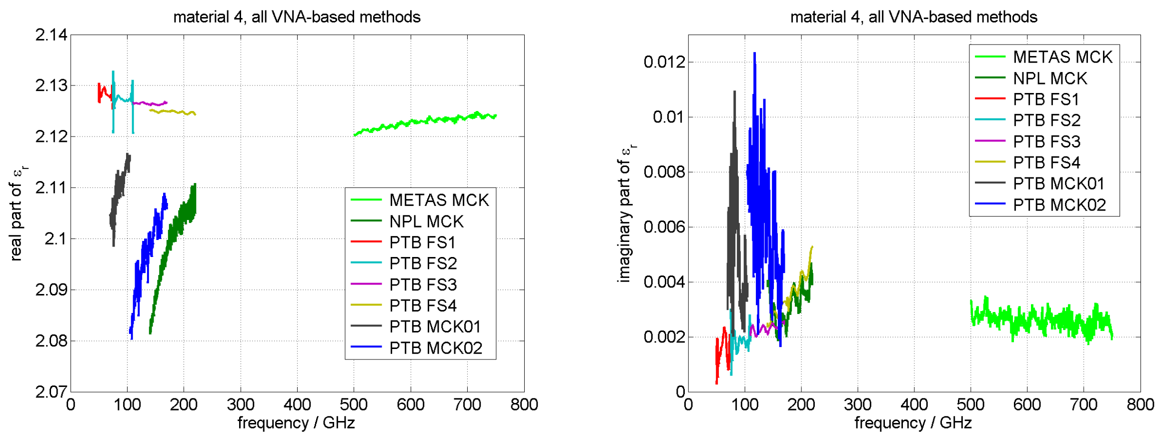

Figure 59: Material 4 measured by VNA-based methods.

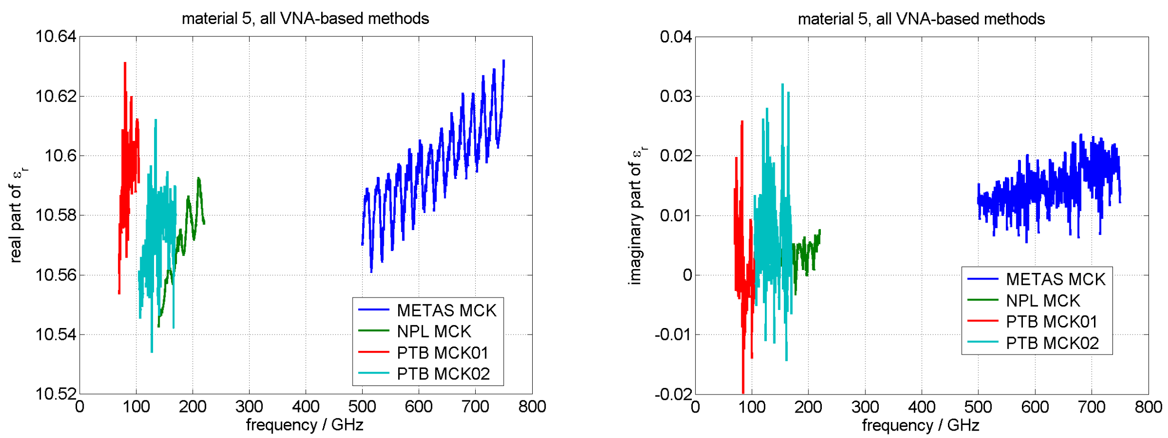

Figure 60: Material 5 measured by VNA-based methods.

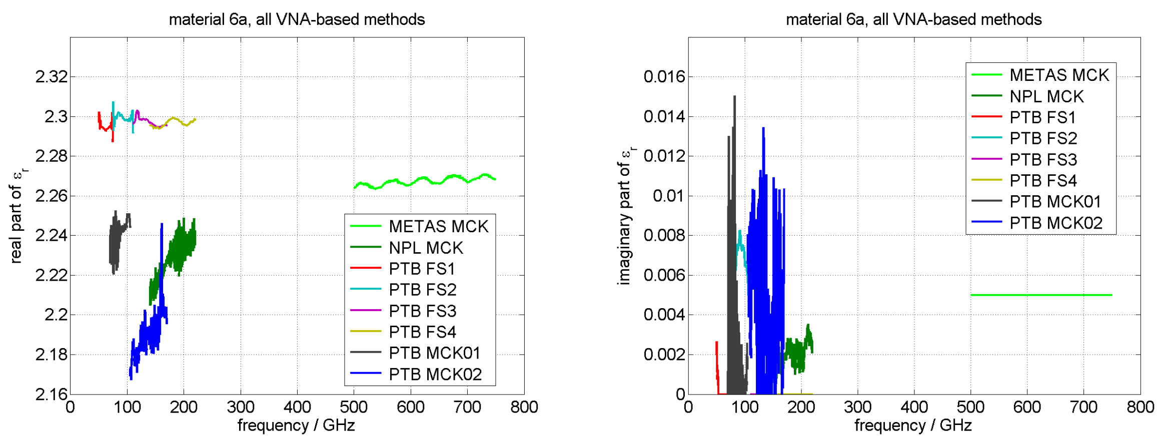

Figure 61: Material 6a measured by VNA-based methods.

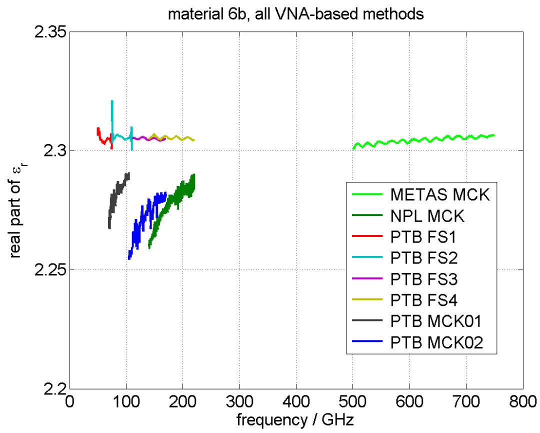

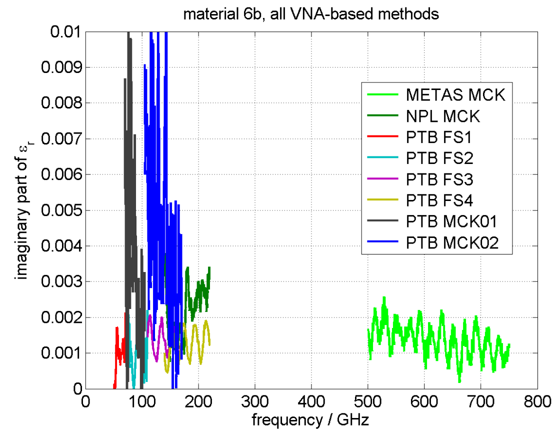

Figure 62: Material 6b measured by VNA-based methods.

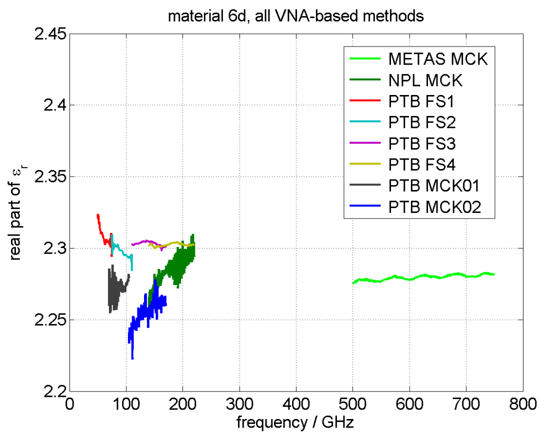

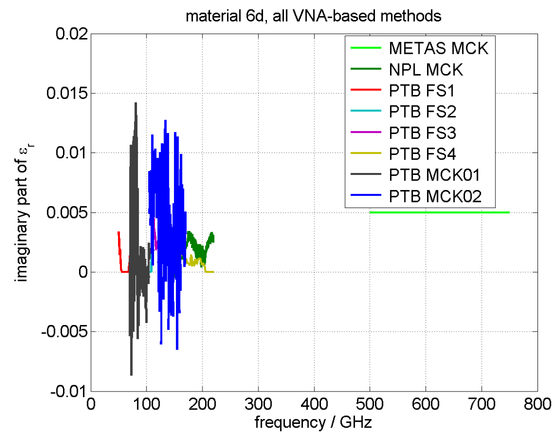

Figure 63: Material 6d measured by VNA-based methods.

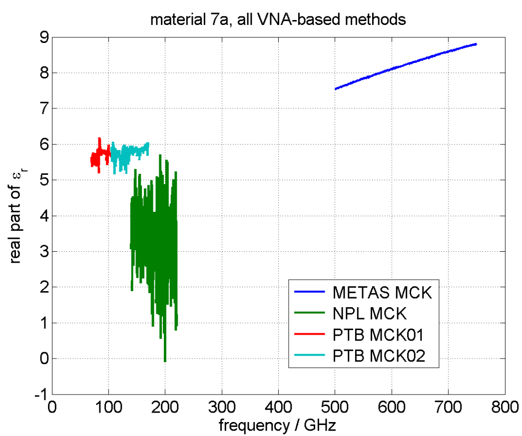

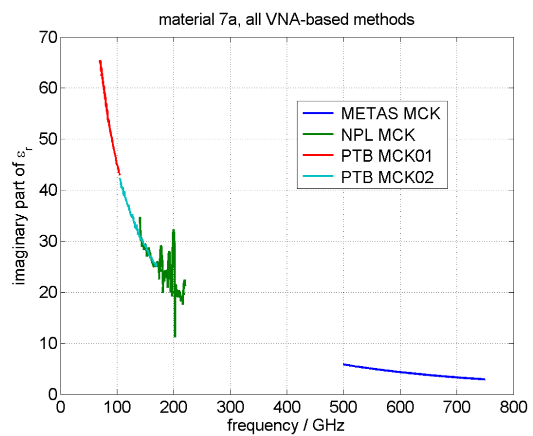

Figure 64: Material 7a measured by VNA-based methods.

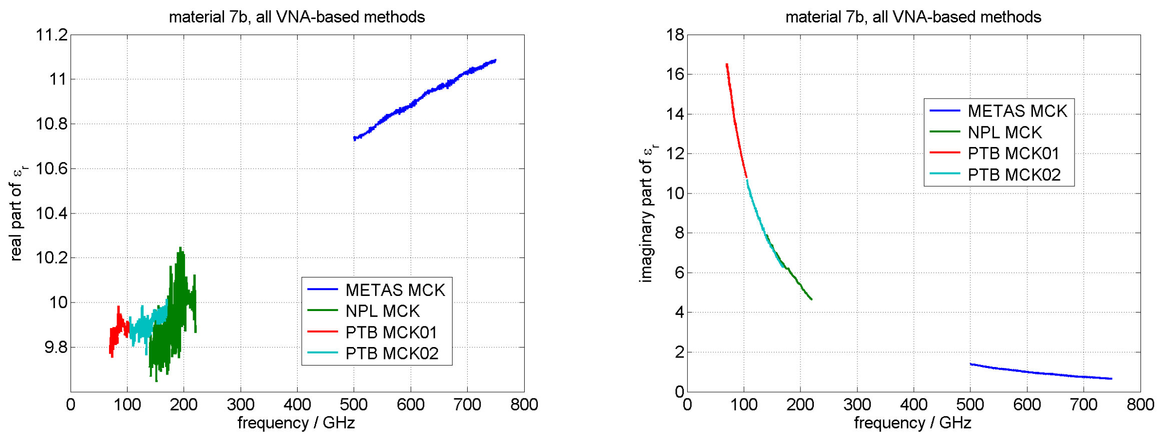

Figure 65: Material 7b measured by VNA-based methods.

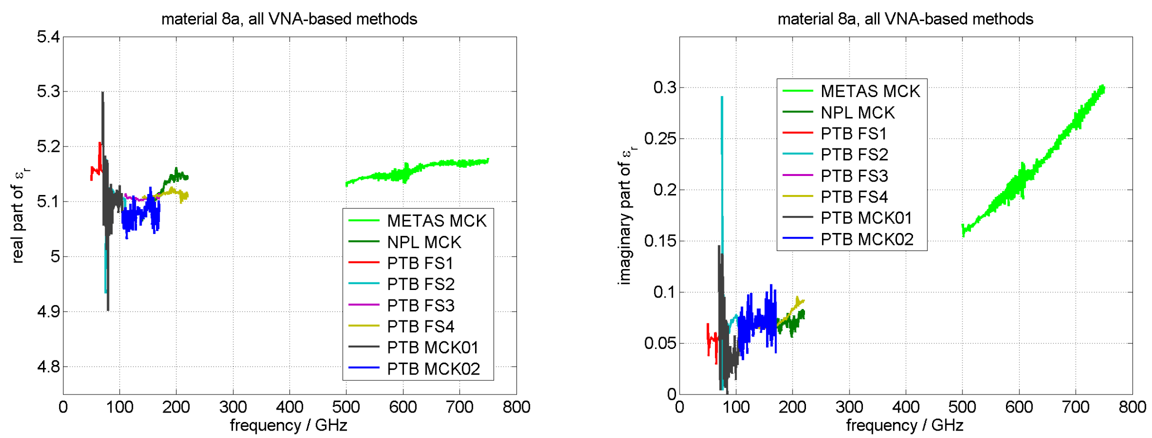

Figure 66: Material 8a measured by VNA-based methods.

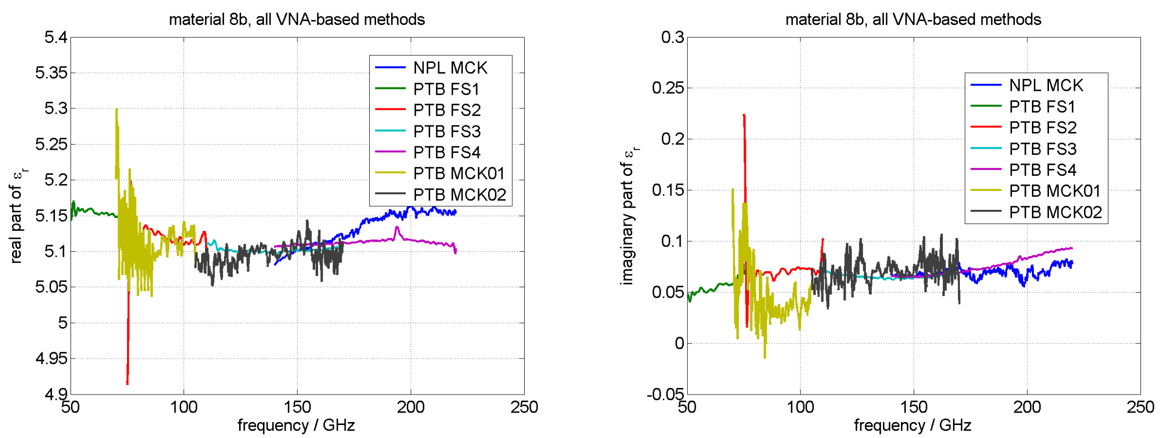

Figure 67: Material 8b measured by VNA-based methods.

6.1.3 All materials measured using open resonator-based methods

This section shows a comparison of all the material samples from Table 3 measured by open resonator-based methods by particular institutes.

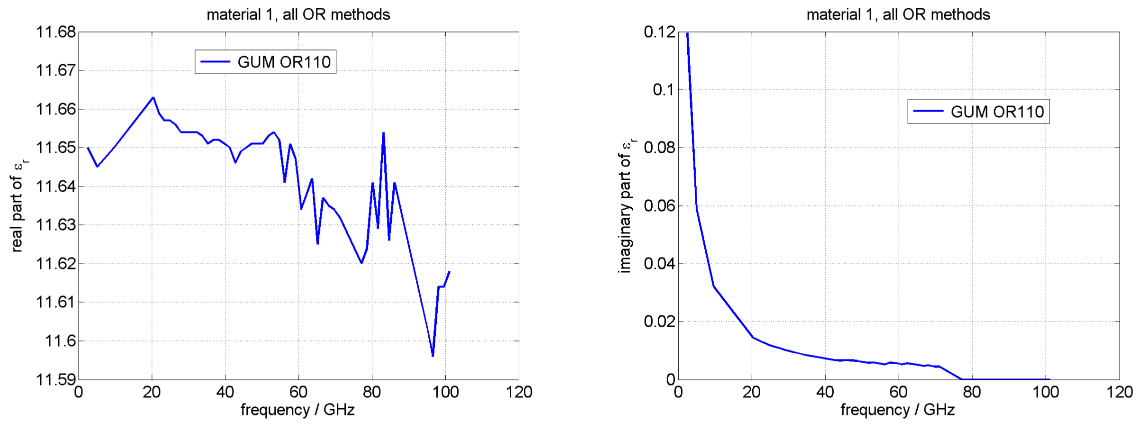

Figure 68: Material 1 measured by open resonator-based methods.

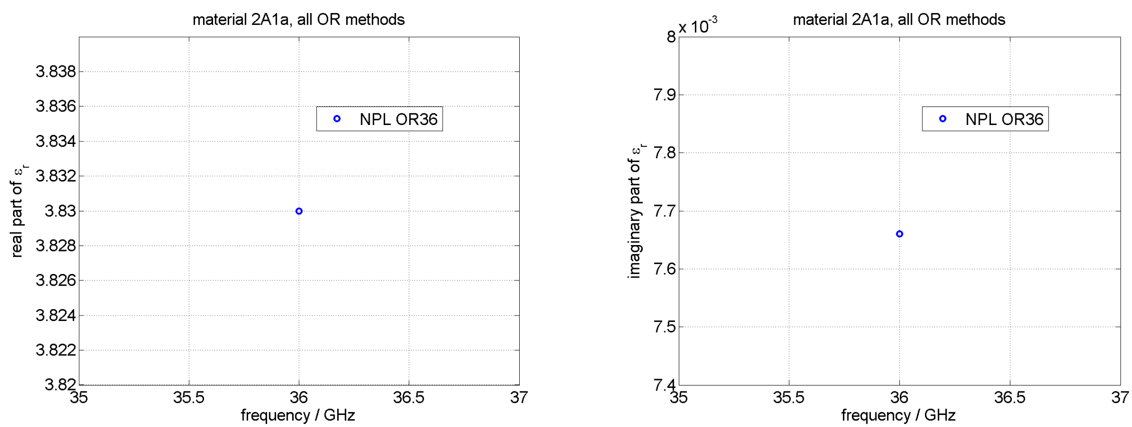

Figure 69: Material 2A1a measured by open resonator-based methods.

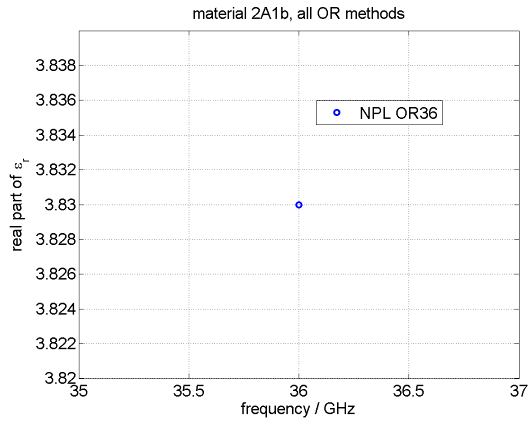

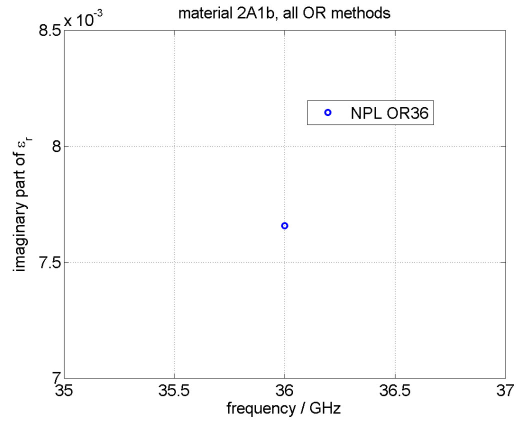

Figure 70: Material 2A1b measured by open resonator-based methods.

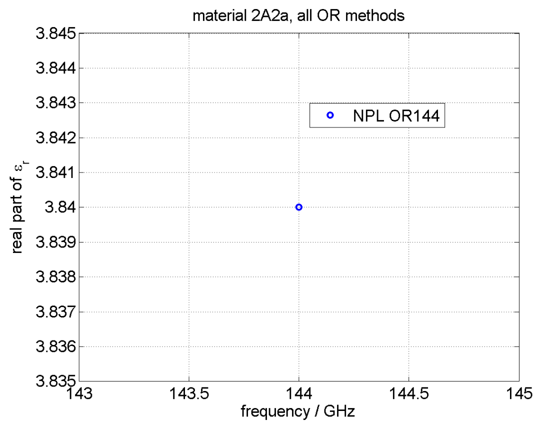

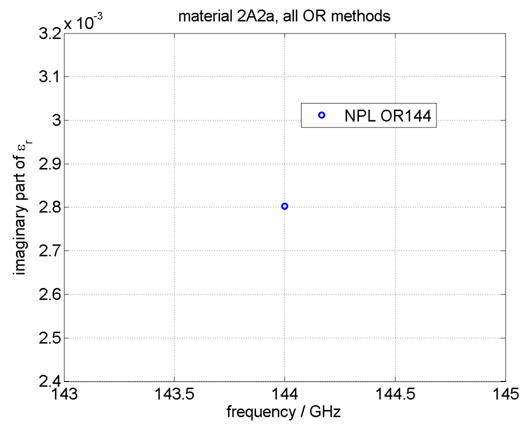

Figure 71: Material 2A2a measured by open resonator-based methods.

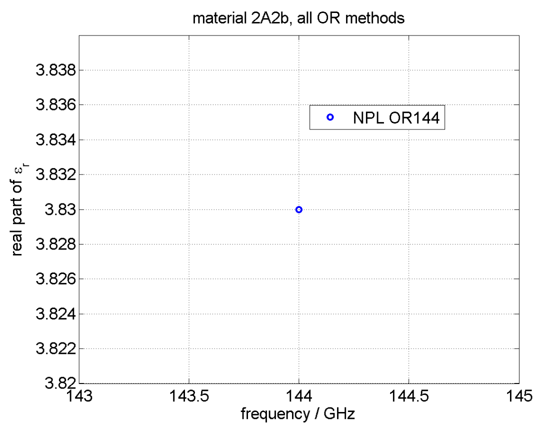

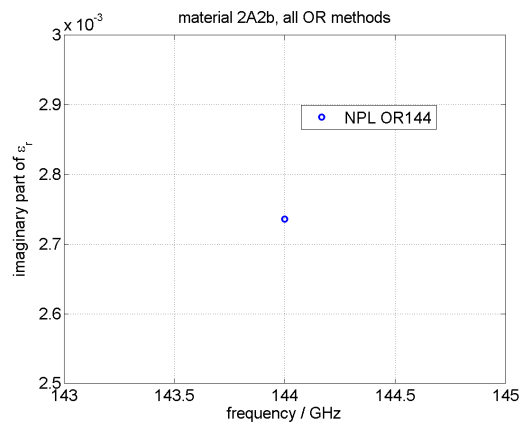

Figure 72: Material 2A2b measured by open resonator-based methods.

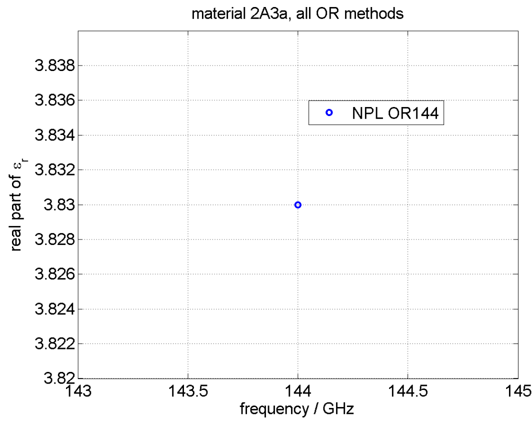

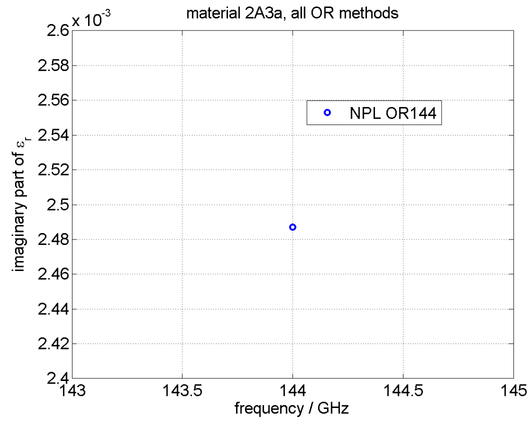

Figure 73: Material 2A3a measured by open resonator-based methods.

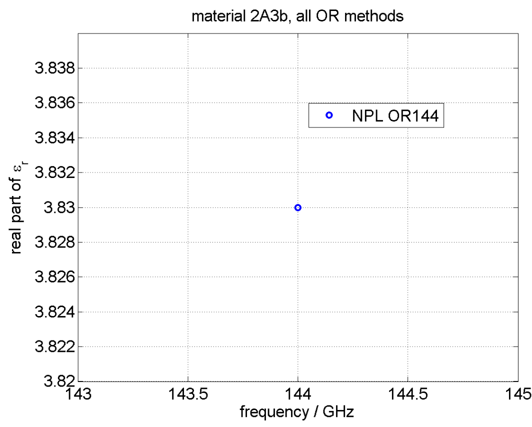

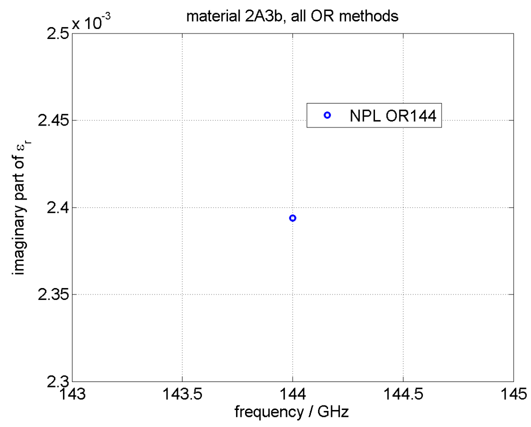

Figure 74: Material 2A3b measured by open resonator-based methods.

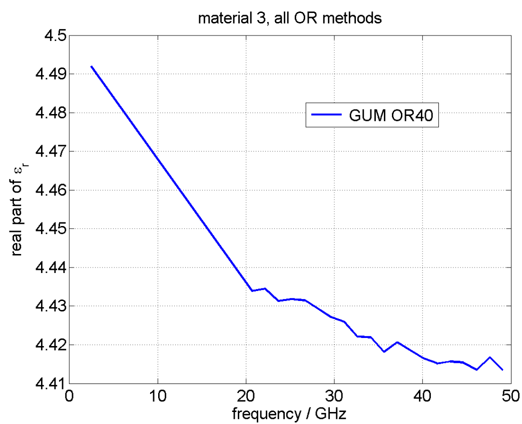

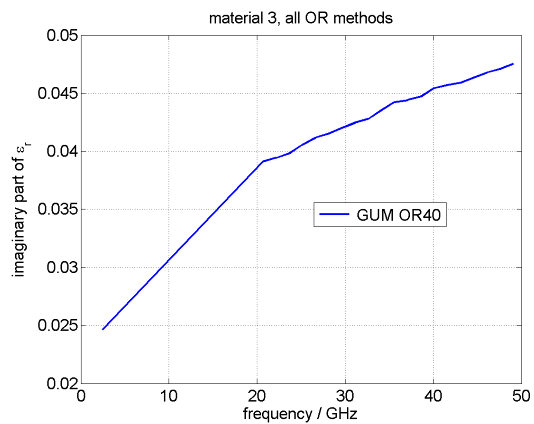

Figure 75: Material 3 measured by open resonator-based methods.

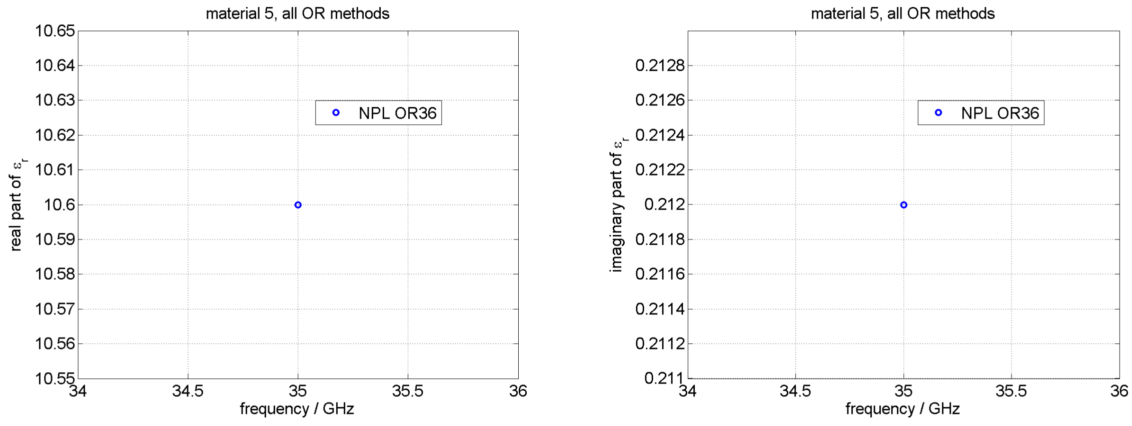

Figure 76: Material 5 measured by open resonator-based methods.

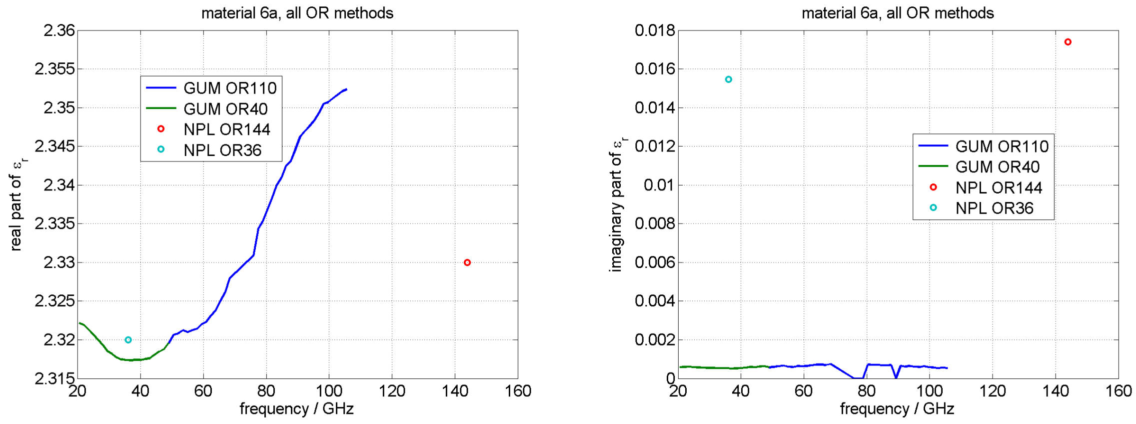

Figure 77: Material 6a measured by open resonator-based methods.

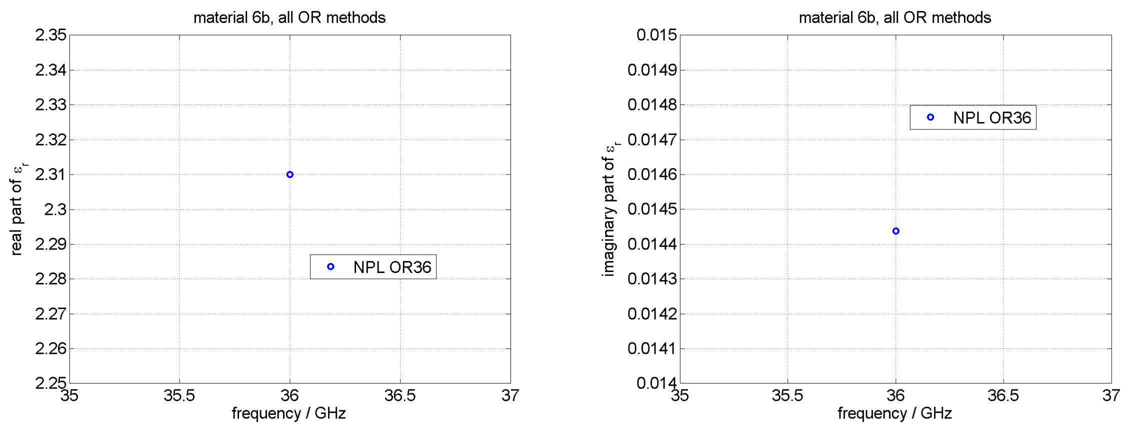

Figure 78: Material 6b measured by open resonator-based methods.

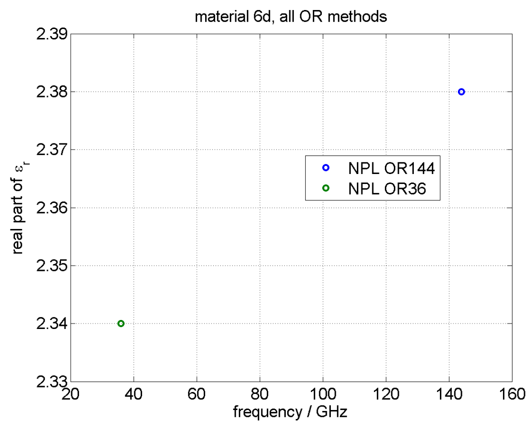

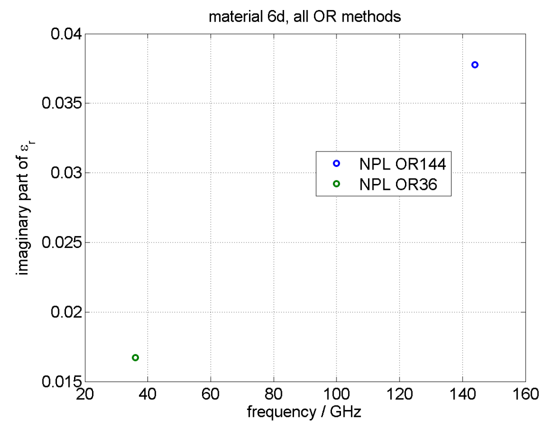

Figure 79: Material 6d measured by open resonator-based methods.

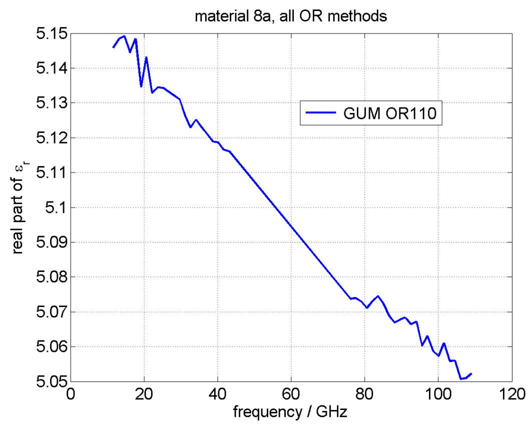

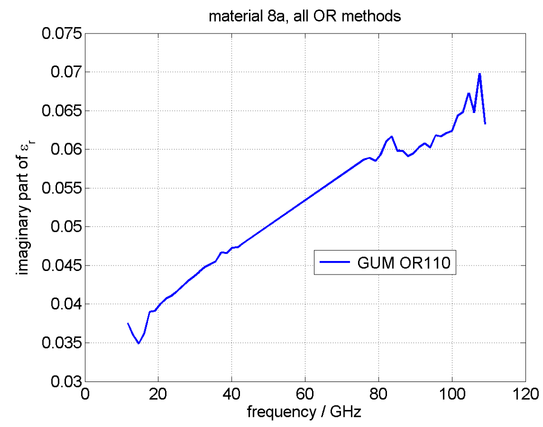

Figure 80: Material 8a measured by open resonator-based methods.

6.1.4 All materials measured using photonic-based methods

This section shows a comparison of all the material samples from Table 3 measured using photonic-based techniques (i.e. TDS, FDS, TDE) by particular institutes.

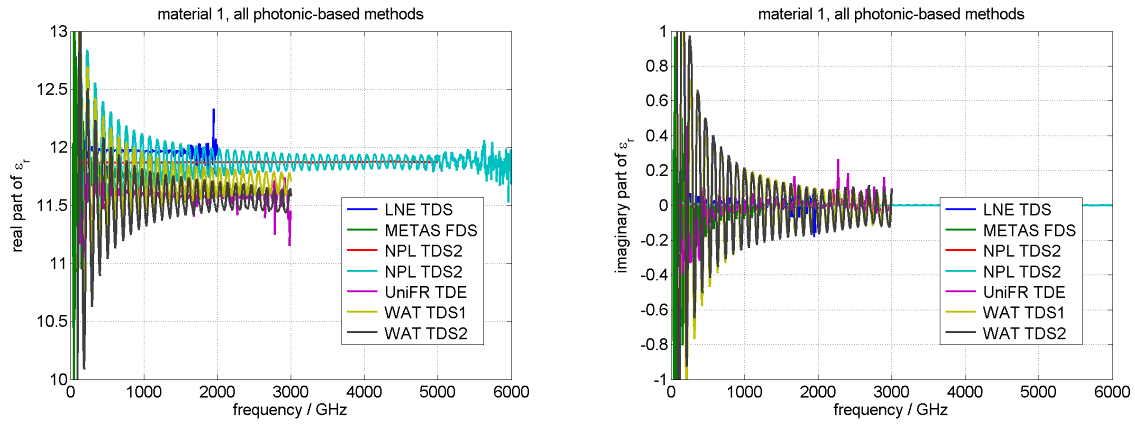

Figure 81: Material 1 (real + imaginary part of ε_r) measured by photonic-based methods.

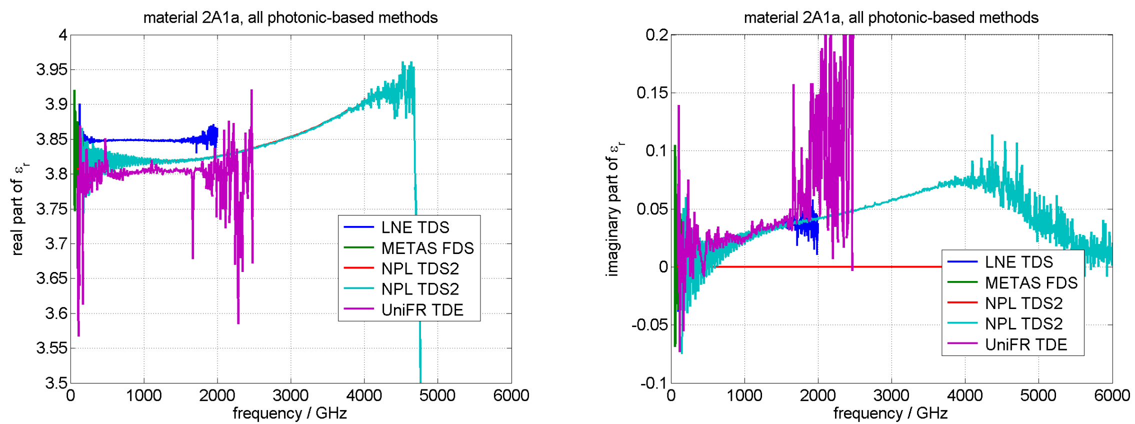

Figure 82: Material 2A1a (real + imaginary part of ε_r) measured by photonic-based methods.

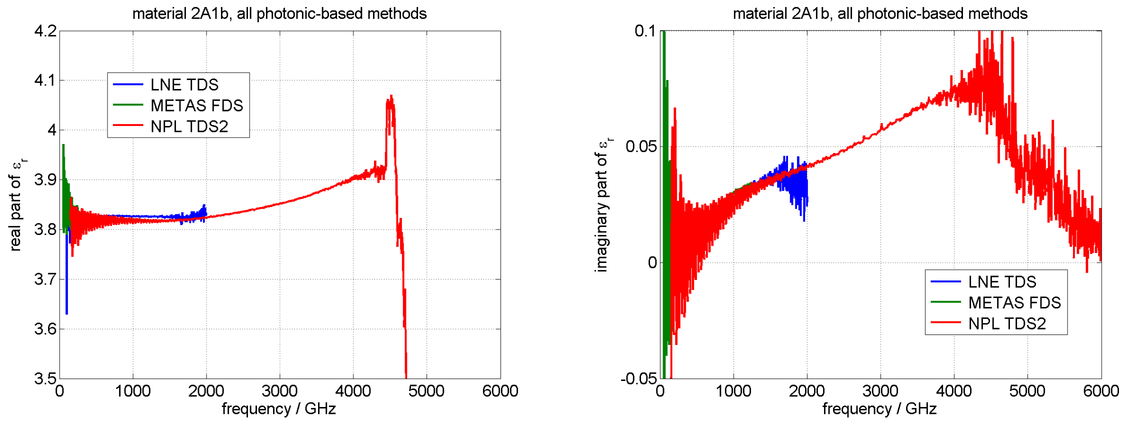

Figure 83: Material 2A1b (real + imaginary part of ε_r) measured by photonic-based methods.

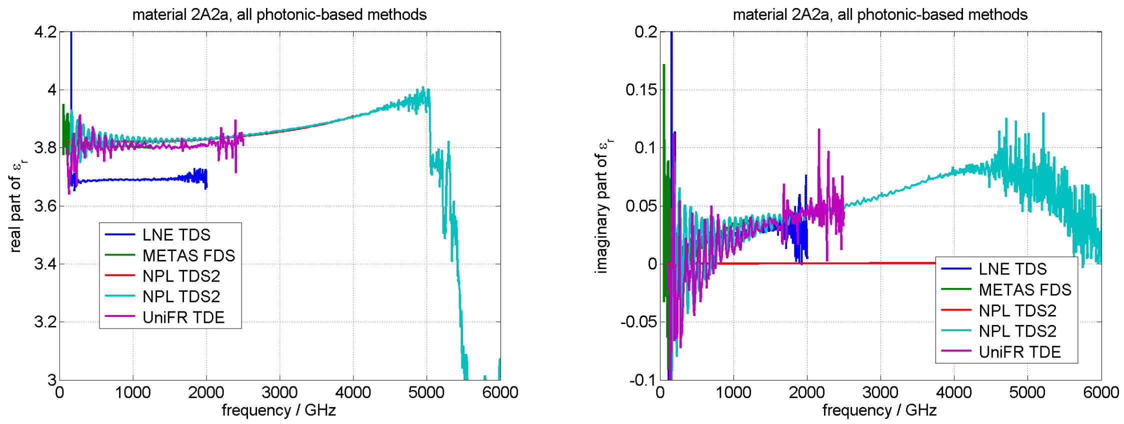

Figure 84: Material 2A2a (real + imaginary part of ε_r) measured by photonic-based methods.

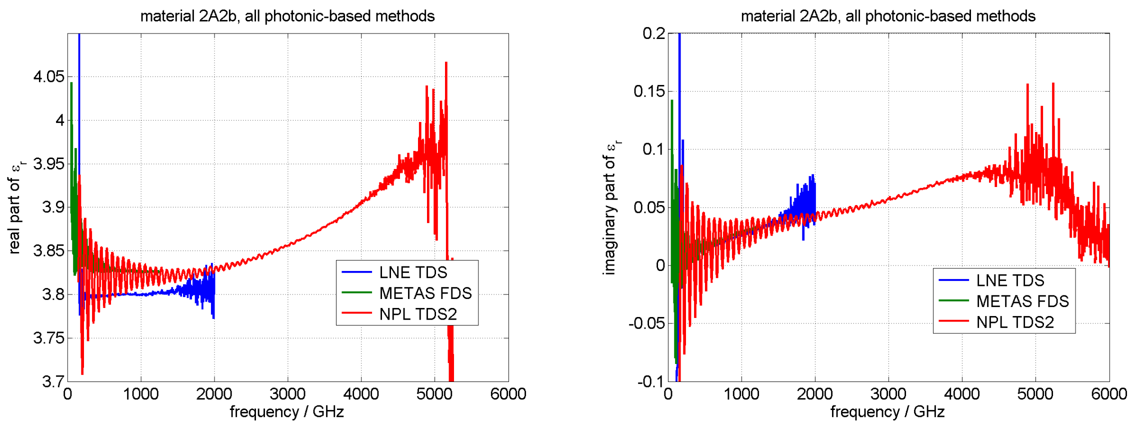

Figure 85: Material 2A2b (real + imaginary part of ε_r) measured by photonic-based methods.

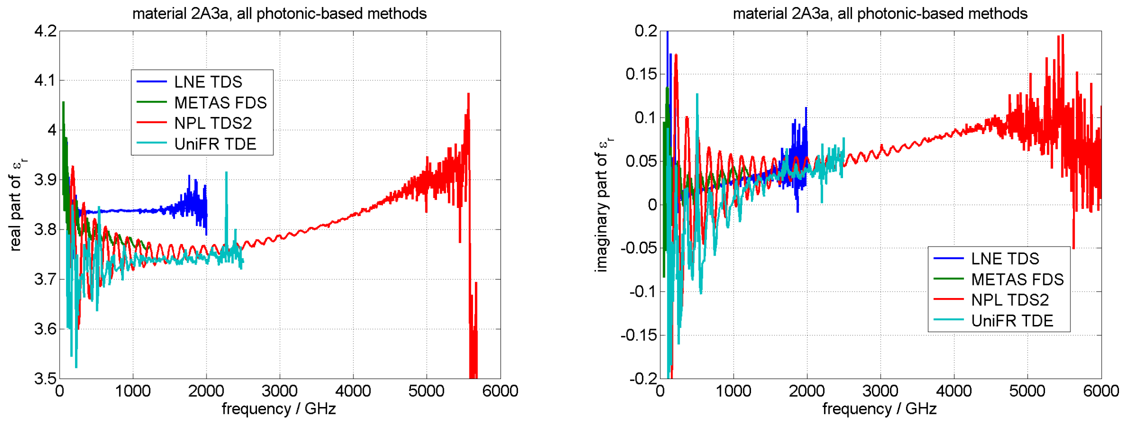

Figure 86: Material 2A3a (real + imaginary part of ε_r) measured by photonic-based methods.

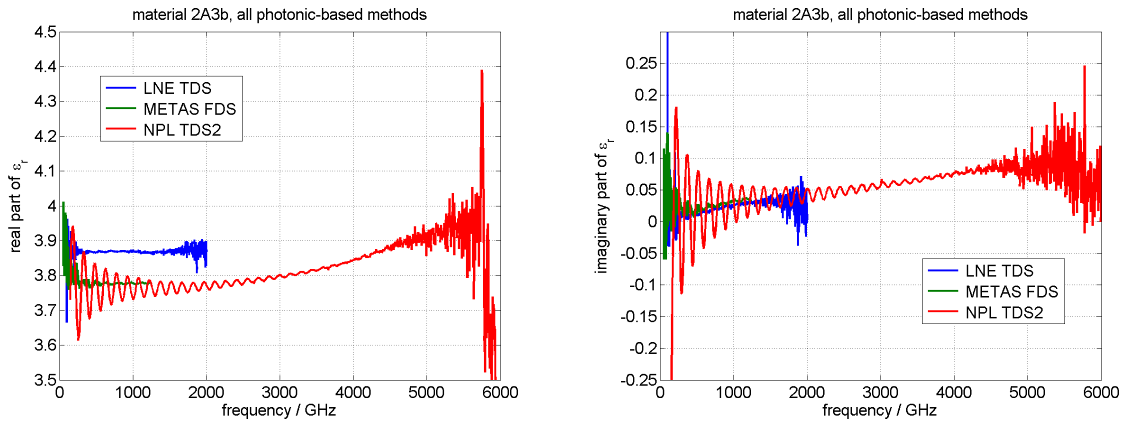

Figure 87: Material 2A3b (real + imaginary part of ε_r) measured by photonic-based methods.

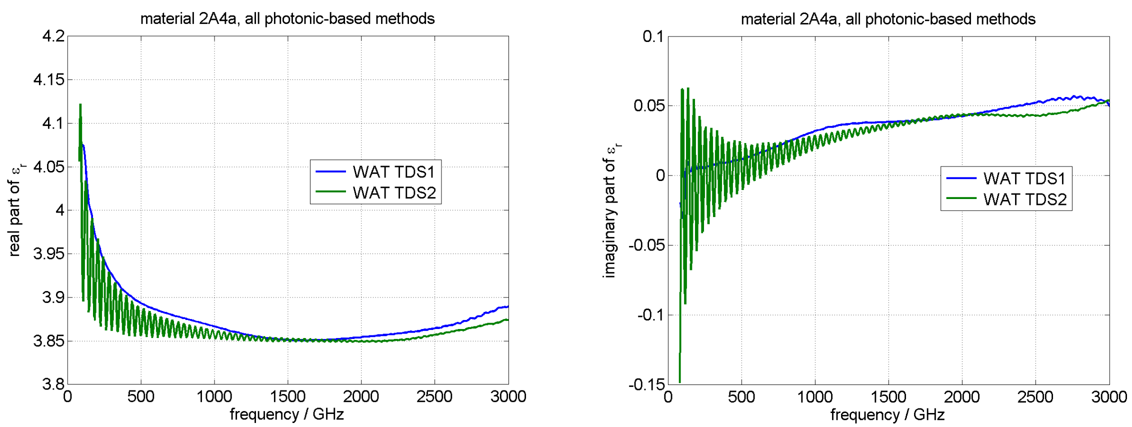

Figure 88: Material 2A4a (real + imaginary part of ε_r) measured by photonic-based methods.

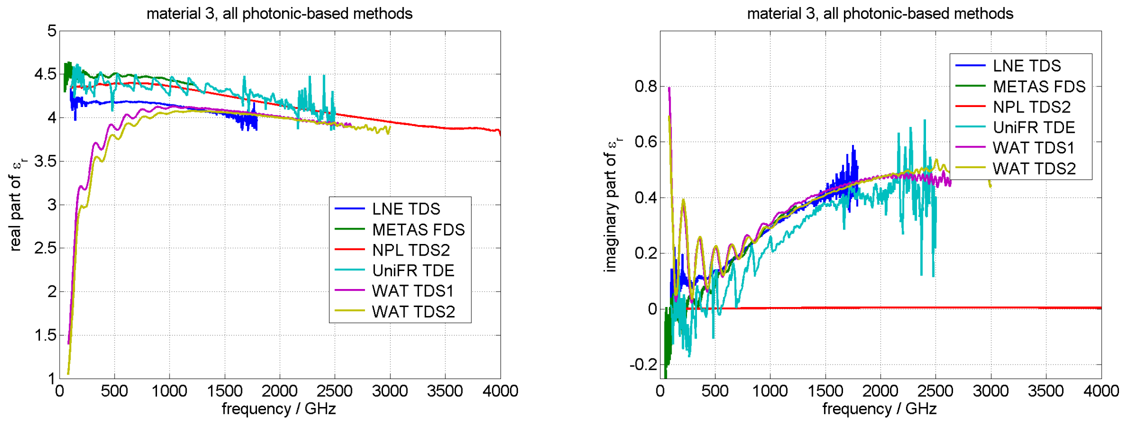

Figure 89: Material 3 (real + imaginary part of ε_r) measured by photonic-based methods.

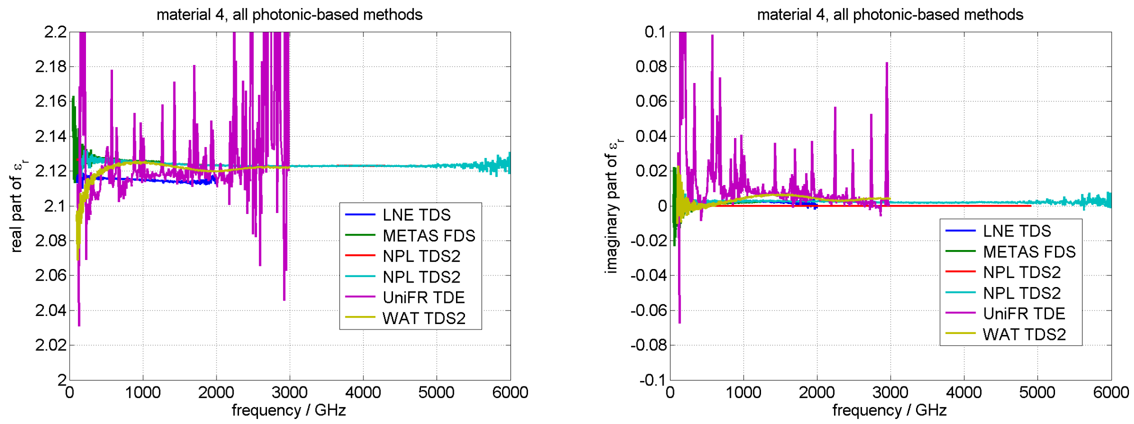

Figure 90: Material 4 (real + imaginary part of ε_r) measured by photonic-based methods.

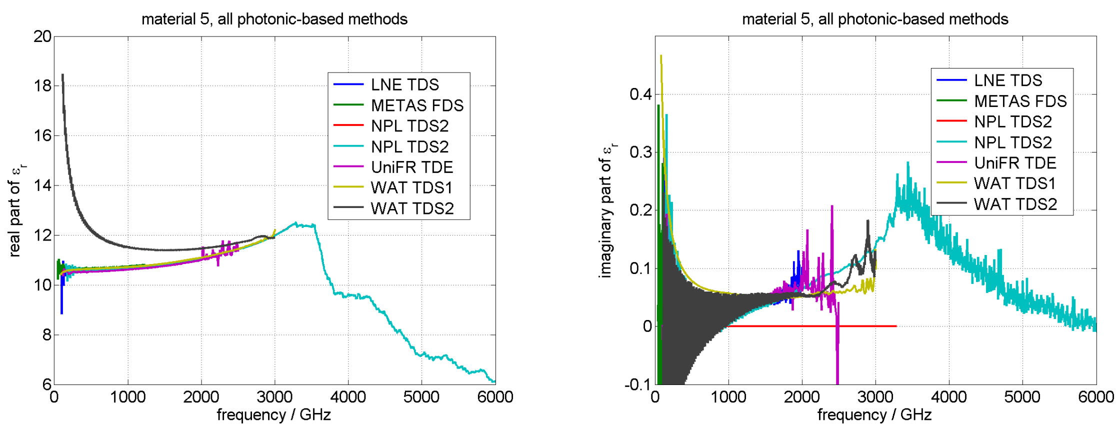

Figure 91: Material 5 (real + imaginary part of ε_r) measured by photonic-based methods.

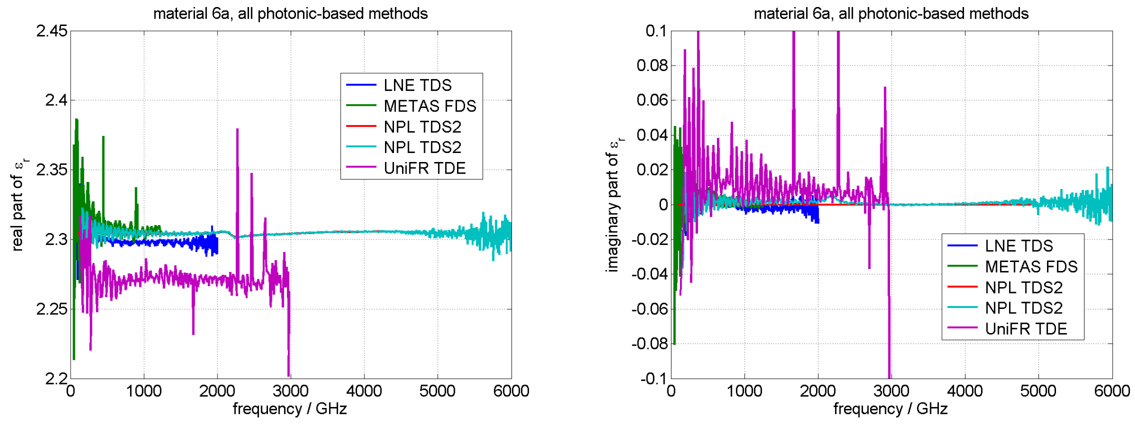

Figure 92: Material 6a (real + imaginary part of ε_r) measured by photonic-based methods.

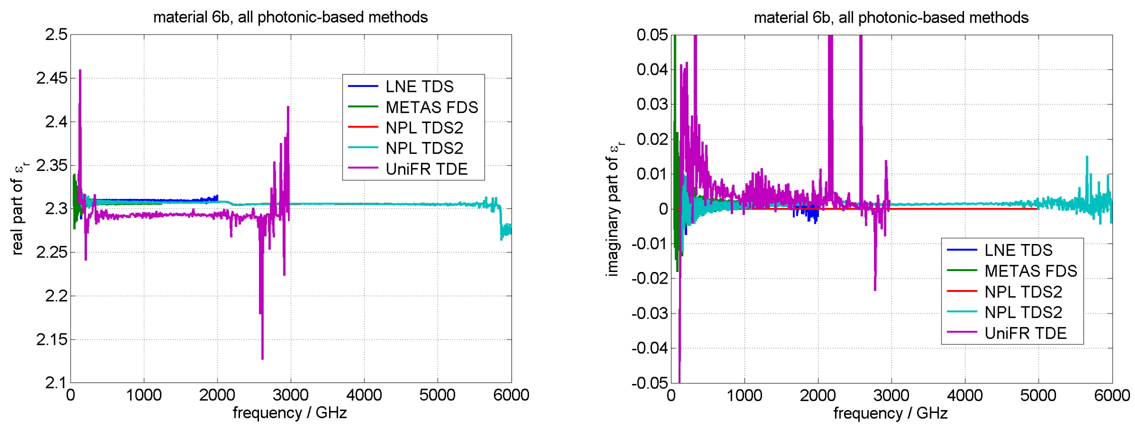

Figure 93: Material 6b (real + imaginary part of ε_r) measured by photonic-based methods.

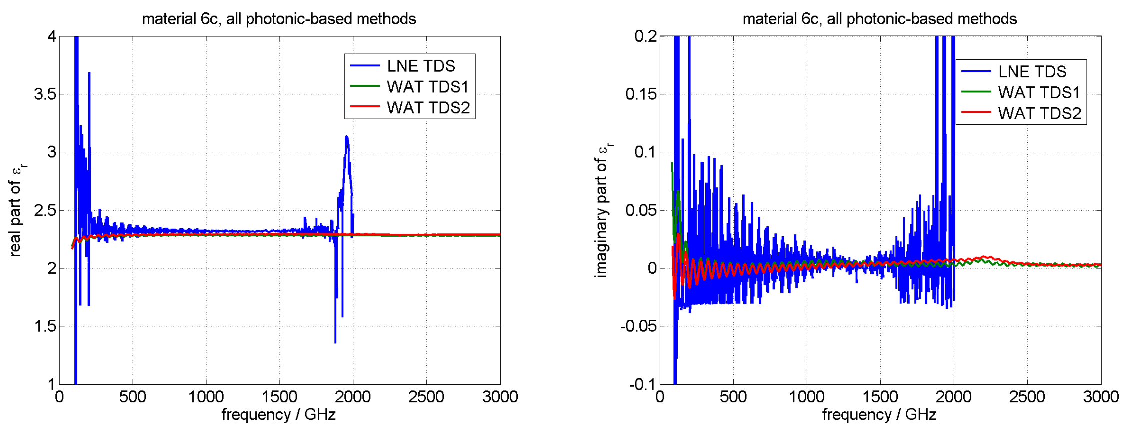

Figure 94: Material 6c (real + imaginary part of ε_r) measured by photonic-based methods.

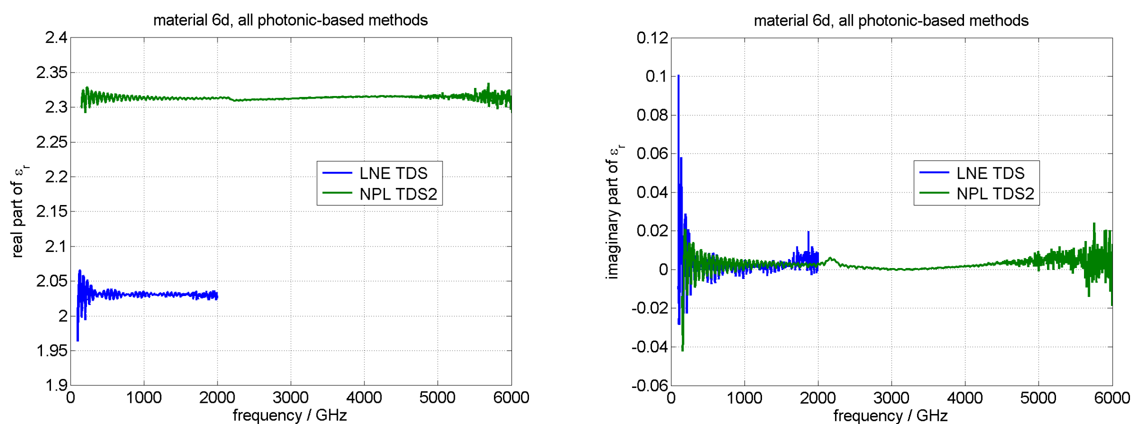

Figure 95: Material 6d (real + imaginary part of ε_r) measured by photonic-based methods.

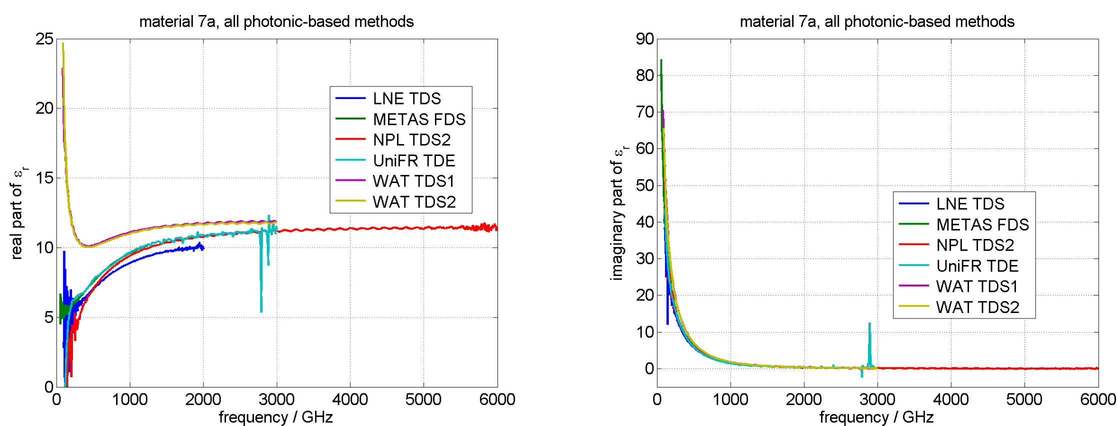

Figure 96: Material 7a (real + imaginary part of ε_r) measured by photonic-based methods.

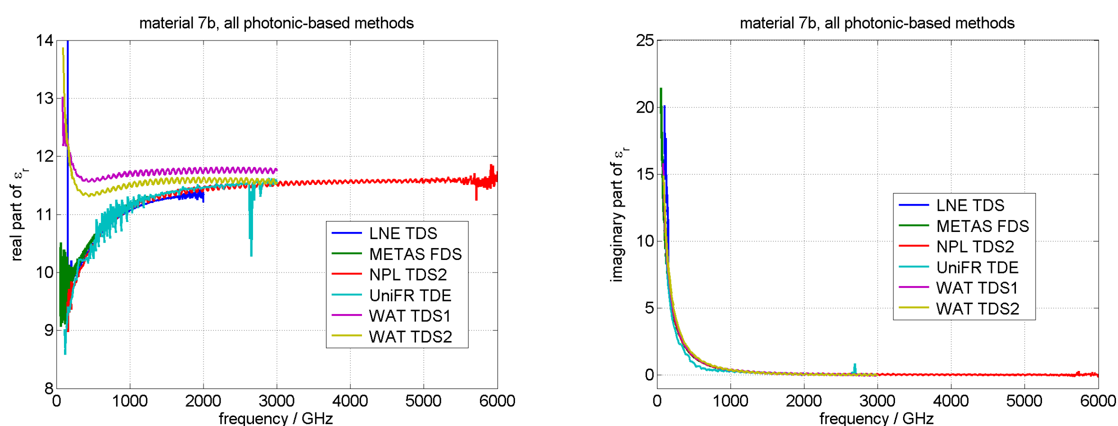

Figure 97: Material 7b (real + imaginary part of ε_r) measured by photonic-based methods.

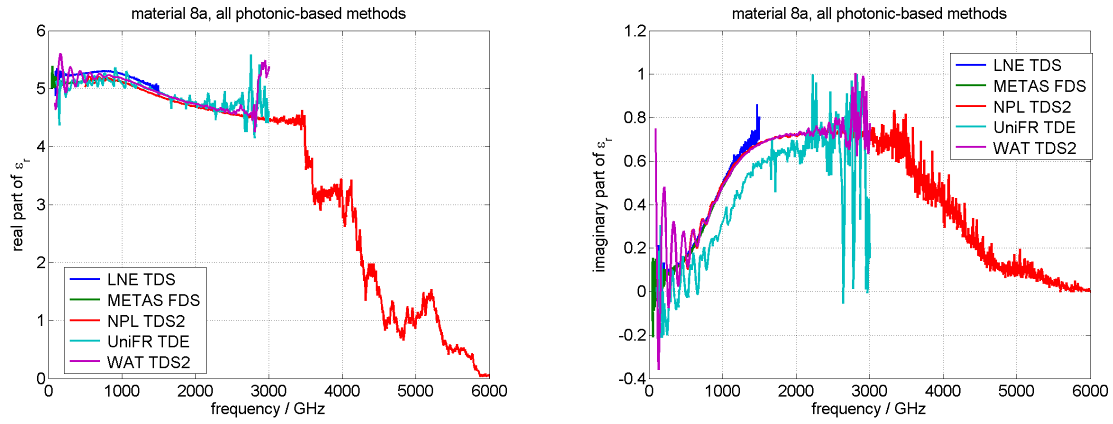

Figure 98: Material 8a (real + imaginary part of ε_r) measured by photonic-based methods.

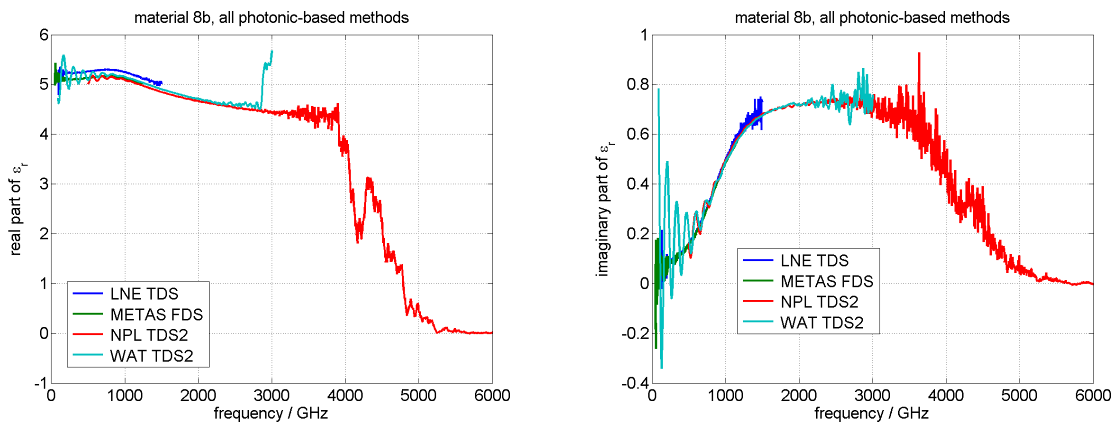

Figure 99: Material 8b (real + imaginary part of ε_r) measured by photonic-based methods.

6.1.5 One material measured using all methods

This section shows all the material samples from Table 3 measured by all techniques and all participants, where applicable. Both the full frequency scale up to several THz and a detail (frequency range 50 GHz to 750 GHz) are shown.

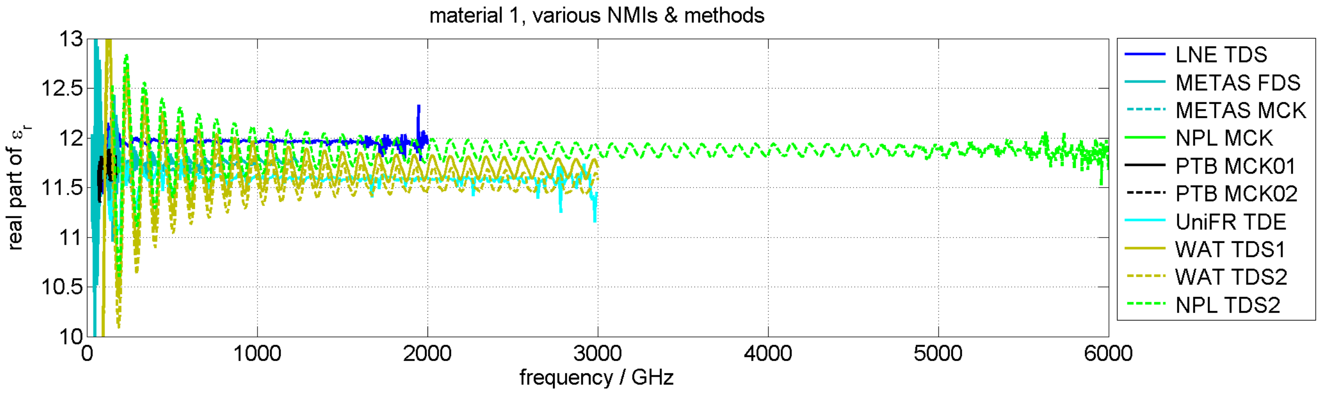

Figure 100: Material 1 (real part of ε_r) comparison of all methods.

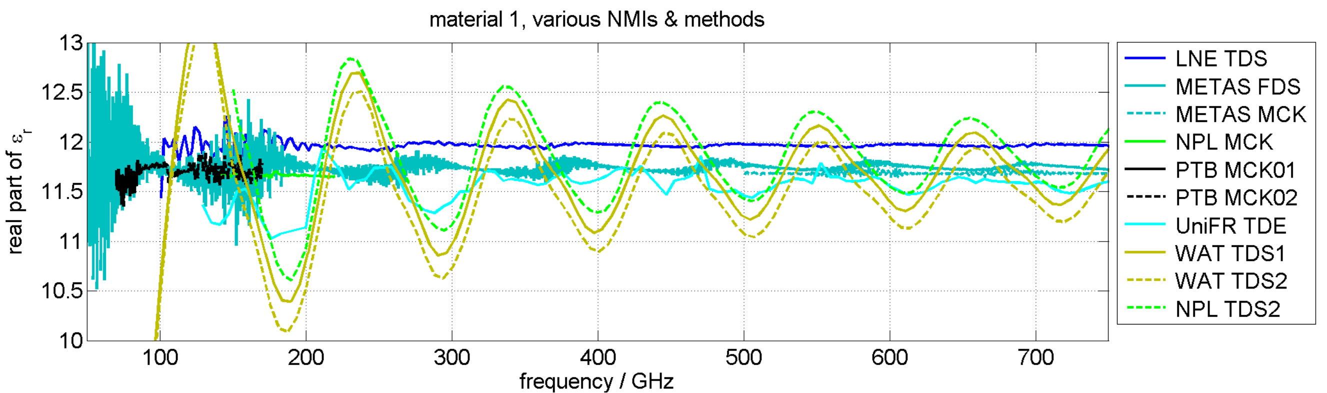

Figure 101: Material 1 (real part of ε_r) comparison of all methods 750G.

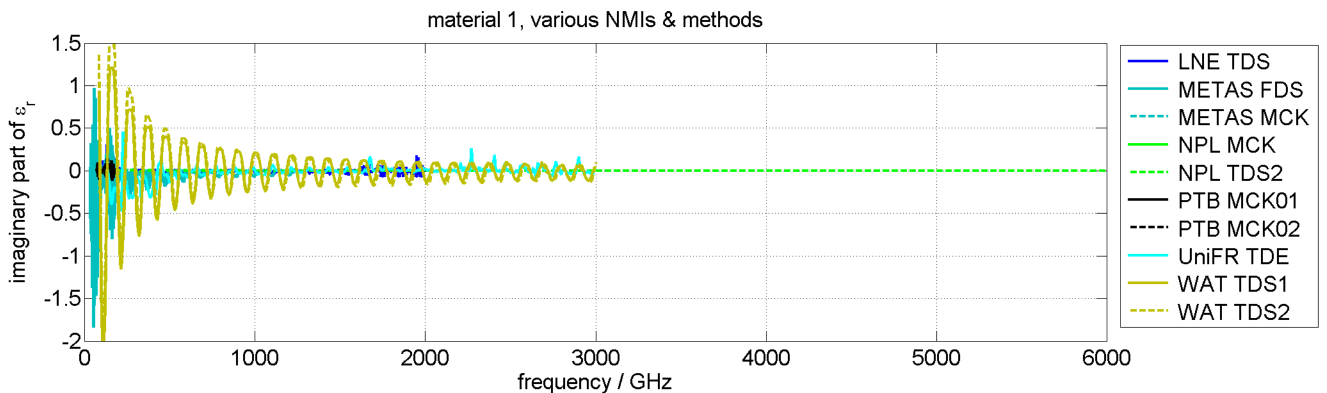

Figure 102: Material 1 (imaginary part of ε_r) comparison of all methods.

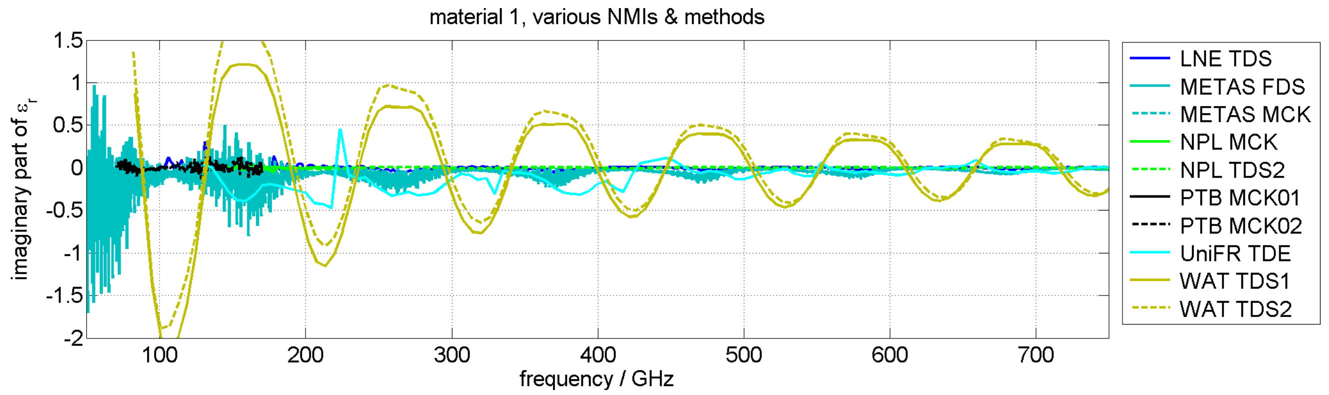

Figure 103: Material 1 (imaginary part of ε_r) comparison of all methods 750G.

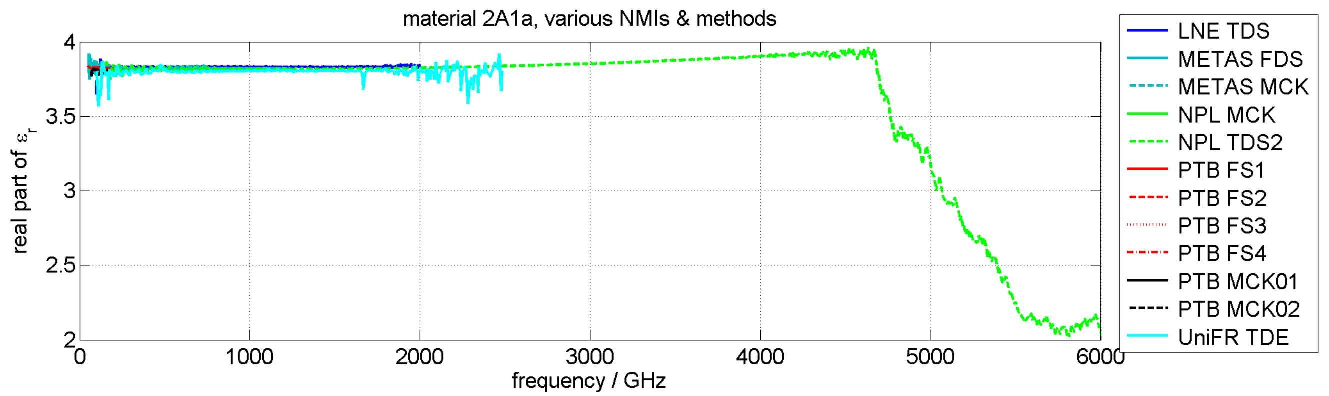

Figure 104: Material 2A1a (real part of ε_r) comparison of all methods.

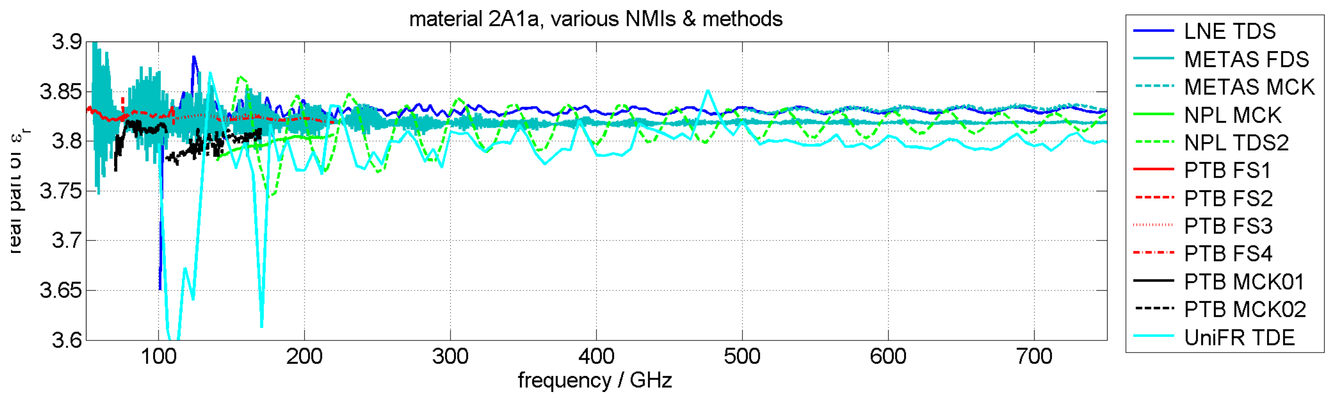

Figure 105: Material 2A1a (real part of ε_r) comparison of all methods 750G.

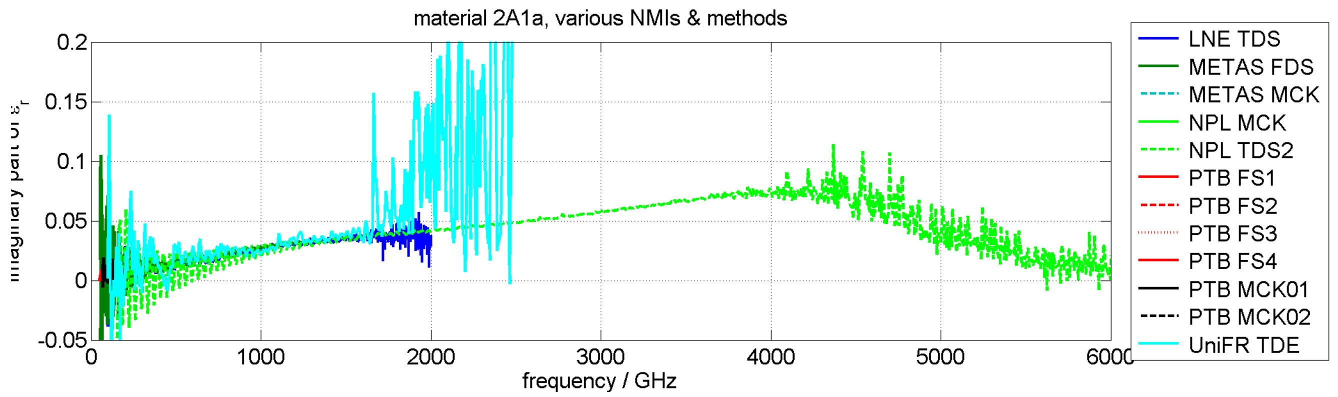

Figure 106: Material 2A1a (imaginary part of ε_r) comparison of all methods.

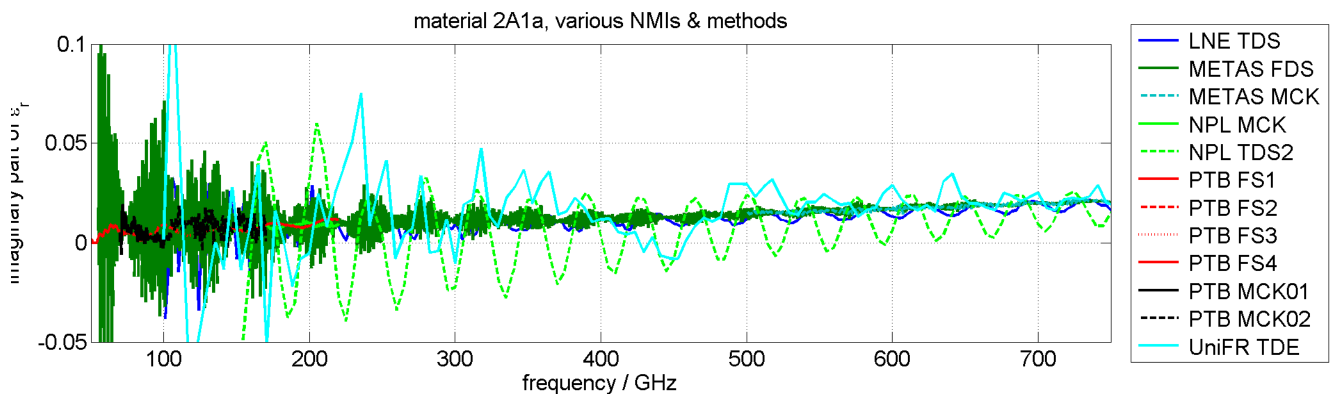

Figure 107: Material 2A1a (imaginary part of ε_r) comparison of all methods 750G.

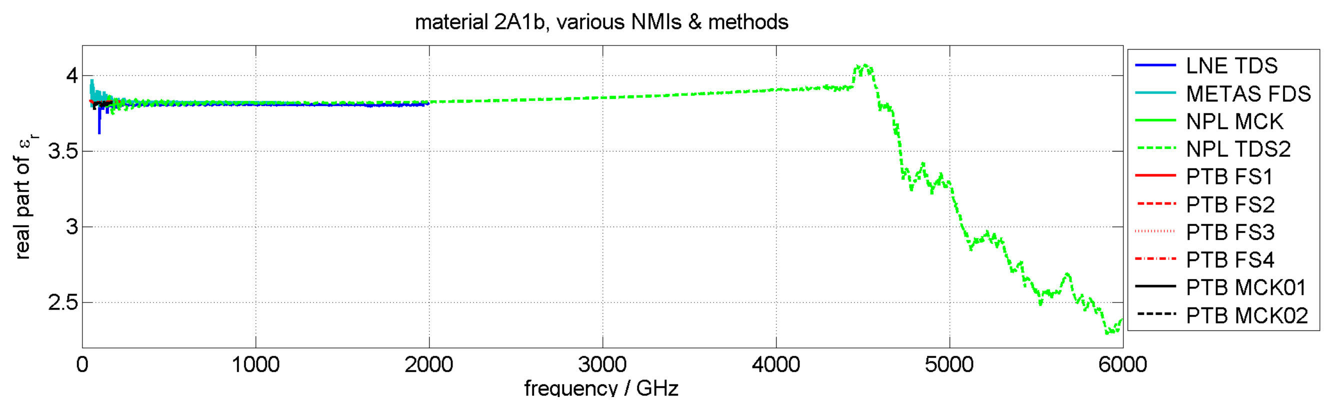

Figure 108: Material 2A1b (real part of ε_r) comparison of all methods.

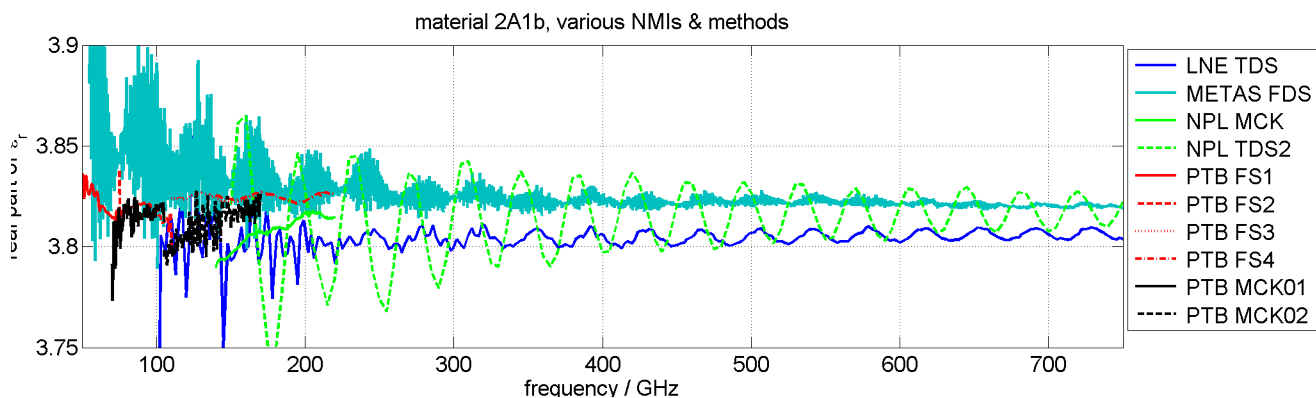

Figure 109: Material 2A1b (real part of ε_r) comparison of all methods 750G.

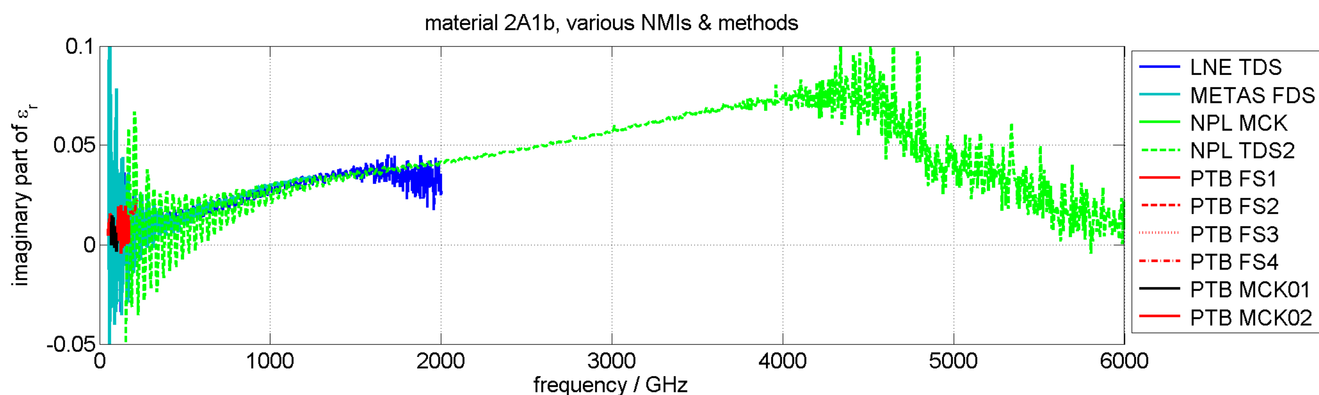

Figure 110: Material 2A1b (imaginary part of ε_r) comparison of all methods.

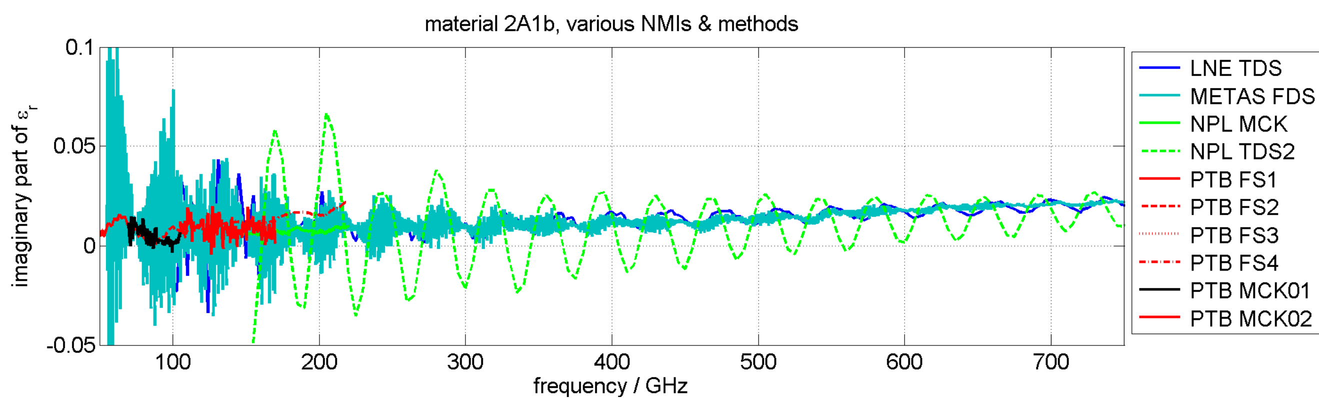

Figure 111: Material 2A1b (imaginary part of ε_r) comparison of all methods 750G.

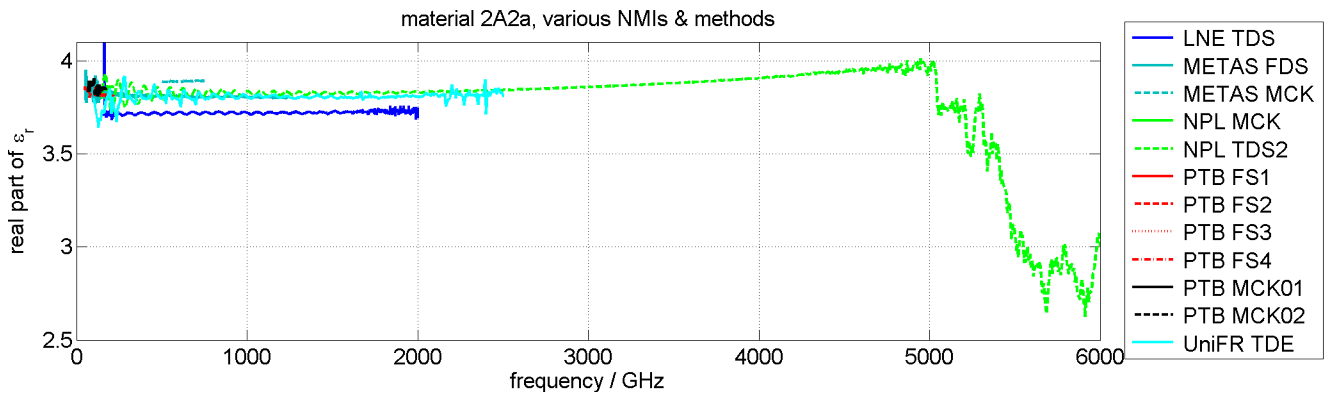

Figure 112: Material 2A2a (real part of ε_r) comparison of all methods.

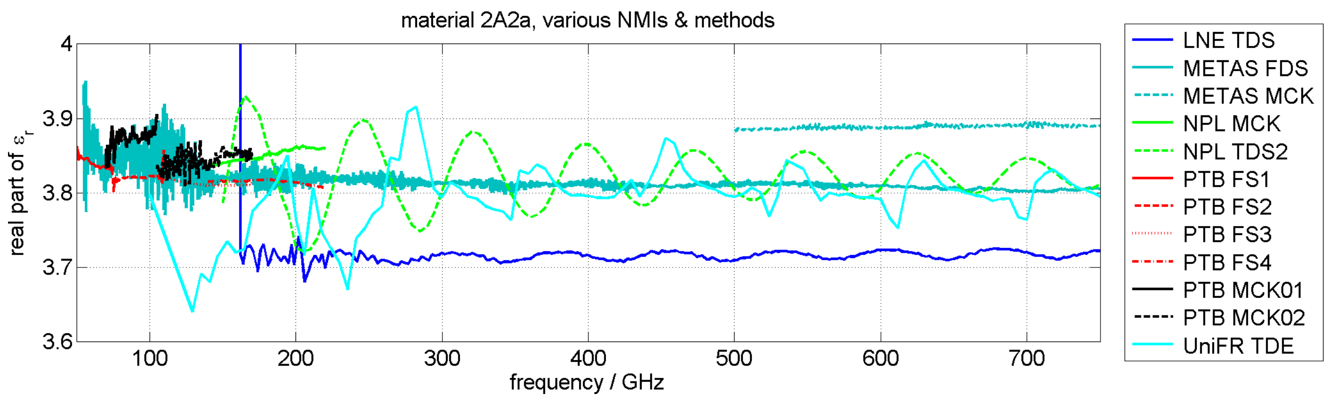

Figure 113: Material 2A2a (real part of ε_r) comparison of all methods 750G.

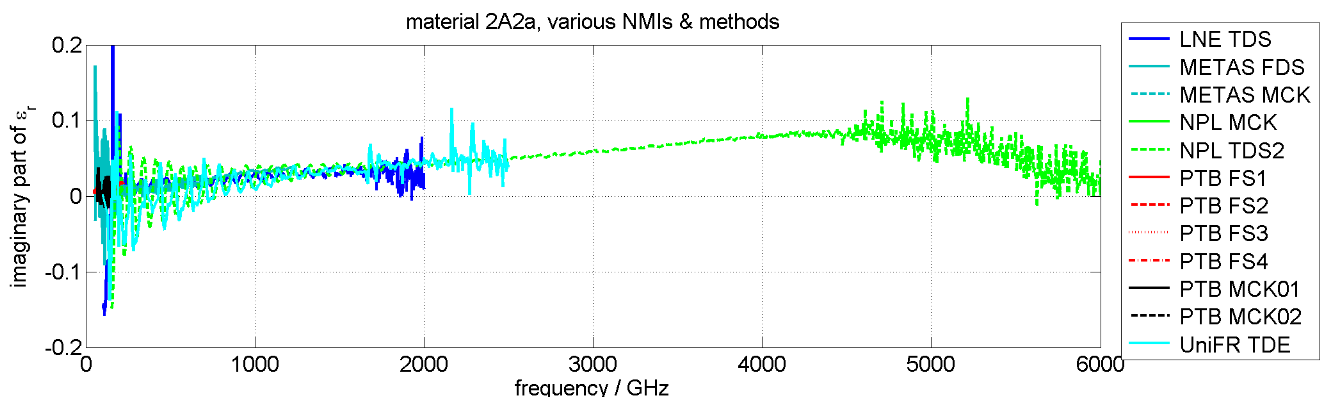

Figure 114: Material 2A2a (imaginary part of ε_r) comparison of all methods.

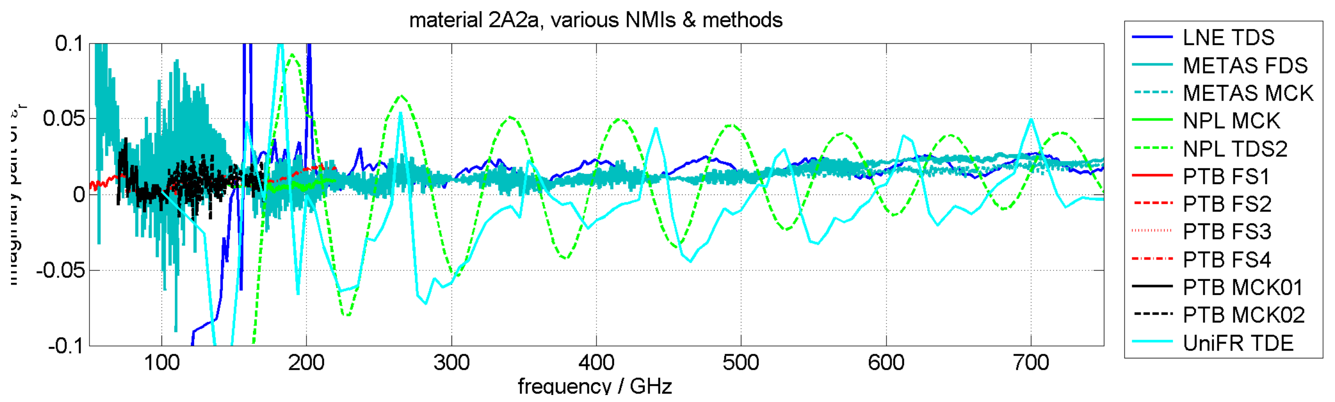

Figure 115: Material 2A2a (imaginary part of ε_r) comparison of all methods 750G.

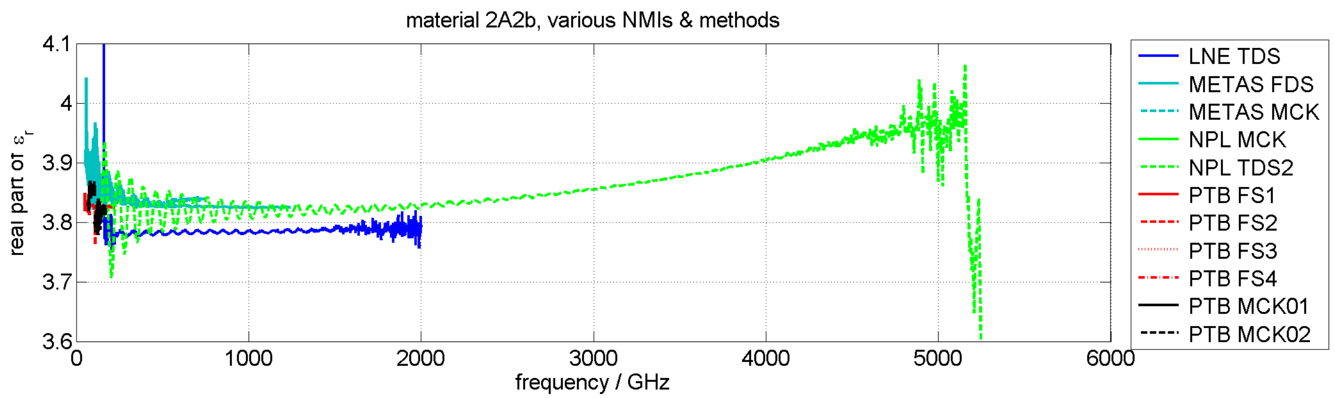

Figure 116: Material 2A2b (real part of ε_r) comparison of all methods.

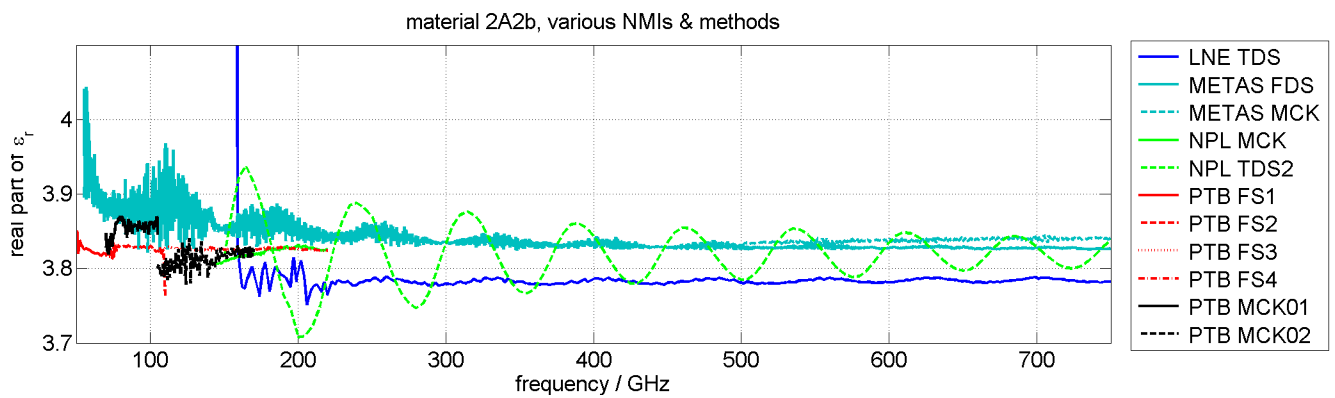

Figure 117: Material 2A2b (real part of ε_r) comparison of all methods 750G.

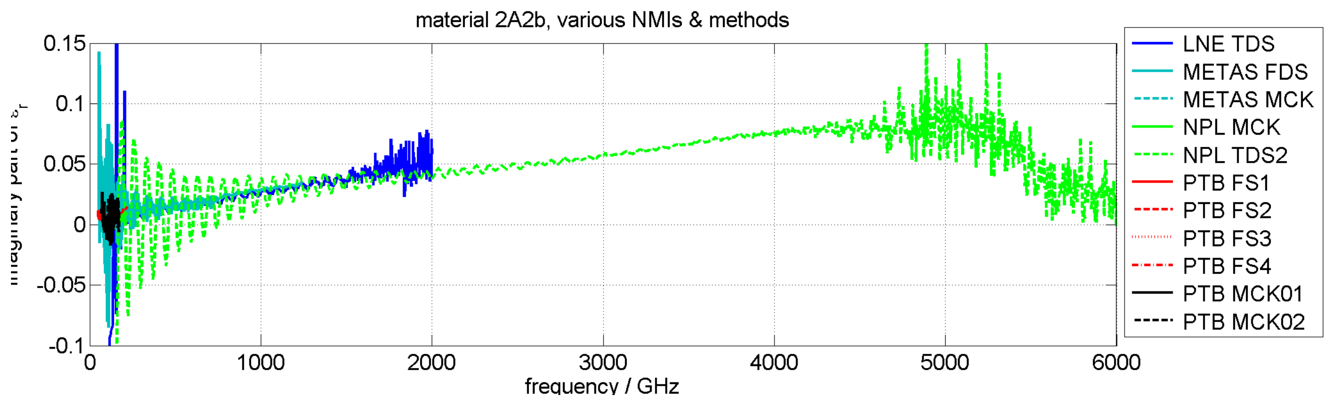

Figure 118: Material 2A2b (imaginary part of ε_r) comparison of all methods.

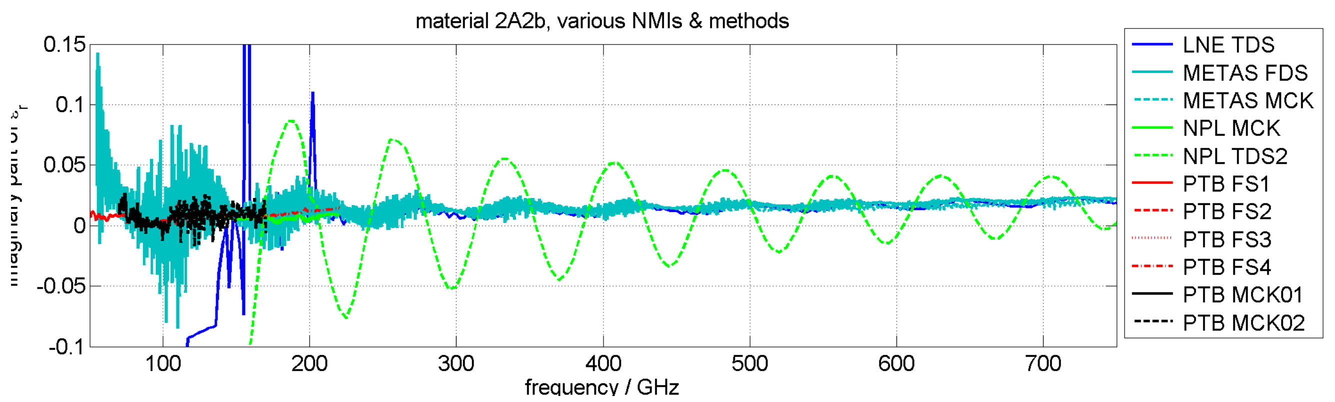

Figure 119: Material 2A2b (imaginary part of ε_r) comparison of all methods 750G.

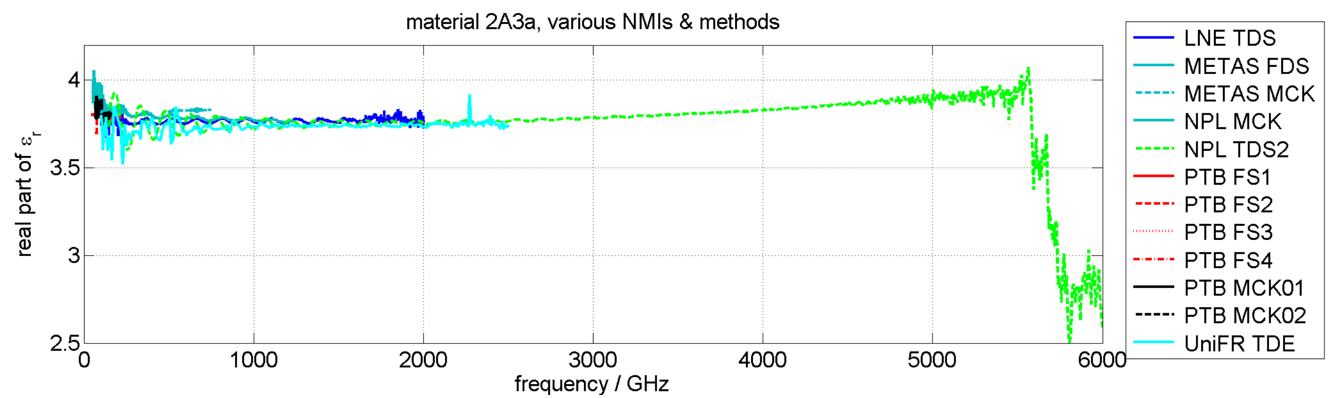

Figure 120: Material 2A3a (real part of ε_r) comparison of all methods.

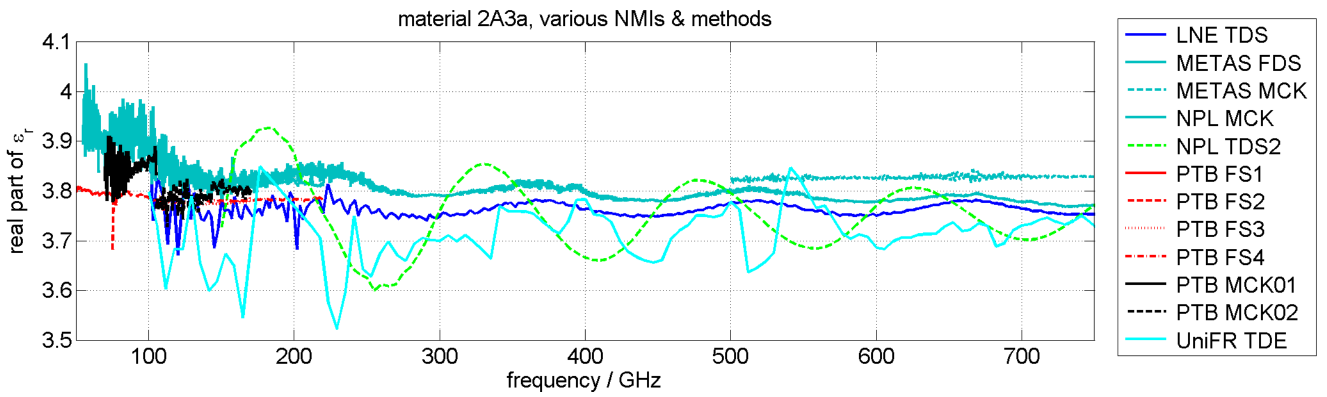

Figure 121: Material 2A3a (real part of ε_r) comparison of all methods 750G.

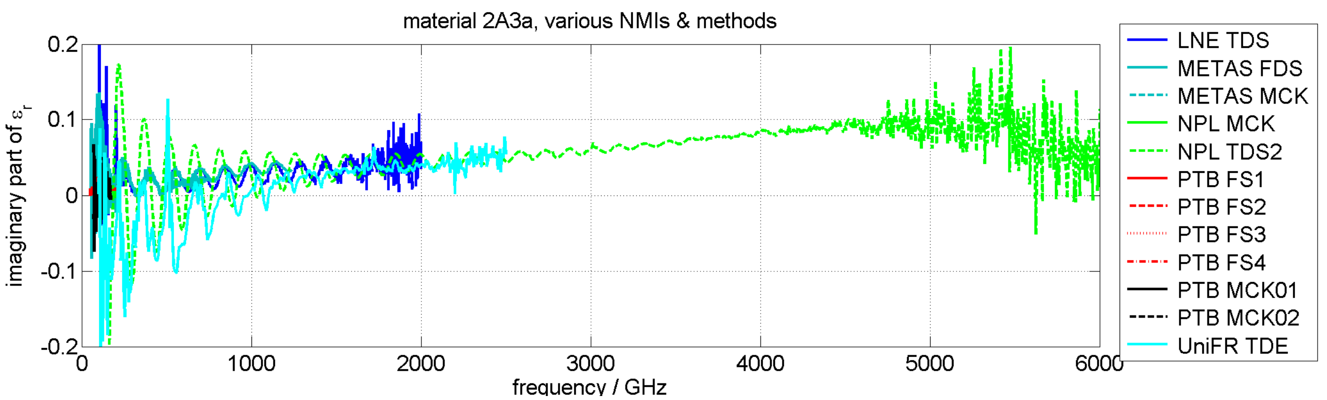

Figure 122: Material 2A3a (imaginary part of ε_r) comparison of all methods.

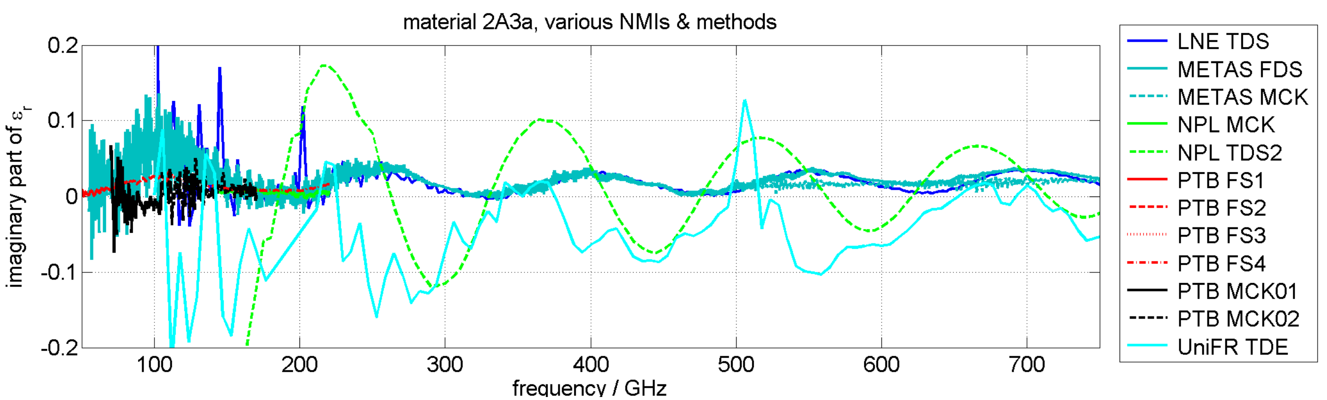

Figure 123: Material 2A3a (imaginary part of ε_r) comparison of all methods 750G.

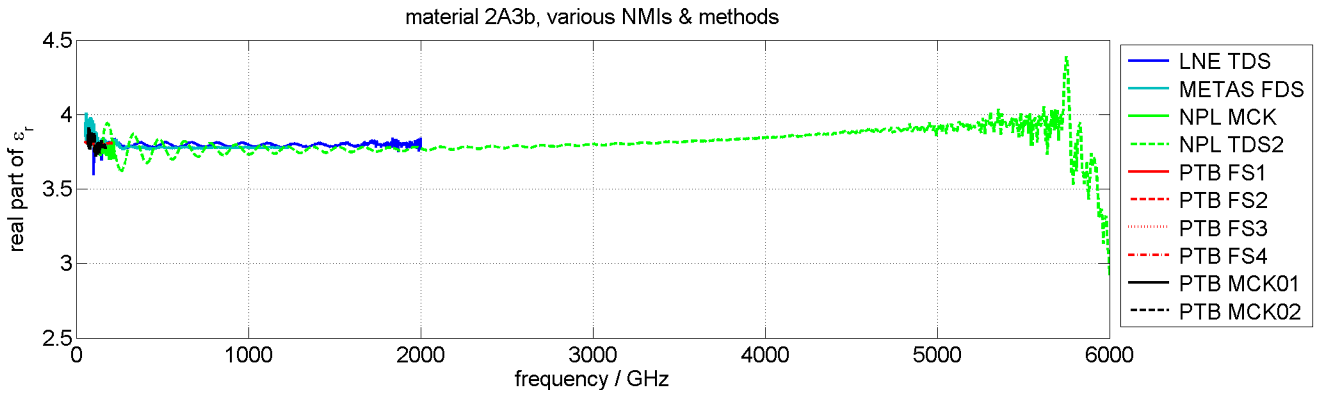

Figure 124: Material 2A3b (real part of ε_r) comparison of all methods.

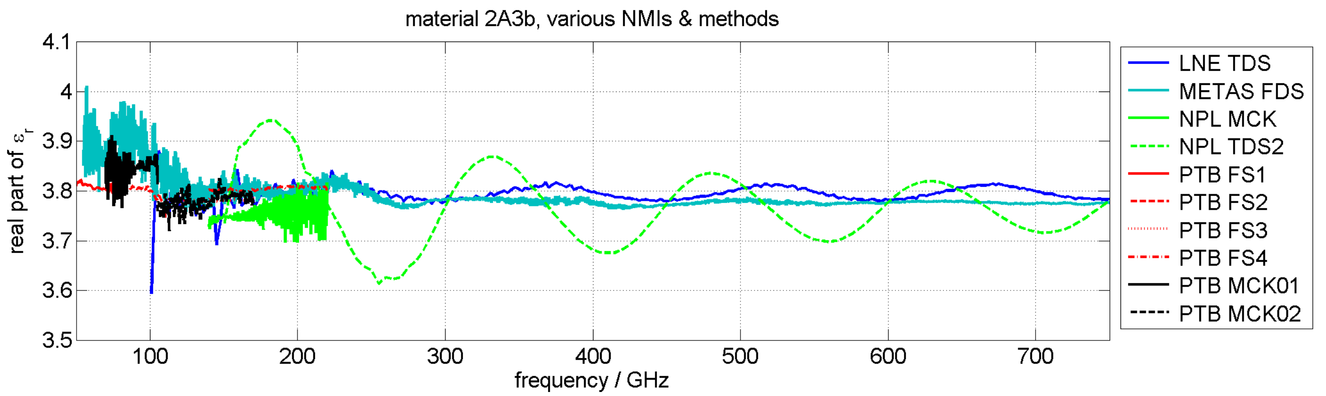

Figure 125: Material 2A3b (real part of ε_r) comparison of all methods 750G.

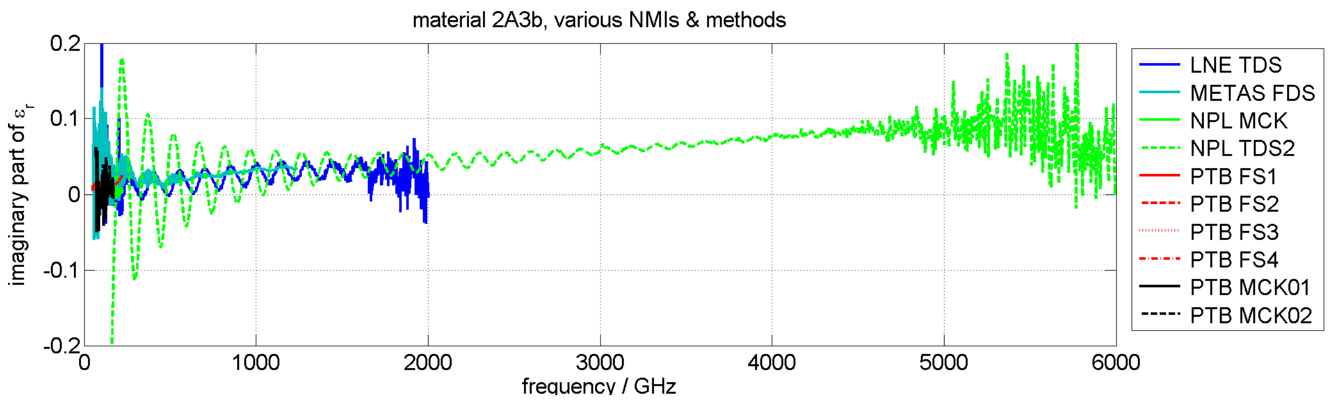

Figure 126: Material 2A3b (imaginary part of ε_r) comparison of all methods.

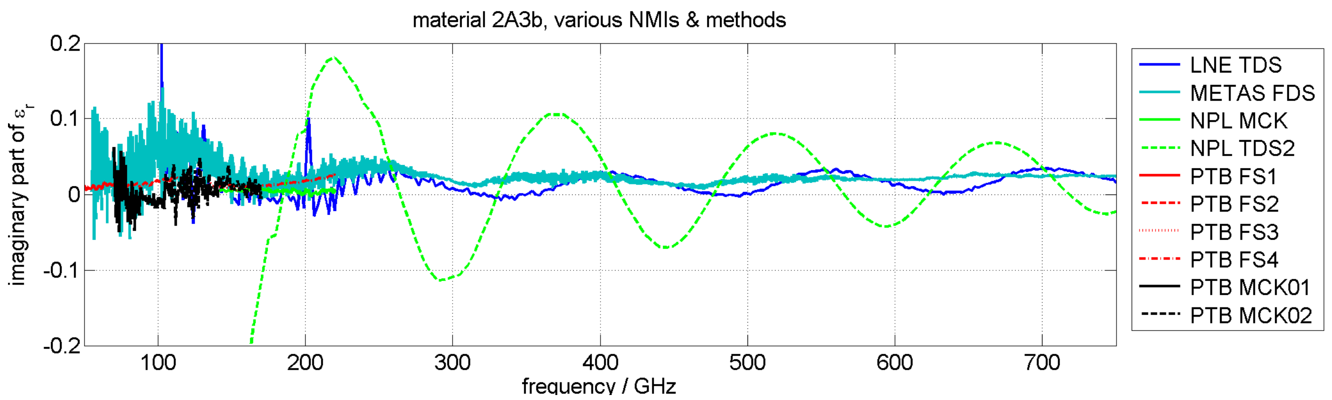

Figure 127: Material 2A3b (imaginary part of ε_r) comparison of all methods 750G.

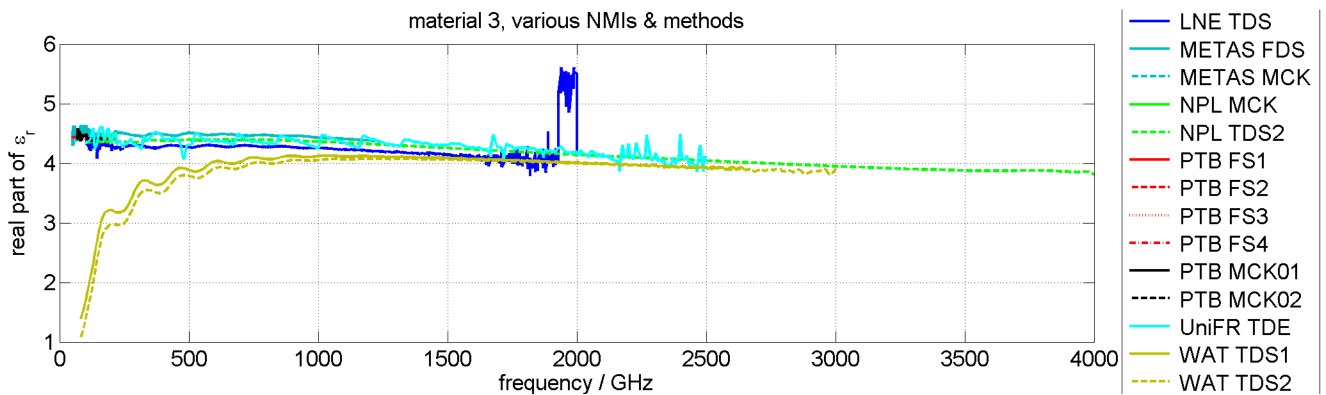

Figure 128: Material 3 (real part of ε_r) comparison of all methods.

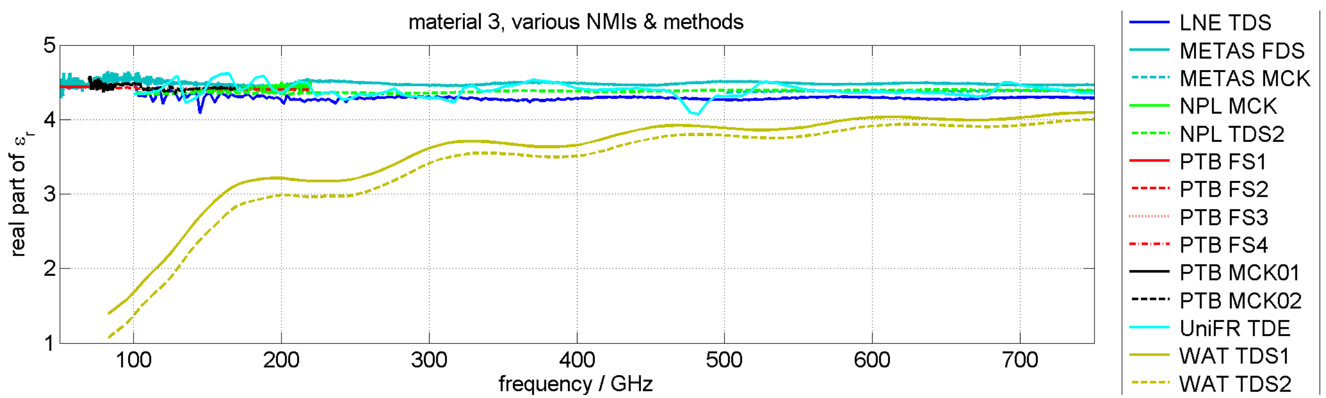

Figure 129: Material 3 (real part of ε_r) comparison of all methods 750G.

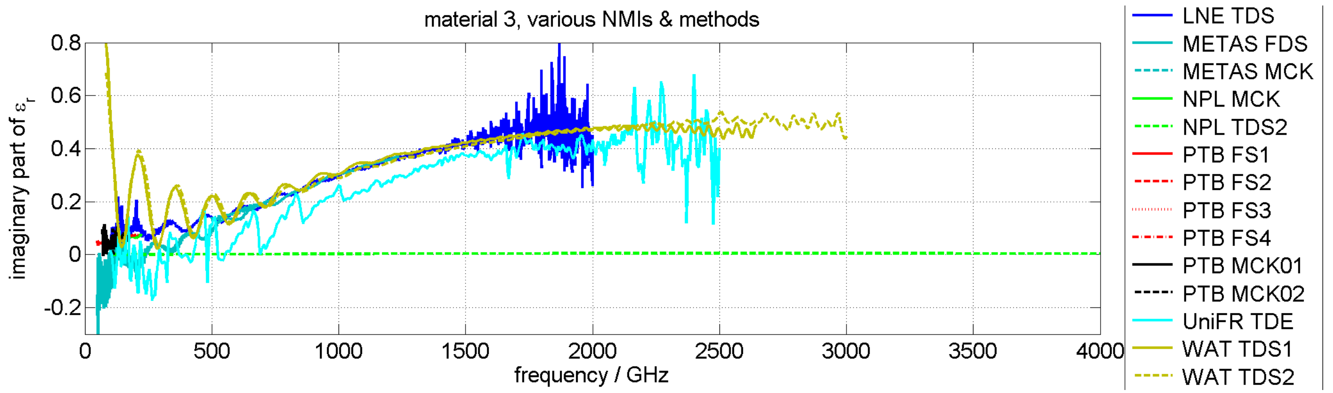

Figure 130: Material 3 (imaginary part of ε_r) comparison of all methods.

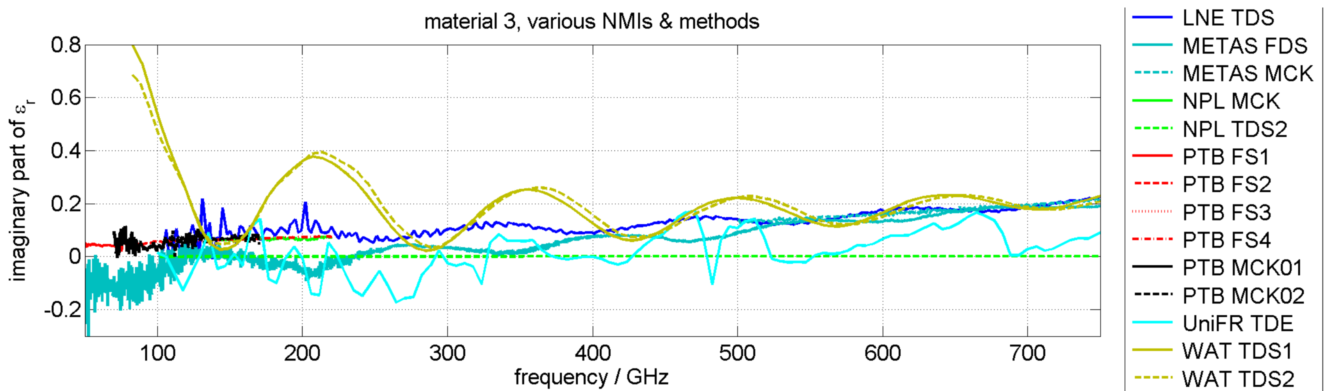

Figure 131: Material 3 (imaginary part of ε_r) comparison of all methods 750G.

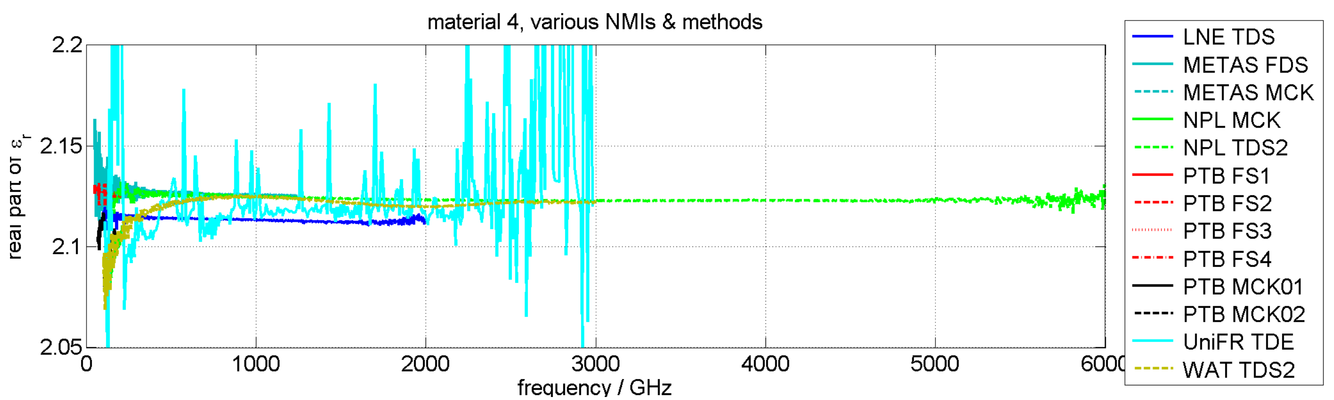

Figure 132: Material 4 (real part of ε_r) comparison of all methods.

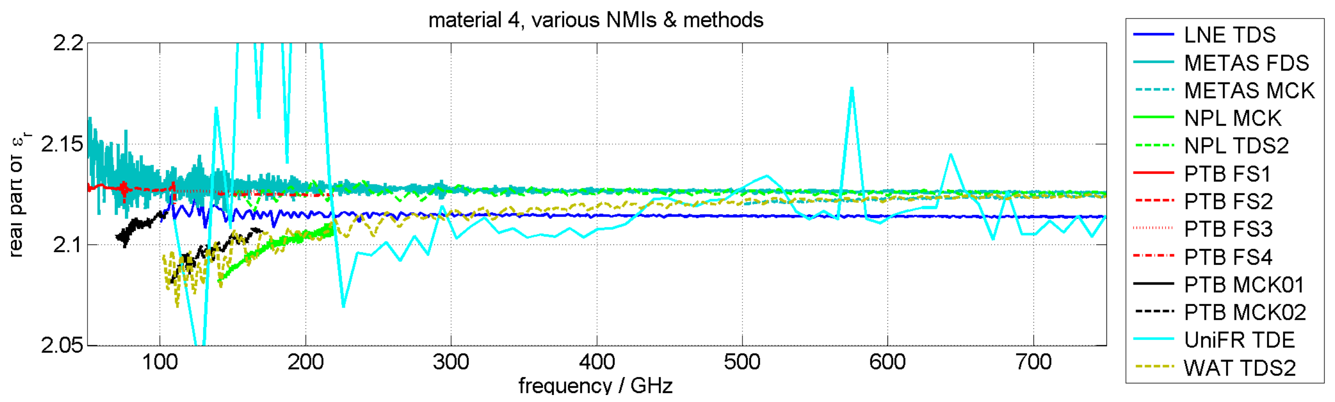

Figure 133: Material 4 (real part of ε_r) comparison of all methods 750G.

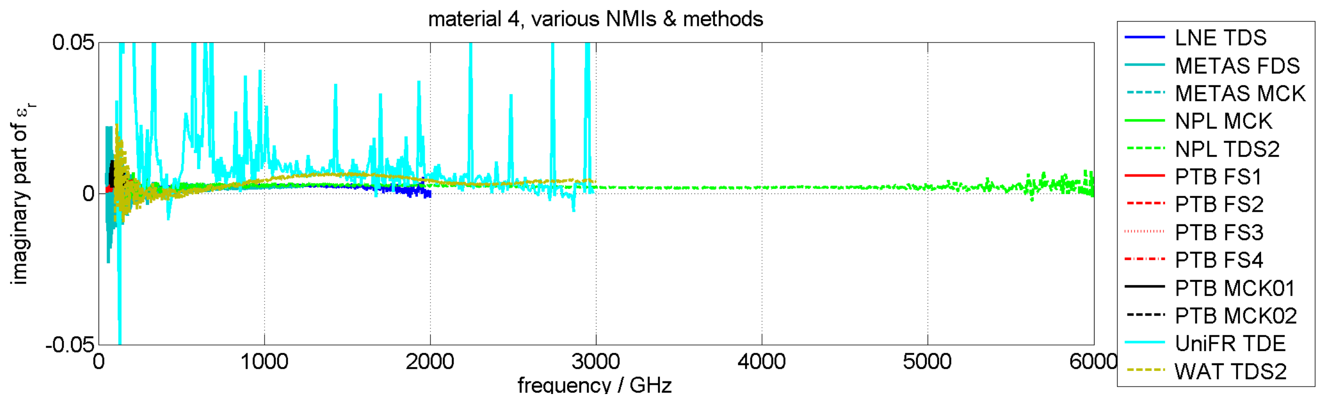

Figure 134: Material 4 (imaginary part of ε_r) comparison of all methods.

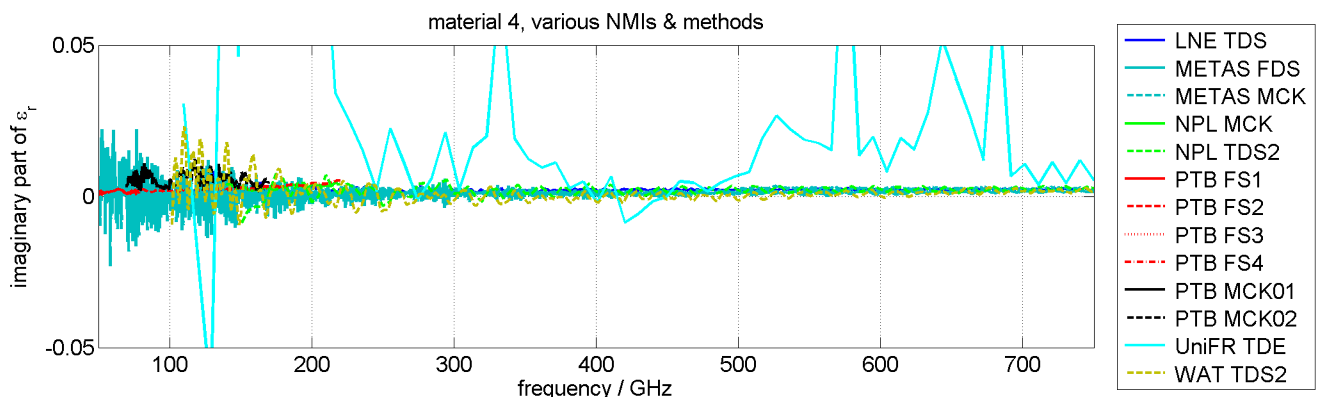

Figure 135: Material 4 (imaginary part of ε_r) comparison of all methods 750G.

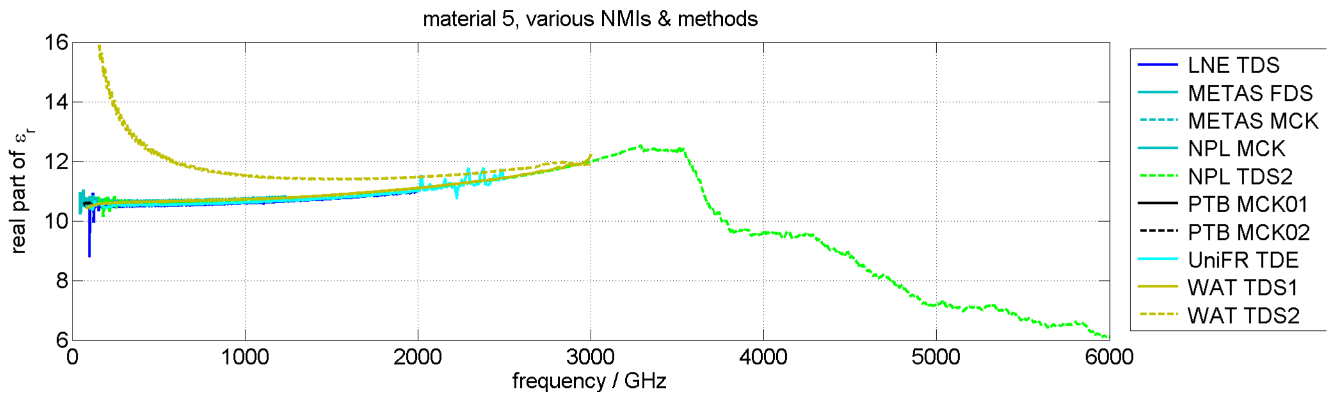

Figure 136: Material 5 (real part of ε_r) comparison of all methods.

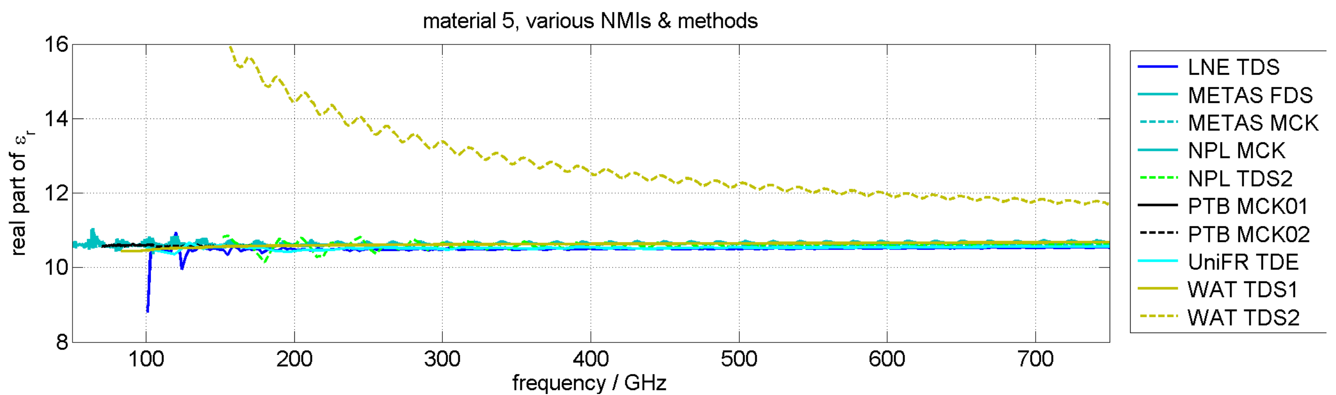

Figure 137: Material 5 (real part of ε_r) comparison of all methods 750G.

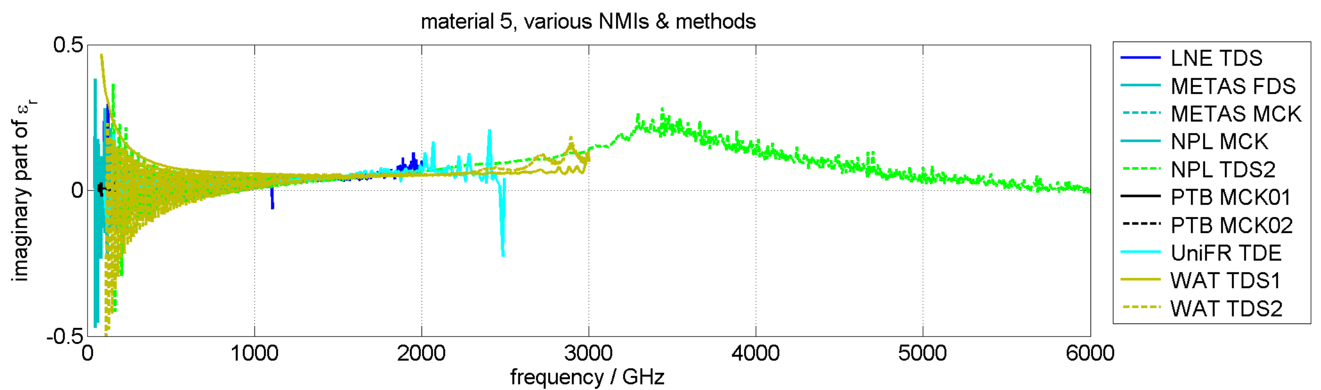

Figure 138: Material 5 (imaginary part of ε_r) comparison of all methods.

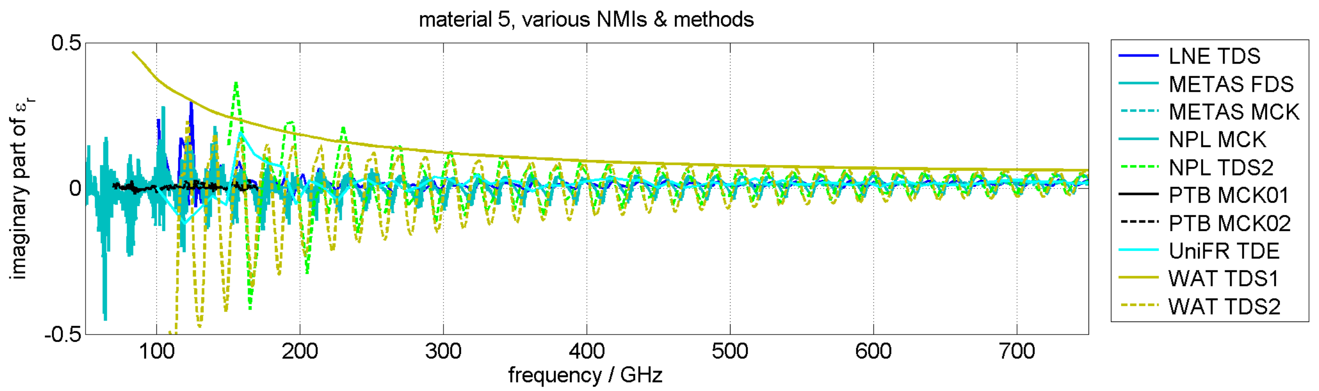

Figure 139: Material 5 (imaginary part of ε_r) comparison of all methods 750G.

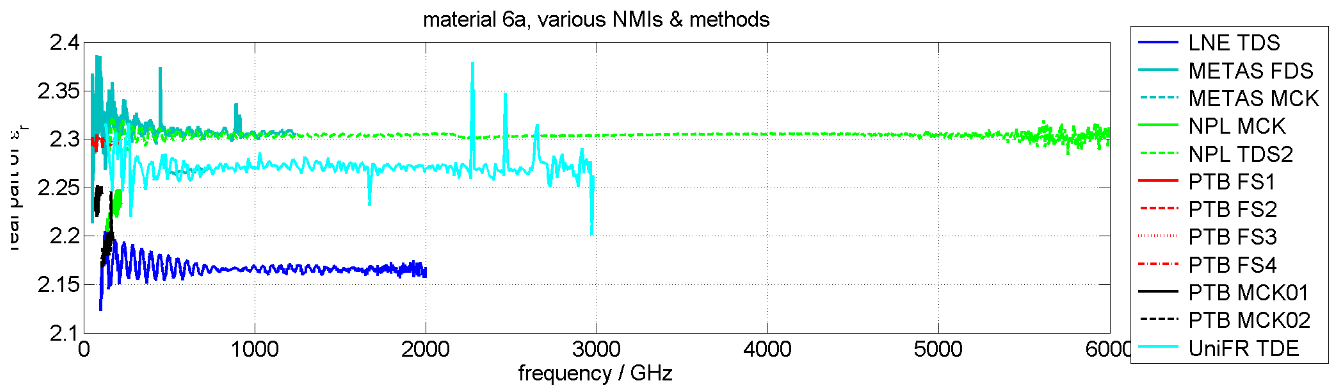

Figure 140: Material 6a (real part of ε_r) comparison of all methods.

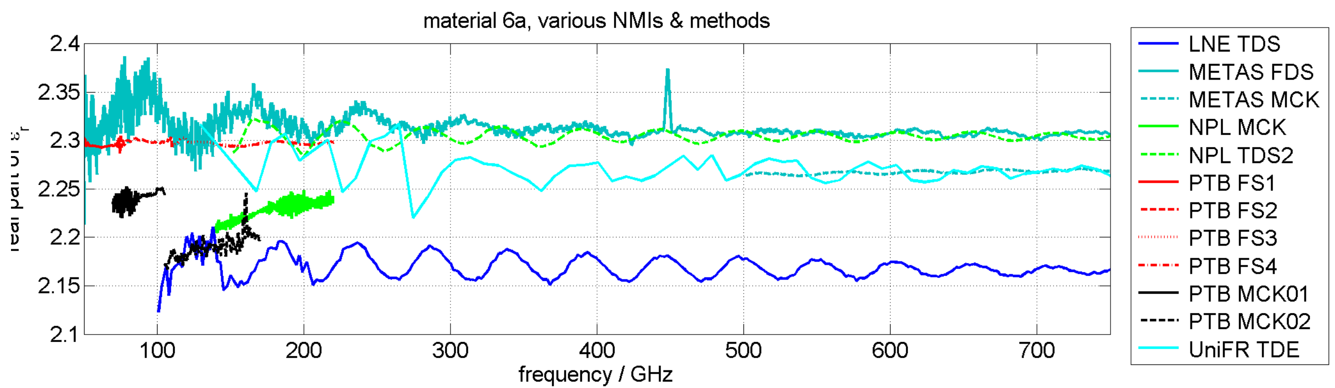

Figure 141: Material 6a (real part of ε_r) comparison of all methods 750G.

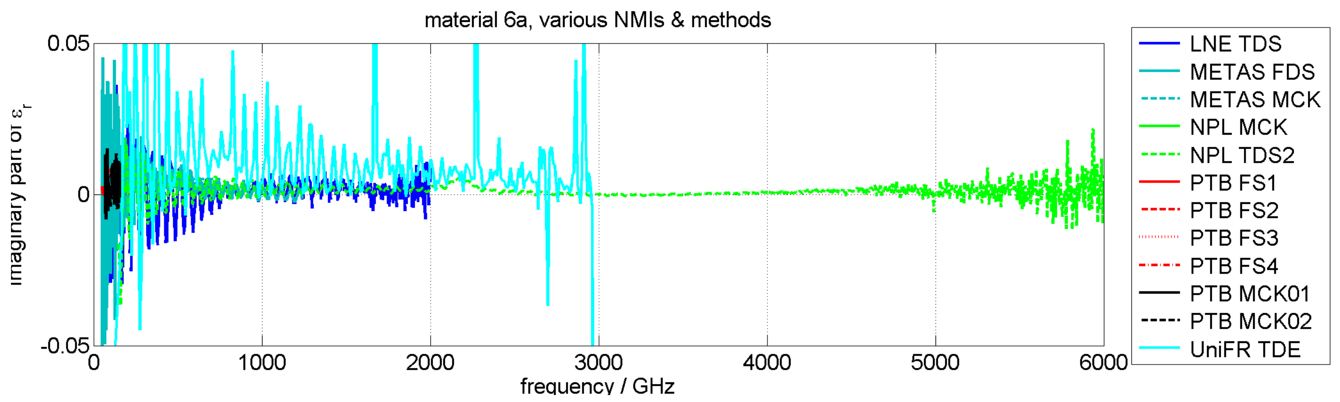

Figure 142: Material 6a (imaginary part of ε_r) comparison of all methods.

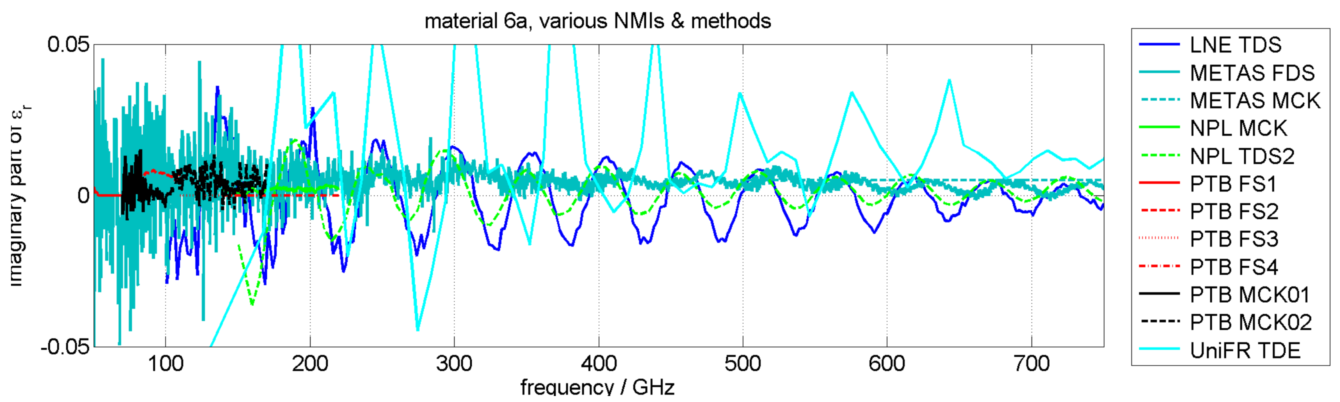

Figure 143: Material 6a (imaginary part of ε_r) comparison of all methods 750G.

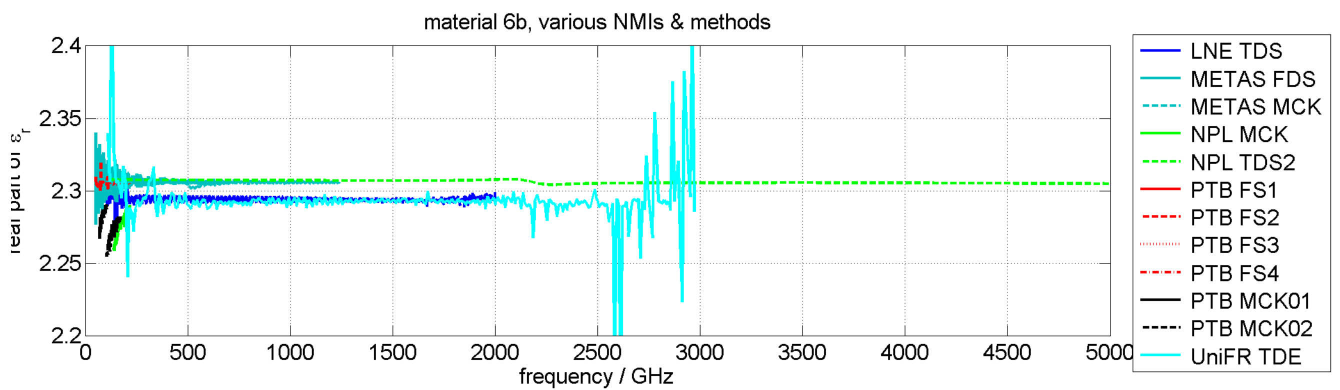

Figure 144: Material 6b (real part of ε_r) comparison of all methods.

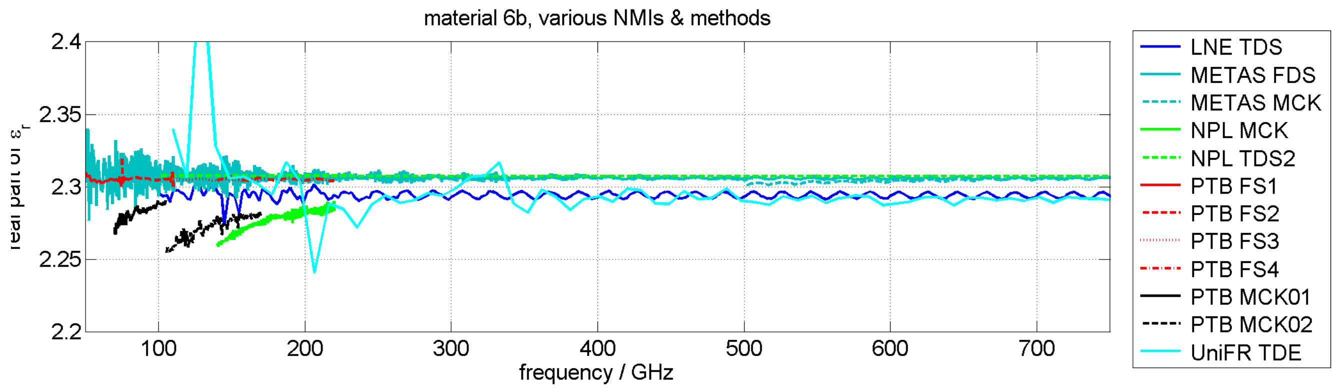

Figure 145: Material 6b (real part of ε_r) comparison of all methods 750G.

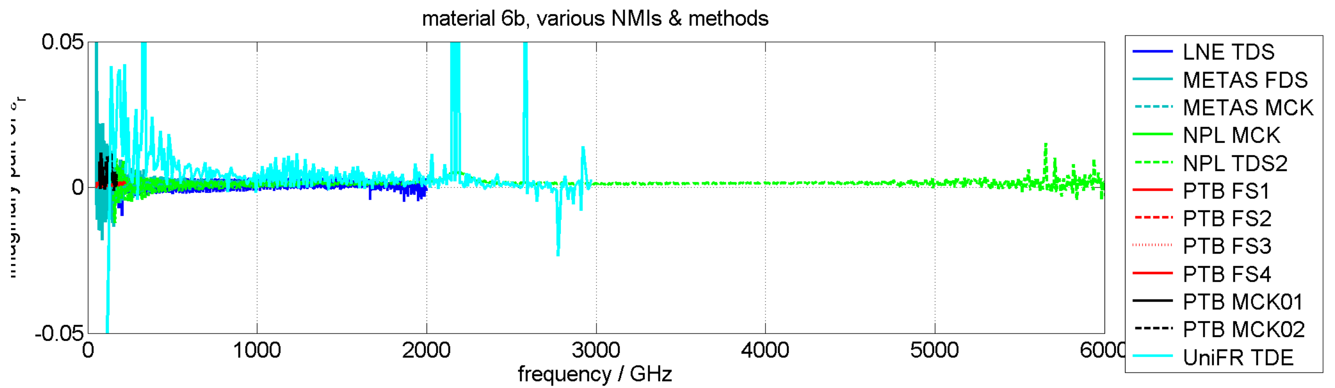

Figure 146: Material 6b (imaginary part of ε_r) comparison of all methods.

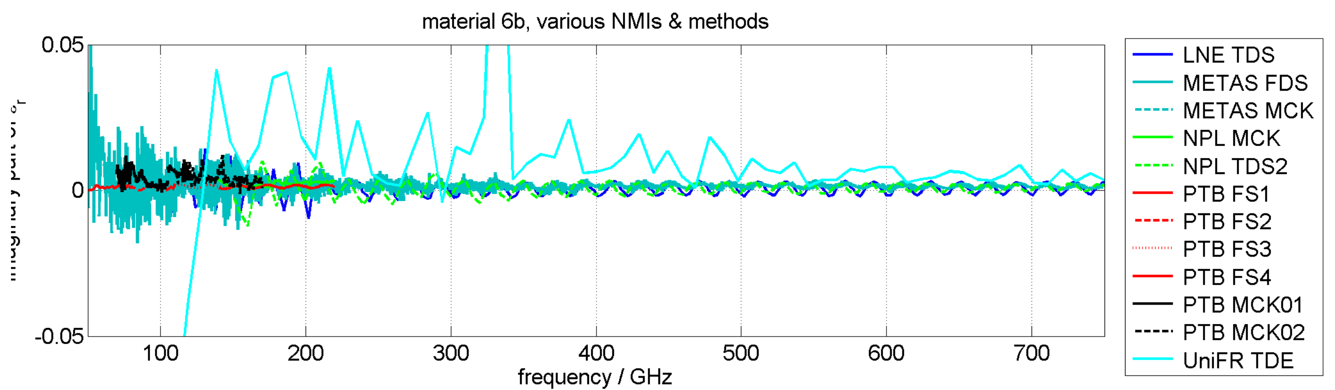

Figure 147: Material 6b (imaginary part of ε_r) comparison of all methods 750G.

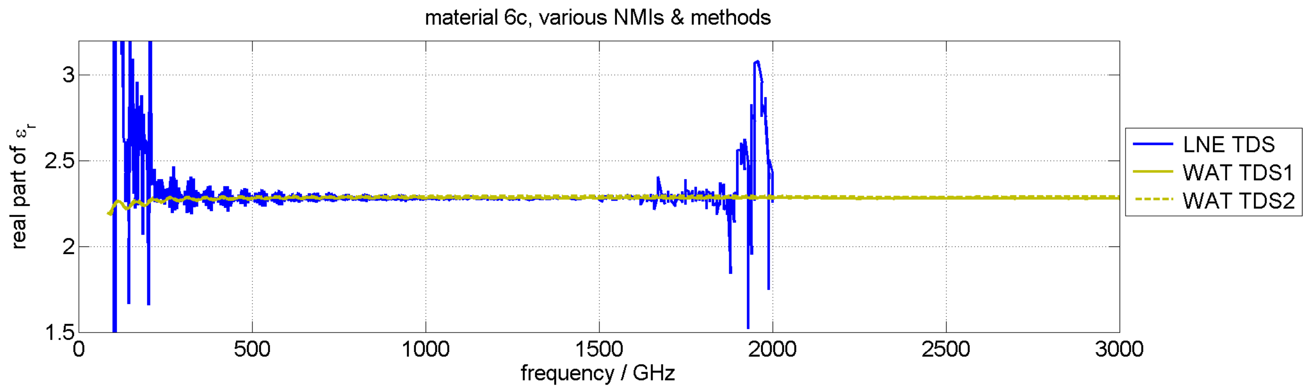

Figure 148: Material 6c (real part of ε_r) comparison of all methods.

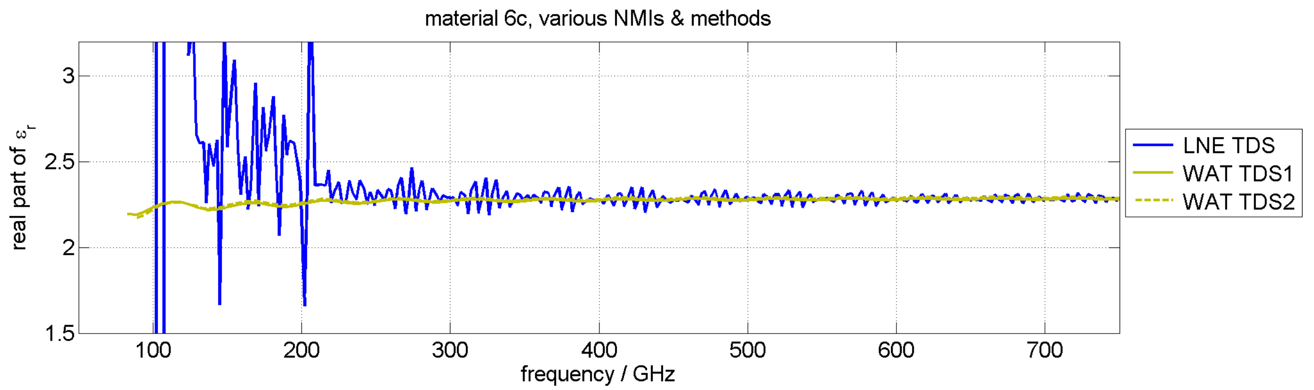

Figure 149: Material 6c (real part of ε_r) comparison of all methods 750G.

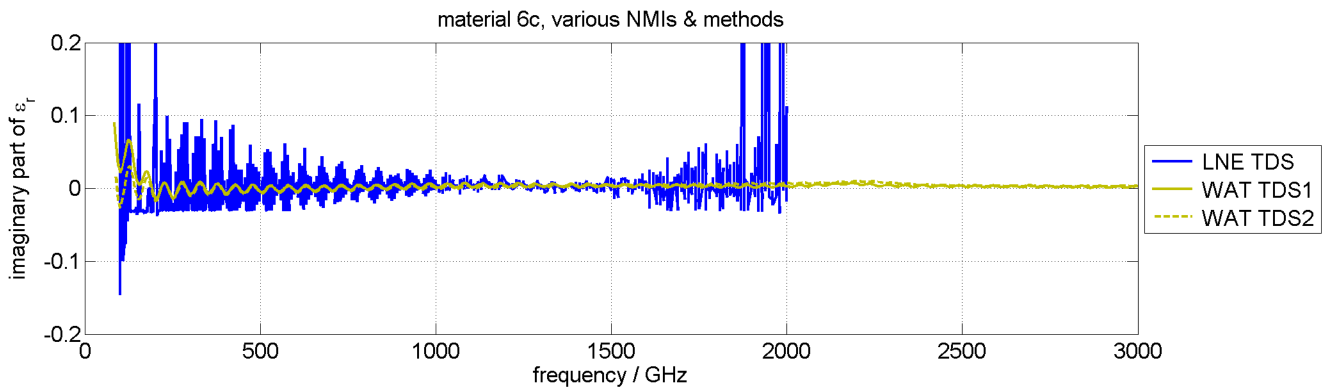

Figure 150: Material 6c (imaginary part of ε_r) comparison of all methods.

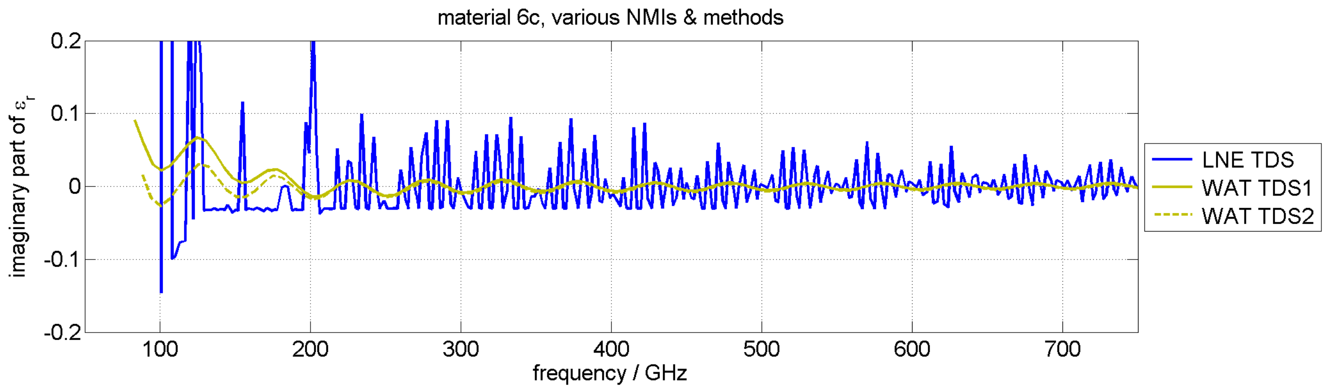

Figure 151: Material 6c (imaginary part of ε_r) comparison of all methods 750G.

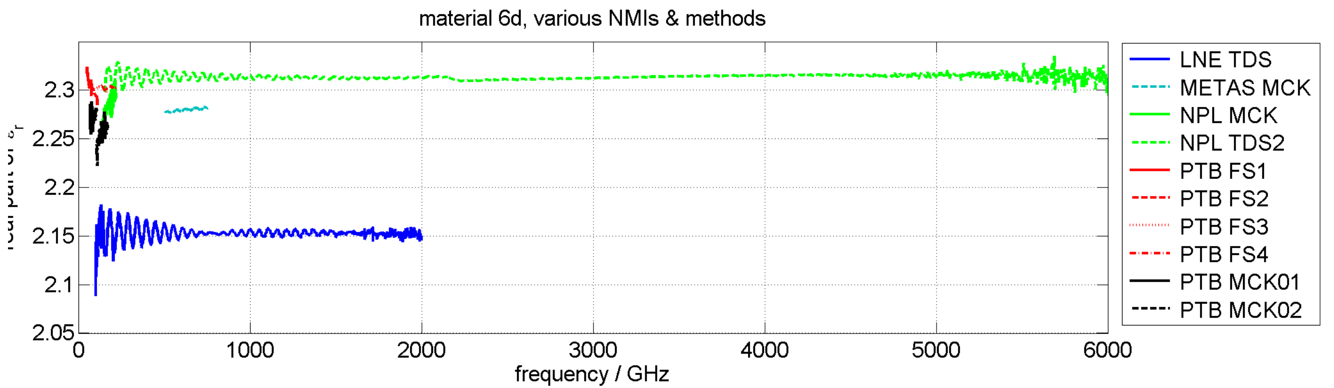

Figure 152: Material 6d (real part of ε_r) comparison of all methods.

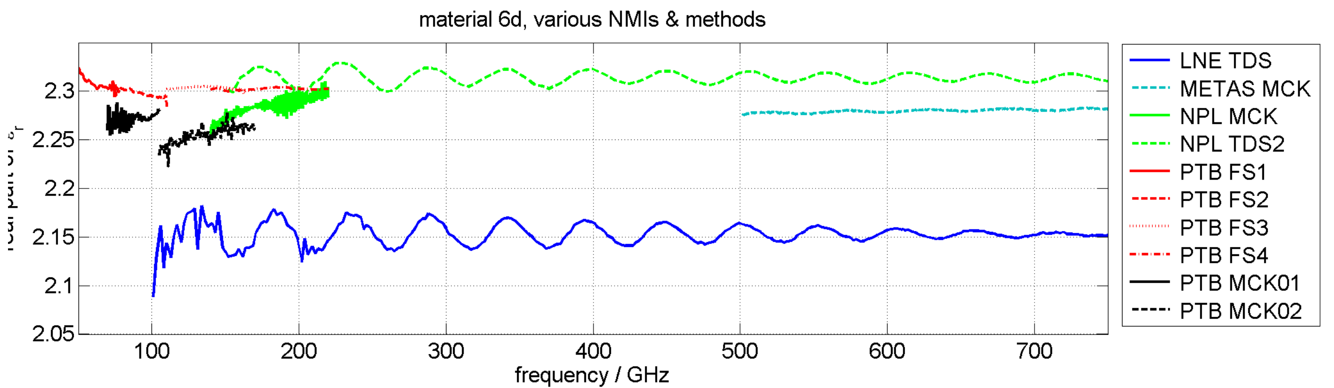

Figure 153: Material 6d (real part of ε_r) comparison of all methods 750G.

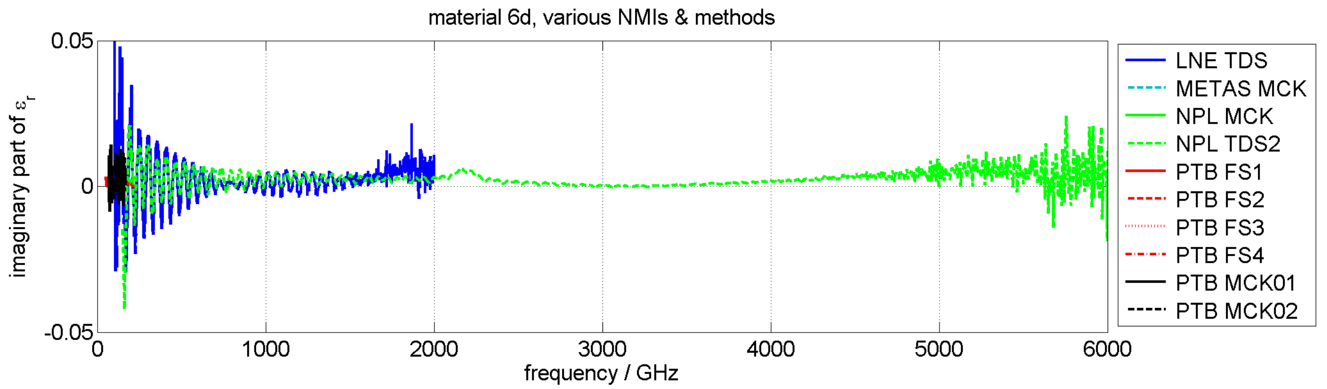

Figure 154: Material 6d (imaginary part of ε_r) comparison of all methods.

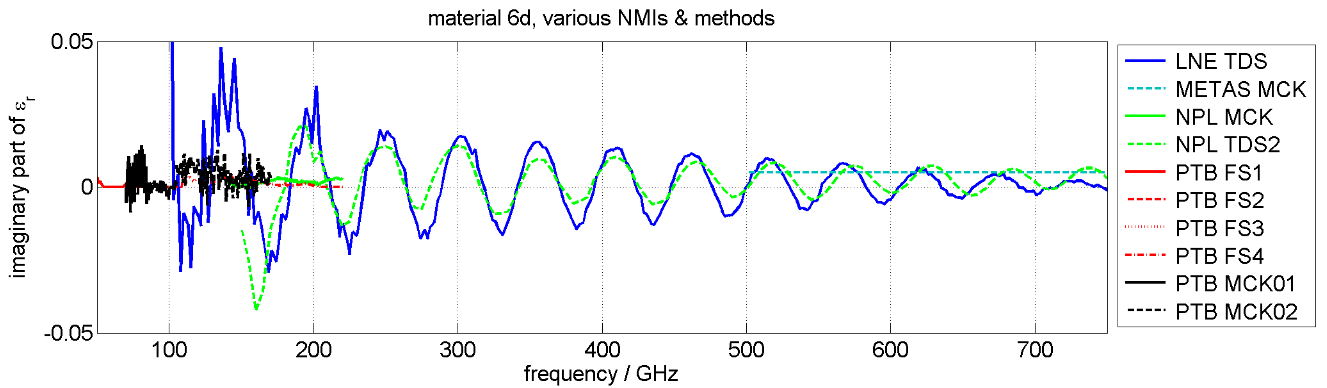

Figure 155: Material 6d (imaginary part of ε_r) comparison of all methods 750G.

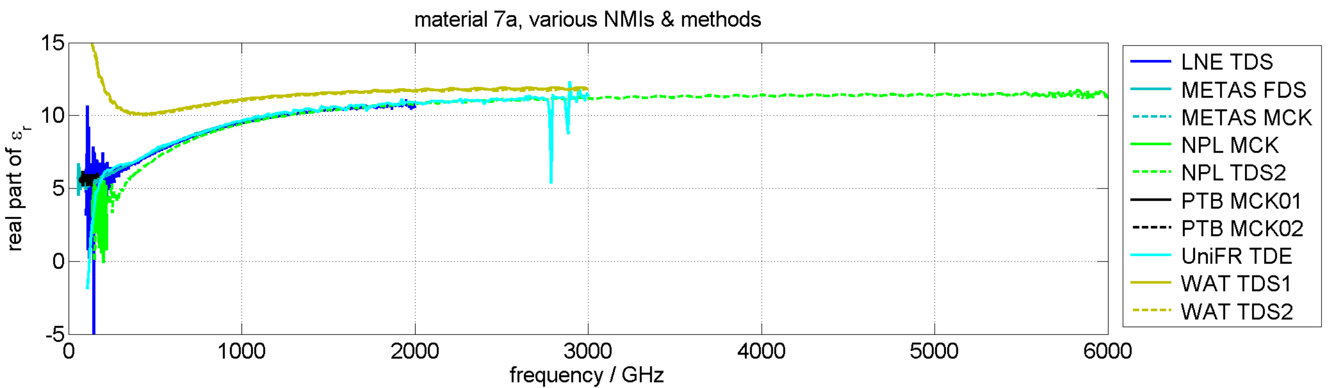

Figure 156: Material 7a (real part of ε_r) comparison of all methods.

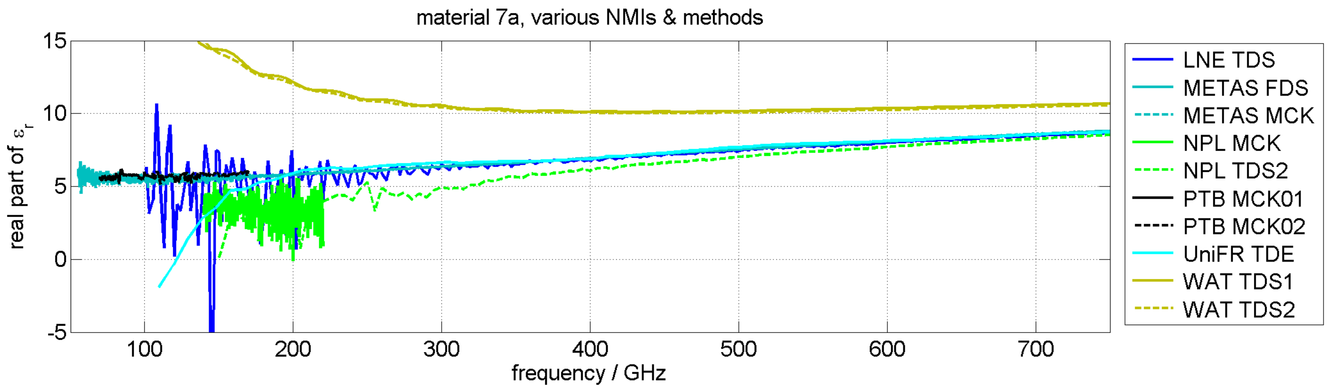

Figure 157: Material 7a (real part of ε_r) comparison of all methods 750G.

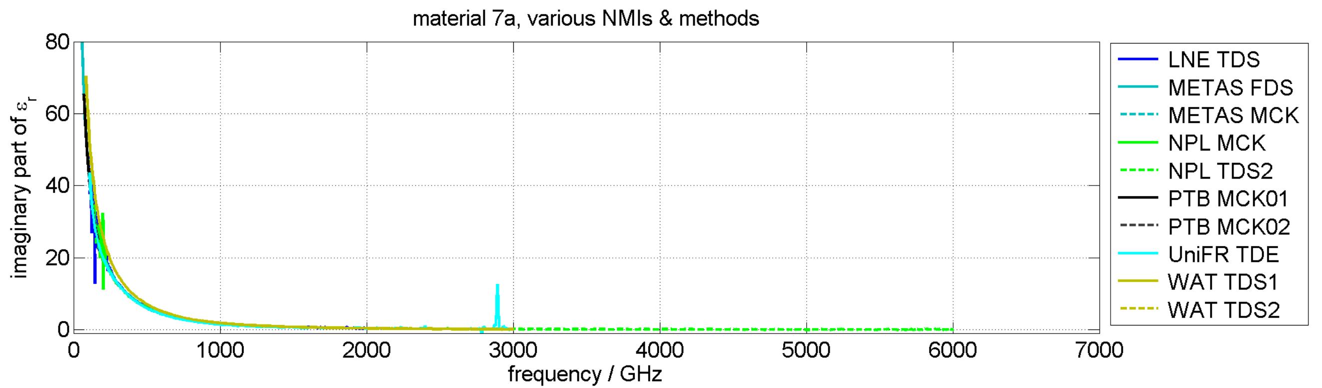

Figure 158: Material 7a (imaginary part of ε_r) comparison of all methods.

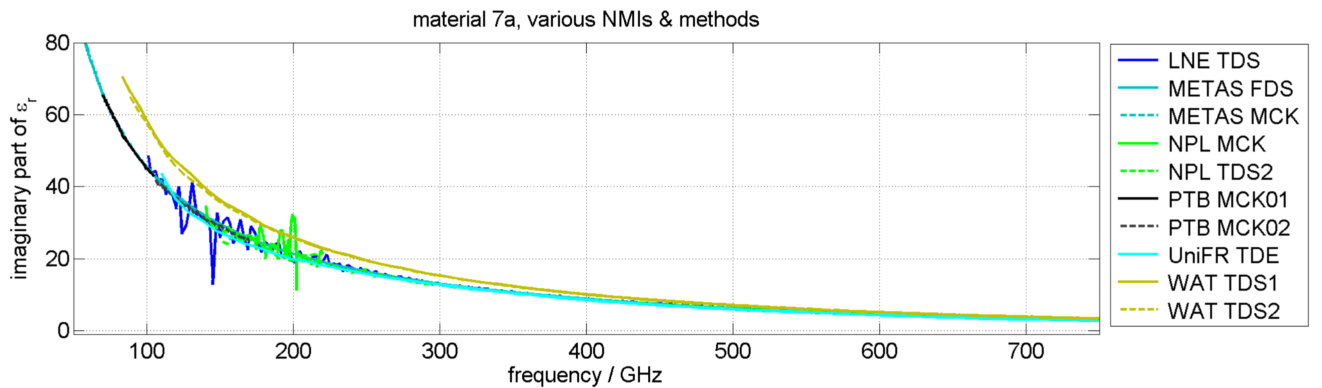

Figure 159: Material 7a (imaginary part of ε_r) comparison of all methods 750G.

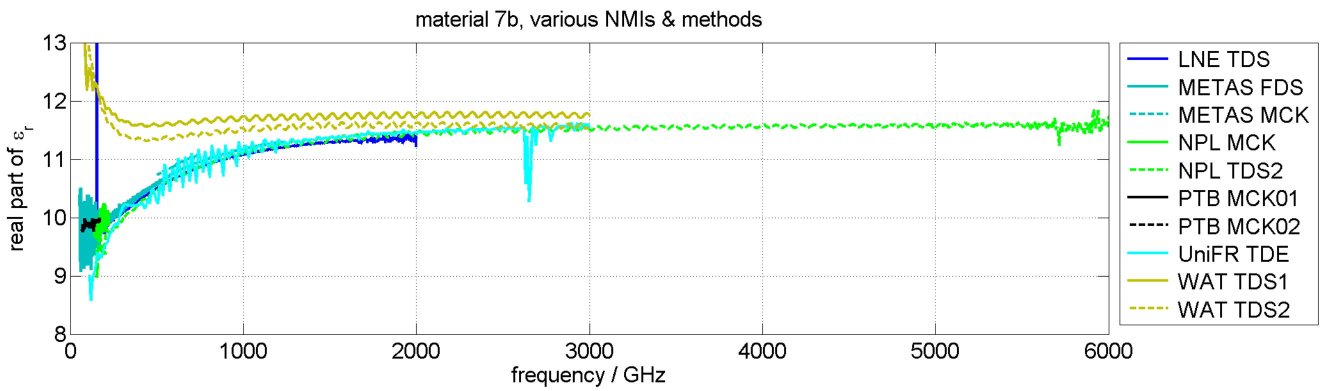

Figure 160: Material 7b (real part of ε_r) comparison of all methods.

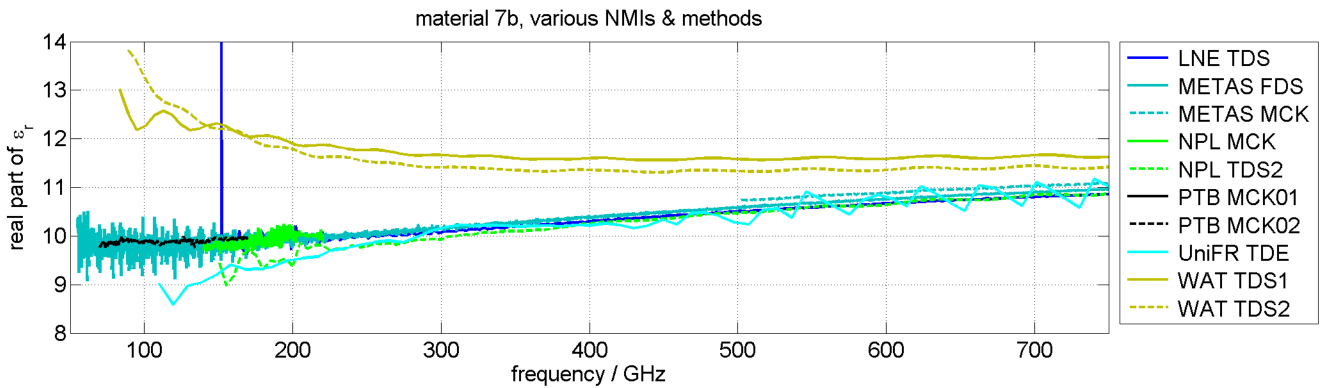

Figure 161: Material 7b (real part of ε_r) comparison of all methods 750G.

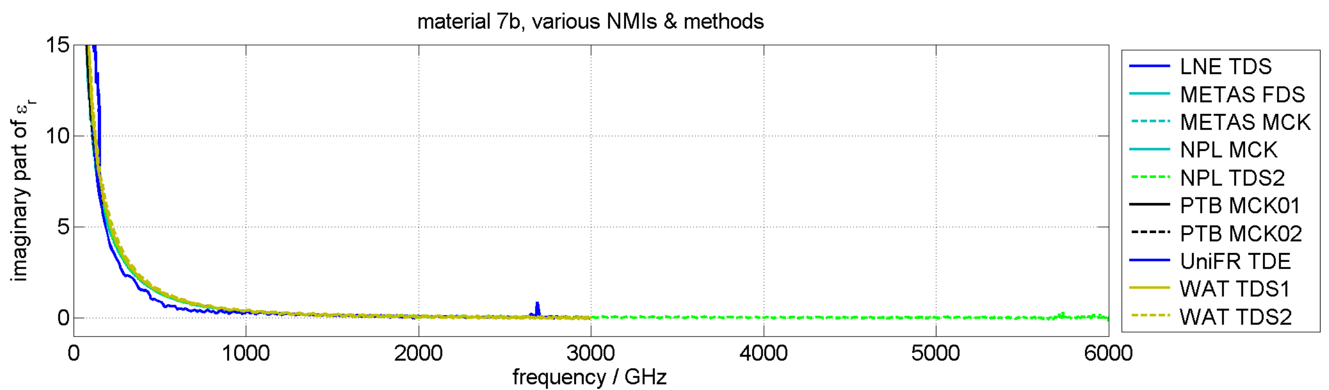

Figure 162: Material 7b (imaginary part of ε_r) comparison of all methods.

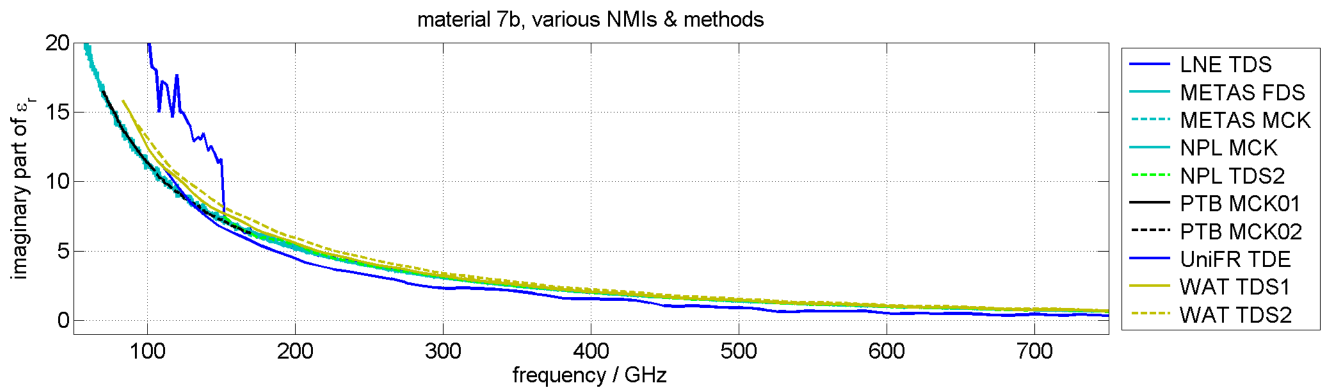

Figure 163: Material 7b (imaginary part of ε_r) comparison of all methods 750G.

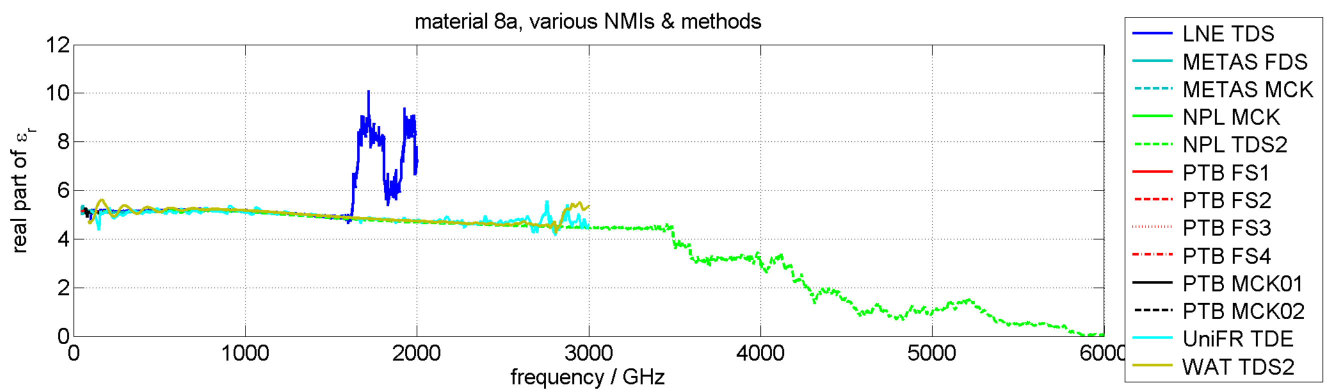

Figure 164: Material 8a (real part of ε_r) comparison of all methods.

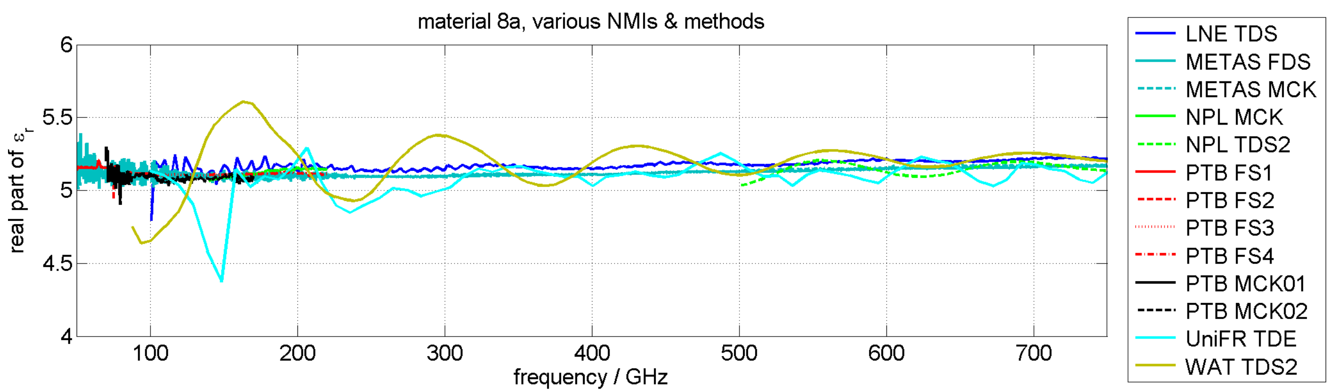

Figure 165: Material 8a (real part of ε_r) comparison of all methods 750G.

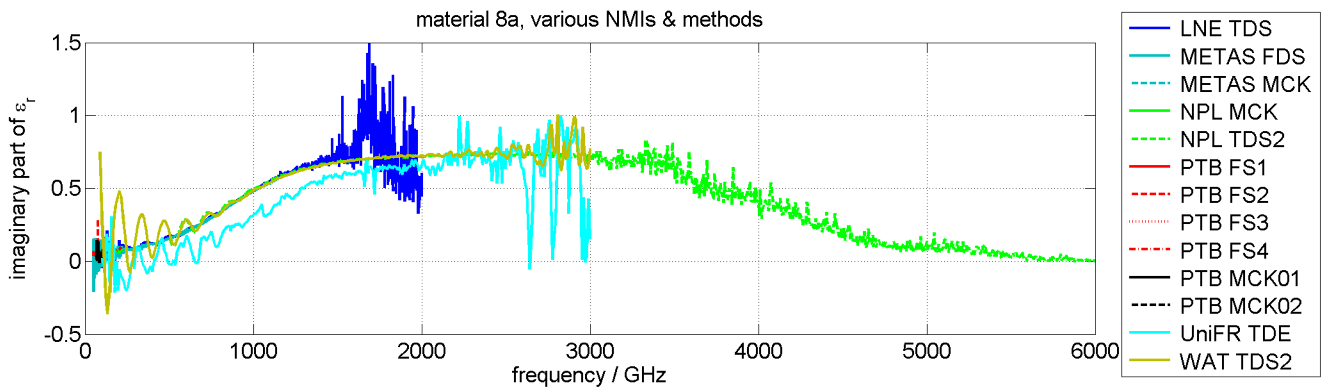

Figure 166: Material 8a (imaginary part of ε_r) comparison of all methods.

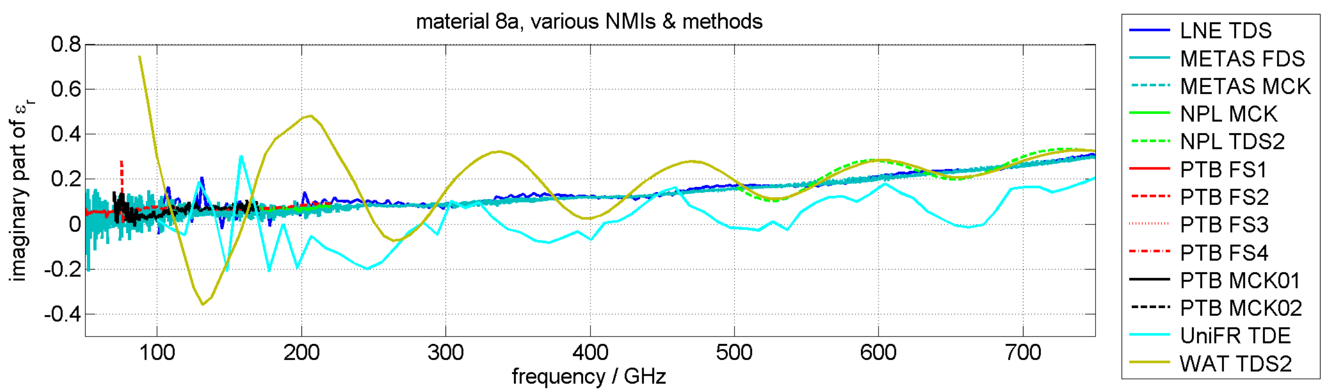

Figure 167: Material 8a (imaginary part of ε_r) comparison of all methods 750G.

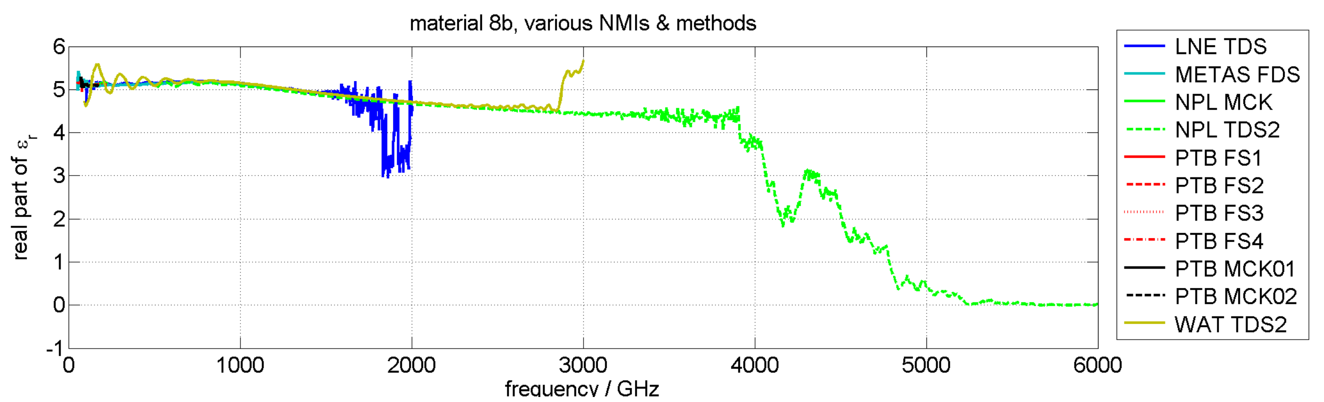

Figure 168: Material 8b (real part of ε_r) comparison of all methods.

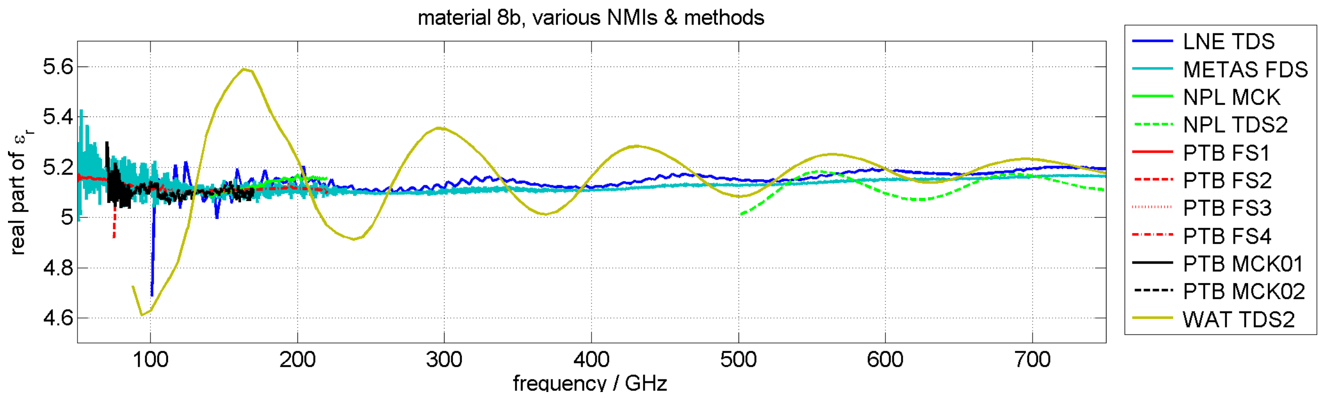

Figure 169: Material 8b (real part of ε_r) comparison of all methods 750G.

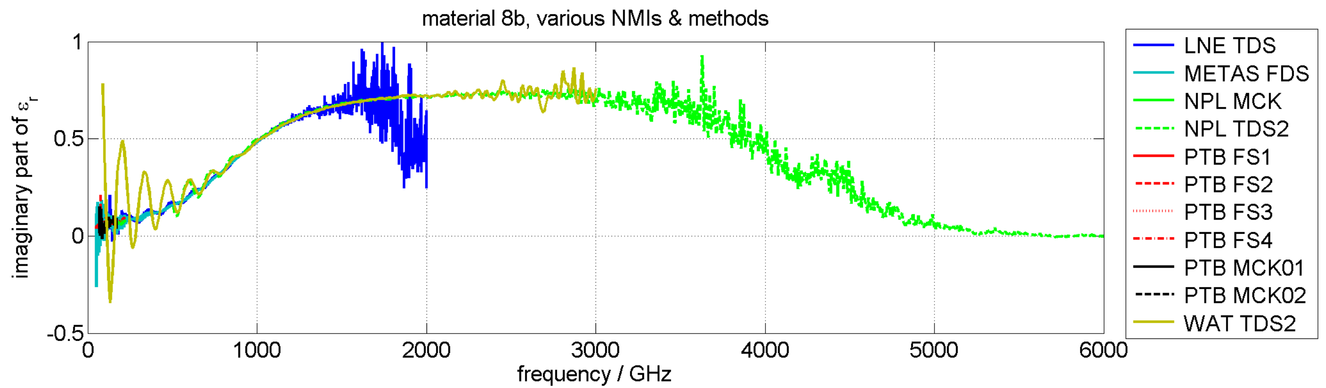

Figure 170: Material 8b (imaginary part of ε_r) comparison of all methods.

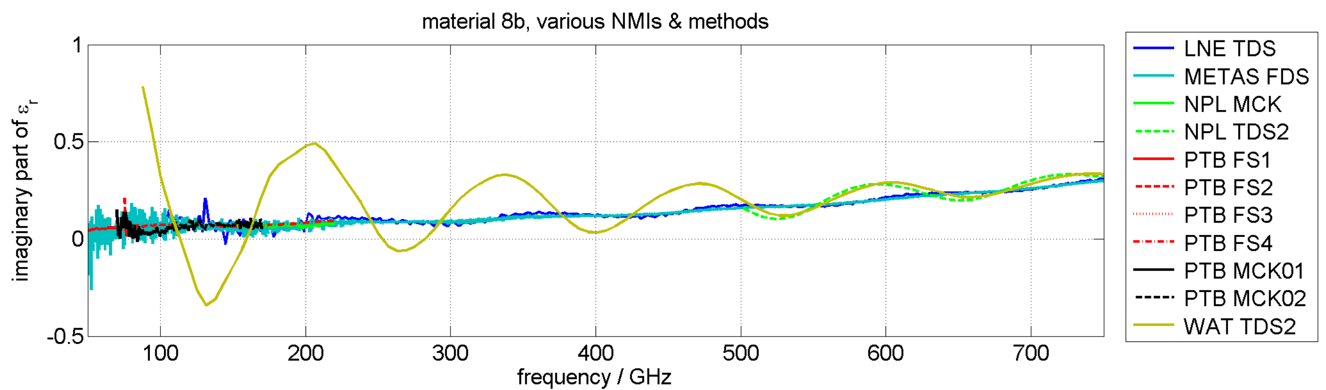

Figure 171: Material 8b (imaginary part of ε_r) comparison of all methods 750G.

6.2 Material Fused silica, all samples measured by one institute

This section shows a comparison of all Fused silica samples (material #2Axx, see Table 3) with different thicknesses. The differences between the extracted permittivity of several samples of the same material are most likely due to inaccuracies of the sample thickness values.

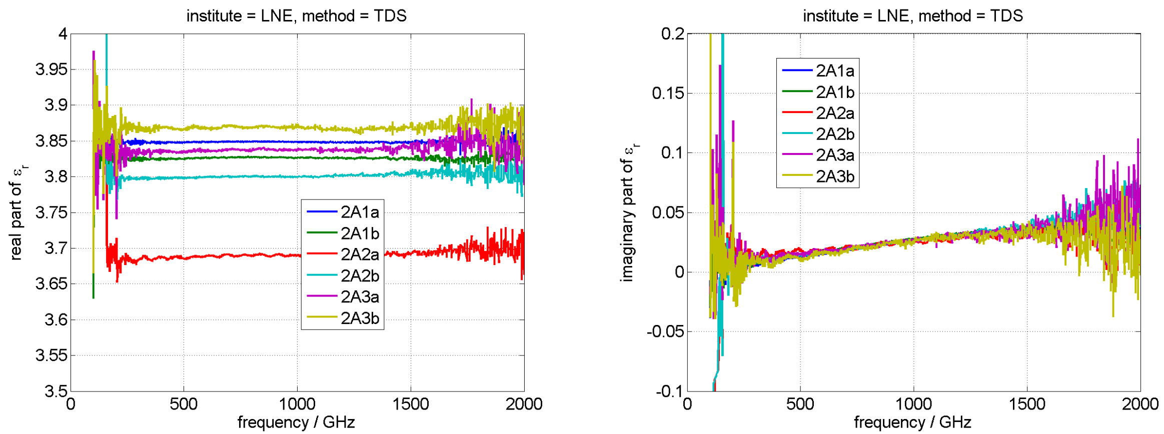

Figure 172: Material 2Axx (Fused silica), all samples measured by one institute.

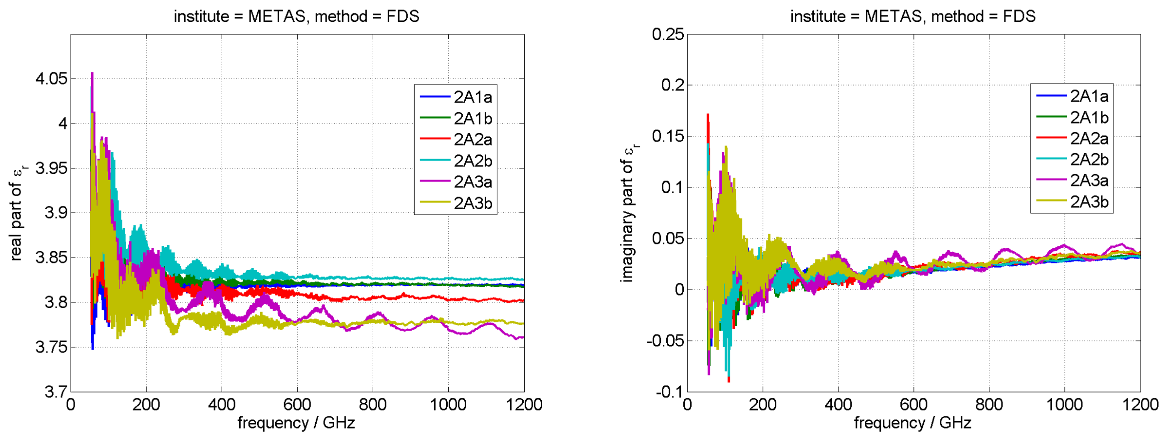

Figure 173: Material 2Axx (Fused silica), all samples measured by one institute.

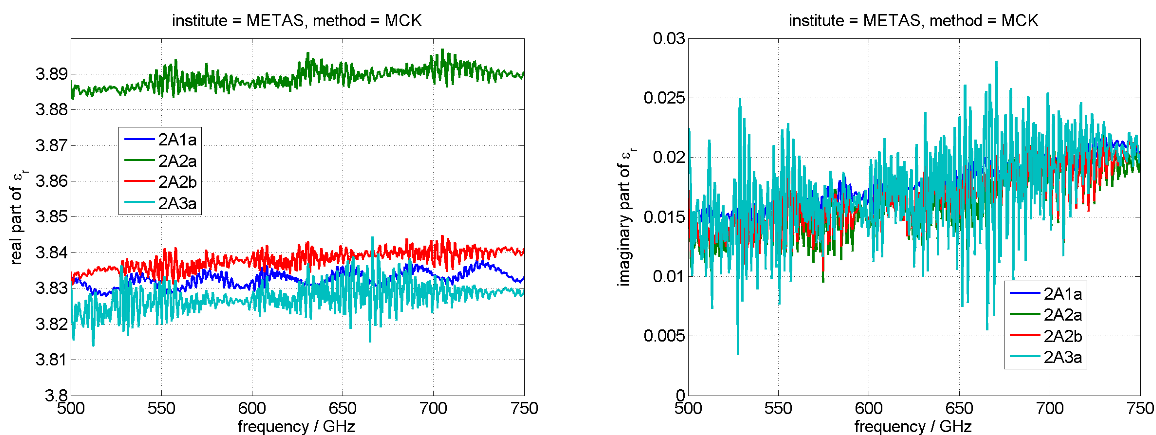

Figure 174: Material 2Axx (Fused silica), all samples measured by one institute.

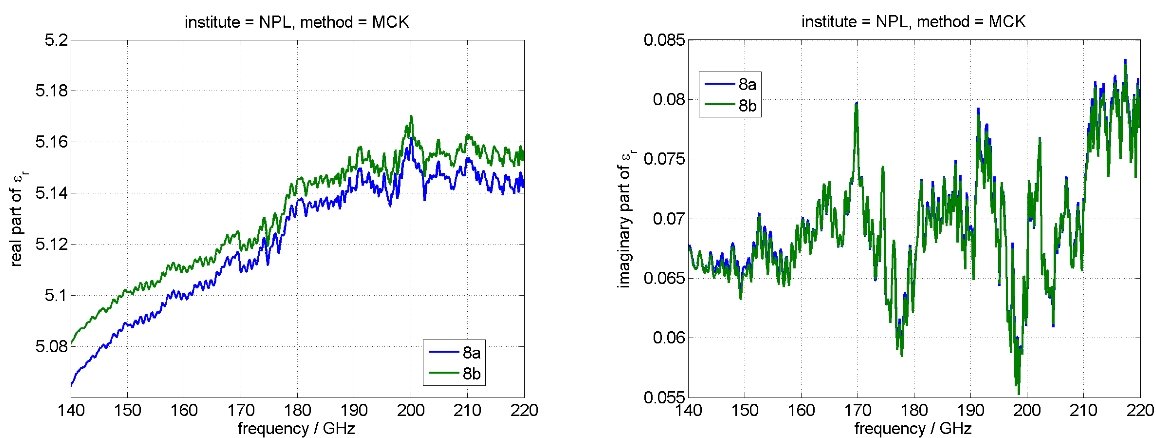

Figure 175: Material 2Axx (Fused silica), all samples measured by one institute.

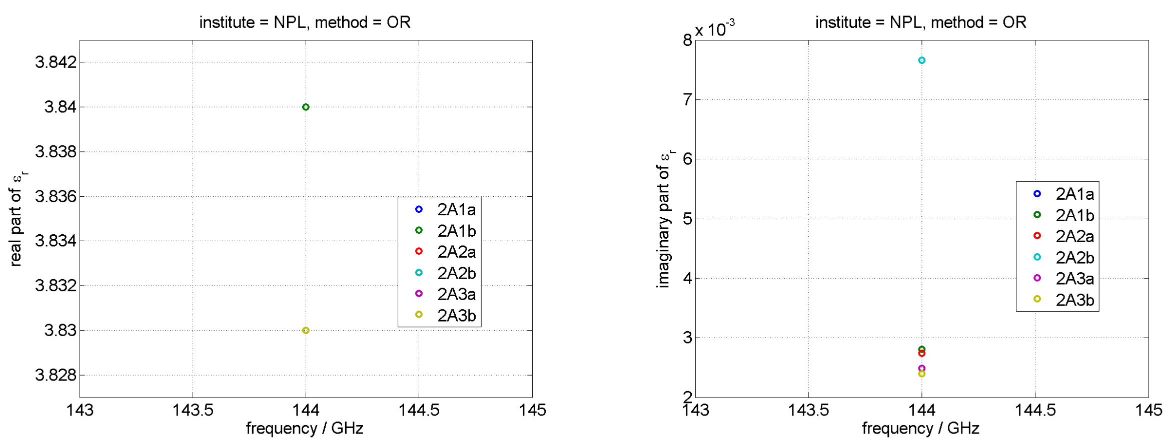

Figure 176: Material 2Axx (Fused silica), all samples measured by one institute.

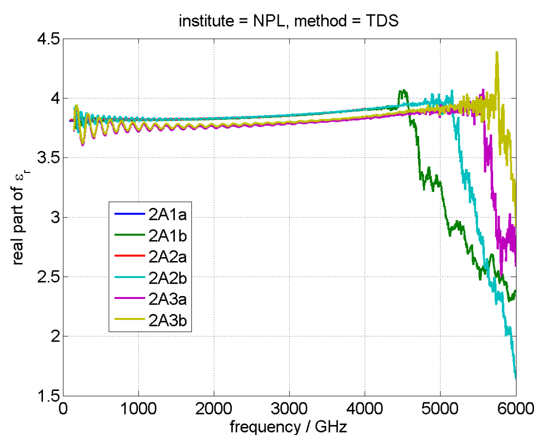

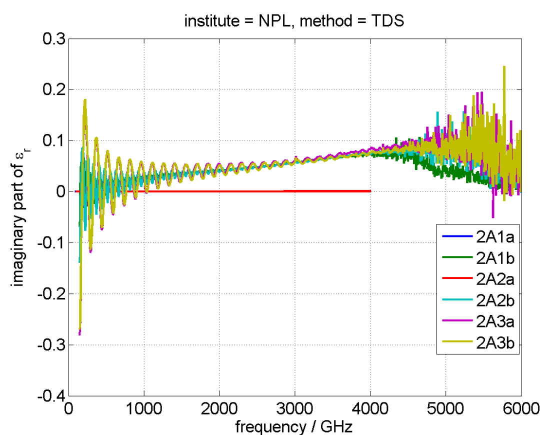

Figure 177: Material 2Axx (Fused silica), all samples measured by one institute.

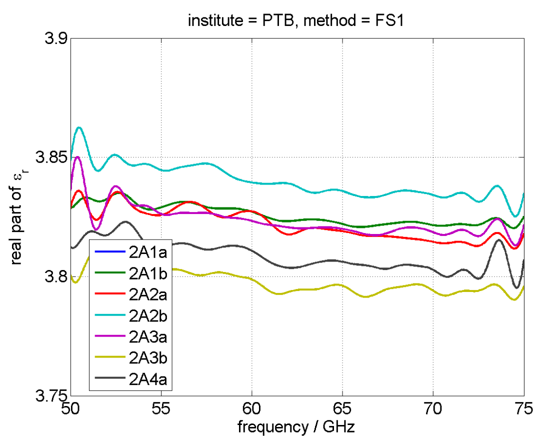

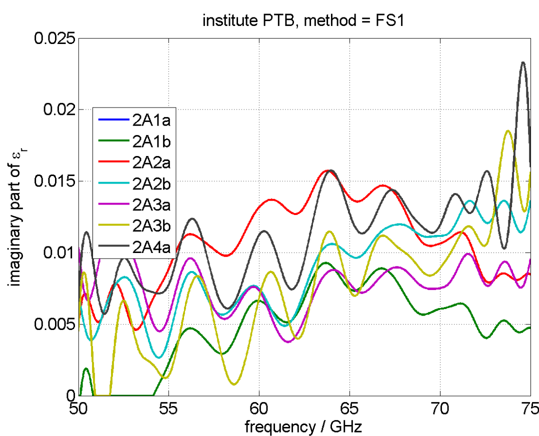

Figure 178: Material 2Axx (Fused silica), all samples measured by one institute.

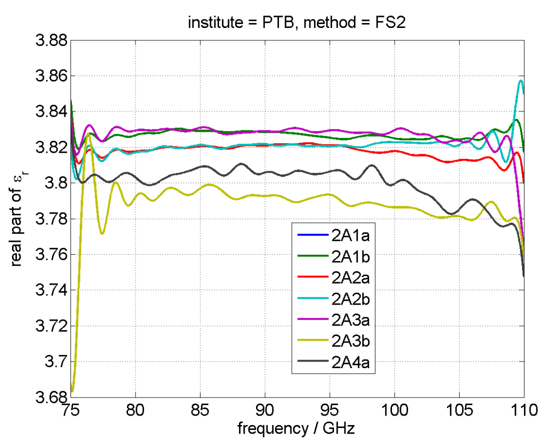

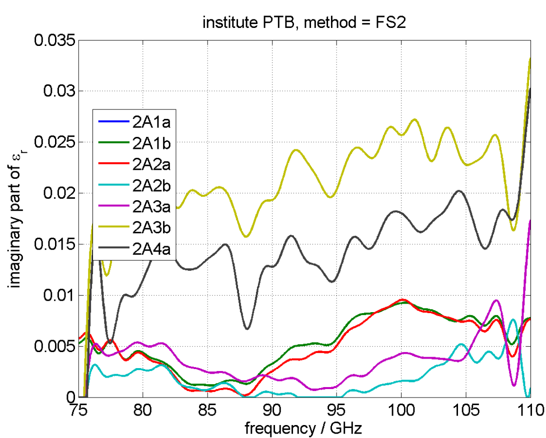

Figure 179: Material 2Axx (Fused silica), all samples measured by one institute.

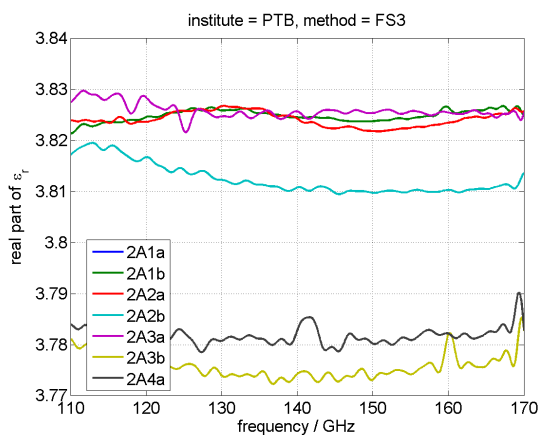

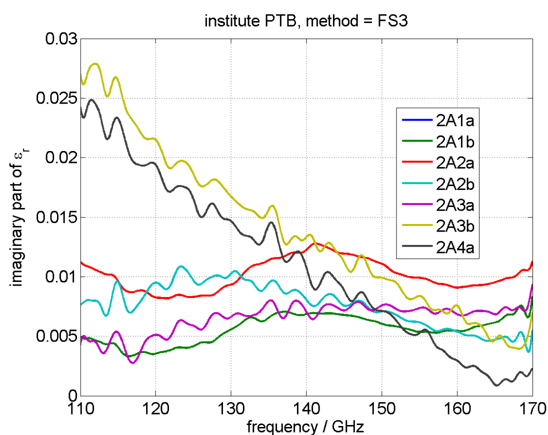

Figure 180: Material 2Axx (Fused silica), all samples measured by one institute.

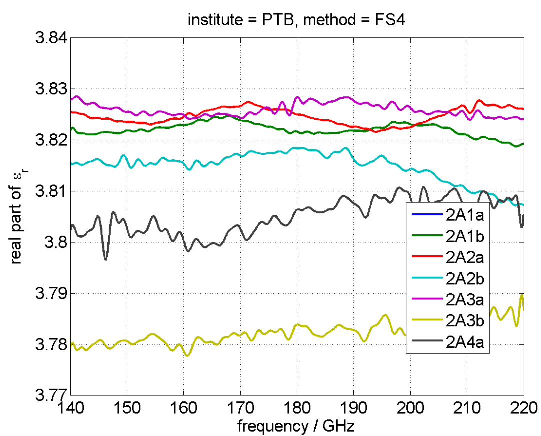

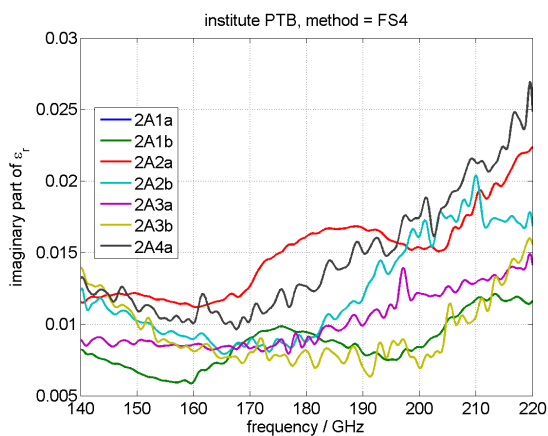

Figure 181: Material 2Axx (Fused silica), all samples measured by one institute.

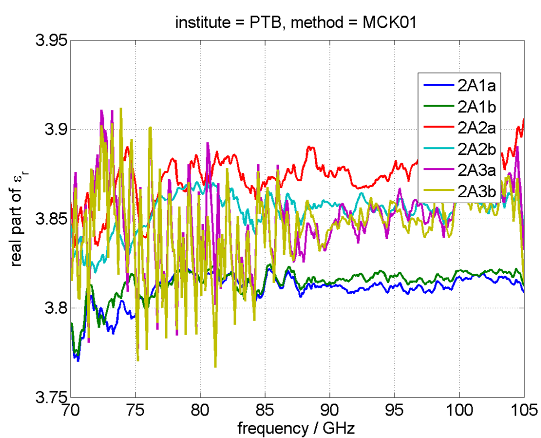

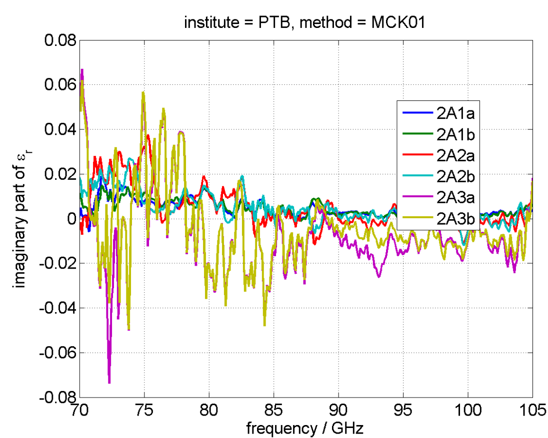

Figure 182: Material 2Axx (Fused silica), all samples measured by one institute.

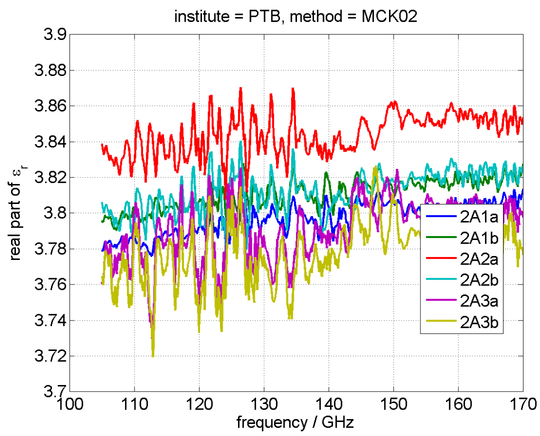

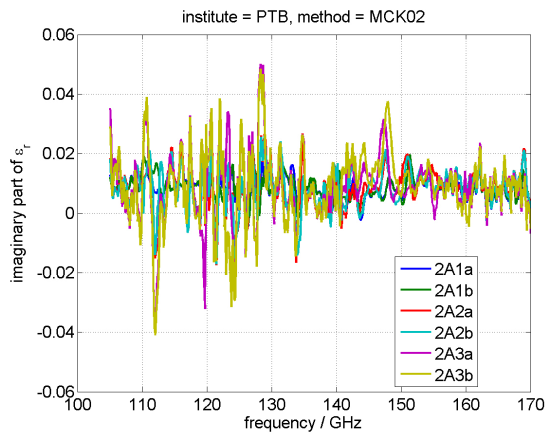

Figure 183: Material 2Axx (Fused silica), all samples measured by one institute.

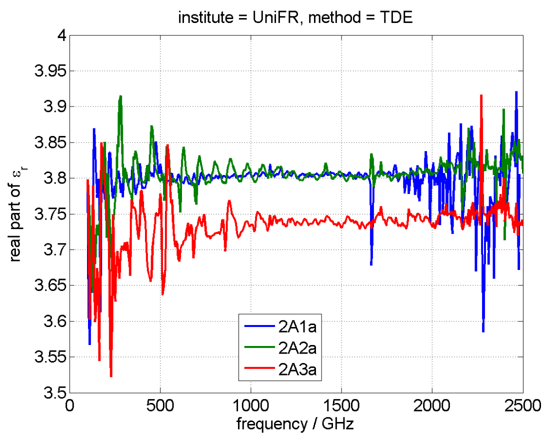

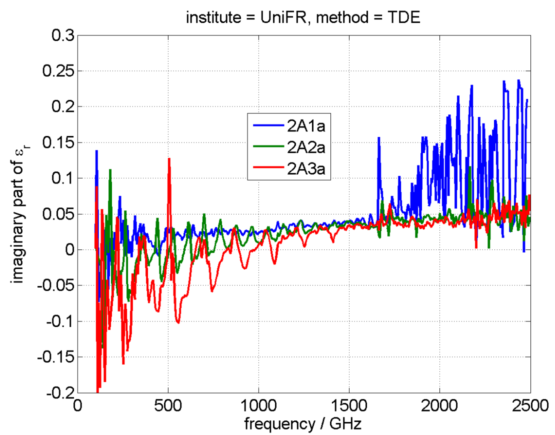

Figure 184: Material 2Axx (Fused silica), all samples measured by one institute.

6.3 Material UHMW polyethylene, all samples measured by one institute

This section shows a comparison of all UHMW polyethylene samples (material #6x, see Table 3) with different thicknesses.

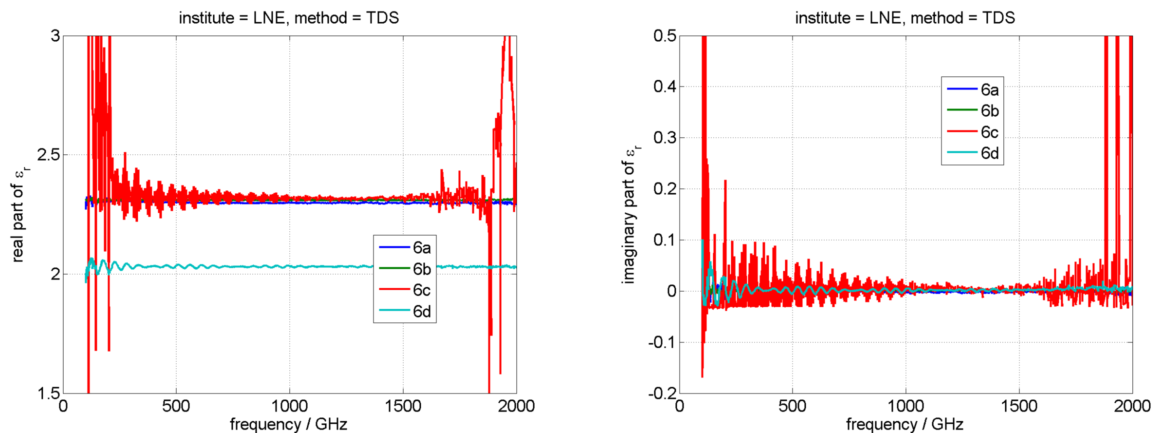

Figure 185: Material 6x (UHMW polyethylene), all samples measured by one institute.

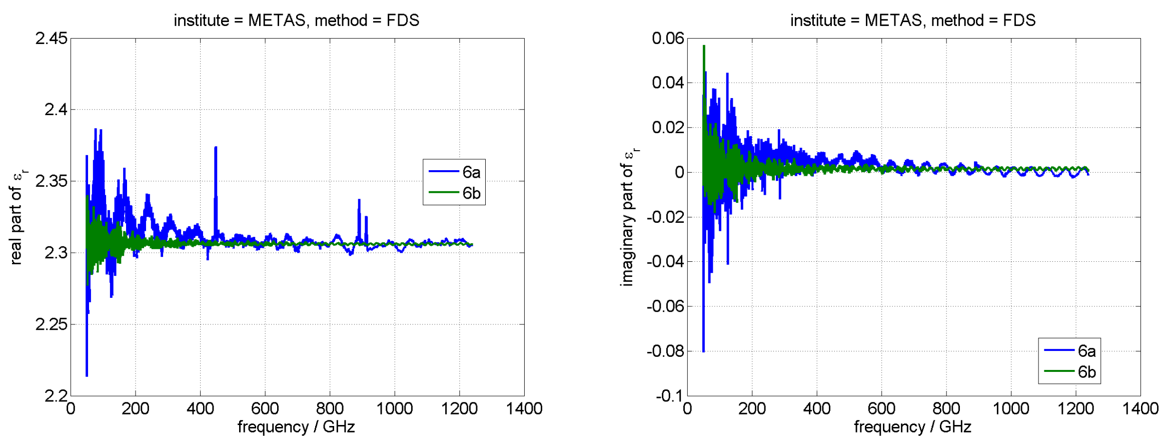

Figure 186: Material 6x (UHMW polyethylene), all samples measured by one institute.

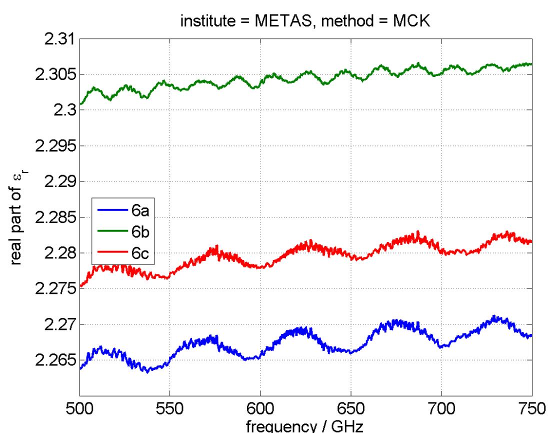

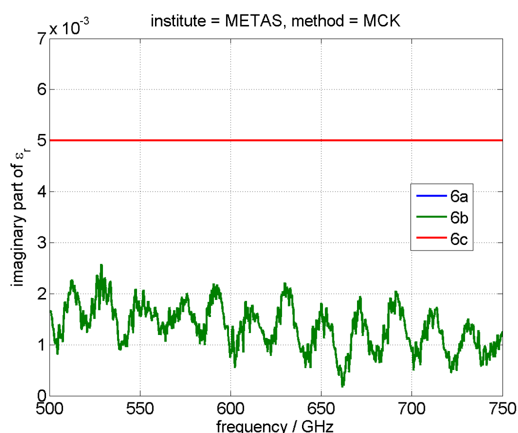

Figure 187: Material 6x (UHMW polyethylene), all samples measured by one institute.

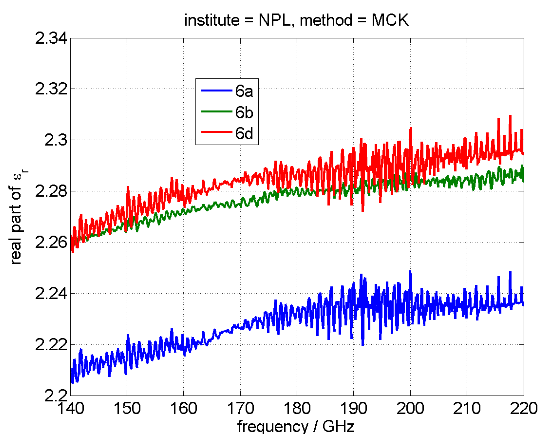

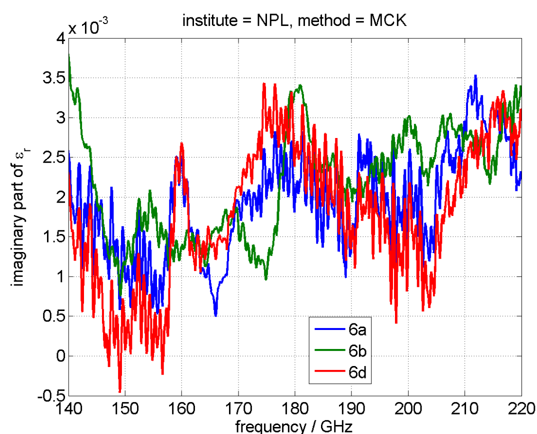

Figure 188: Material 6x (UHMW polyethylene), all samples measured by one institute.

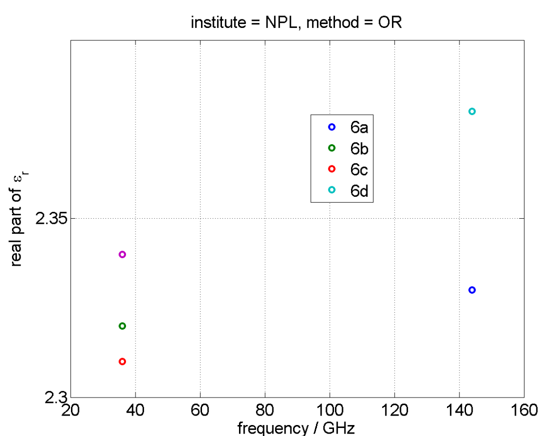

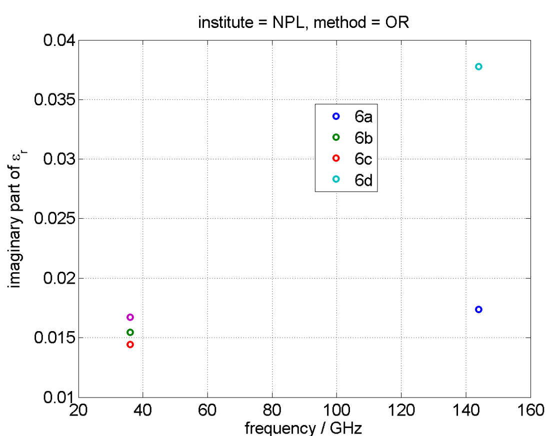

Figure 189: Material 6x (UHMW polyethylene), all samples measured by one institute.

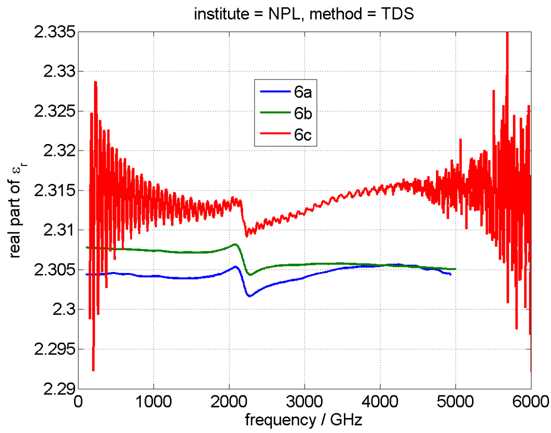

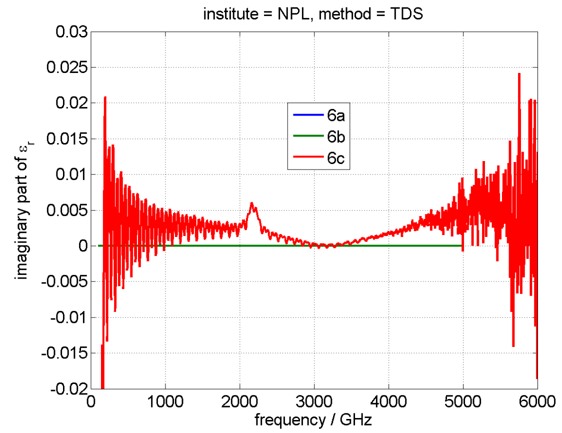

Figure 190: Material 6x (UHMW polyethylene), all samples measured by one institute.

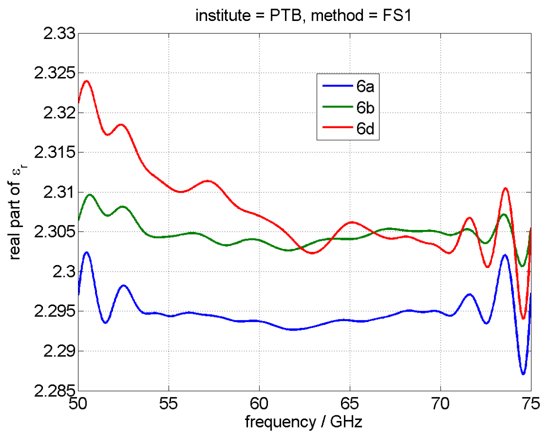

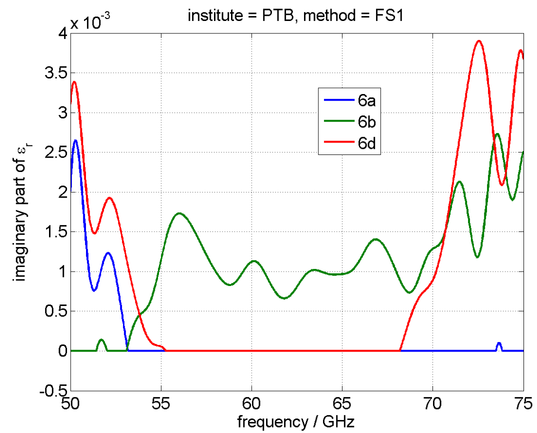

Figure 191: Material 6x (UHMW polyethylene), all samples measured by one institute.

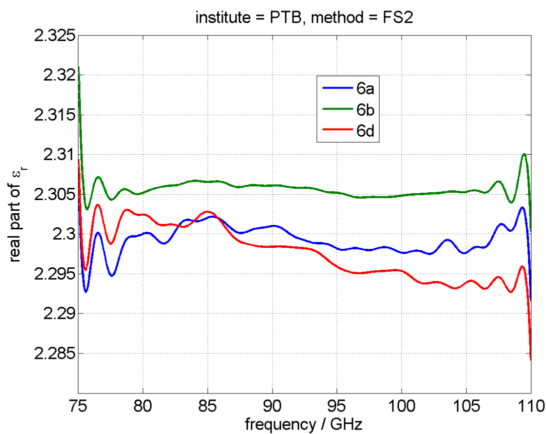

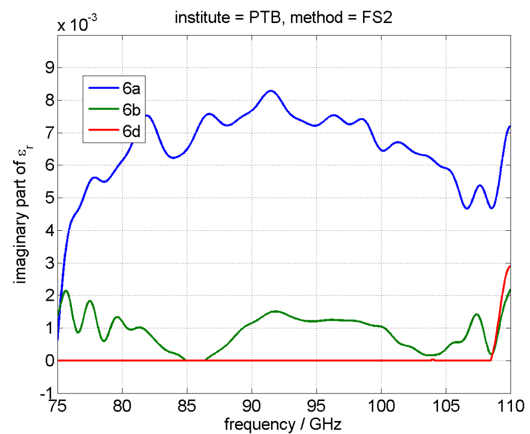

Figure 192: Material 6x (UHMW polyethylene), all samples measured by one institute.

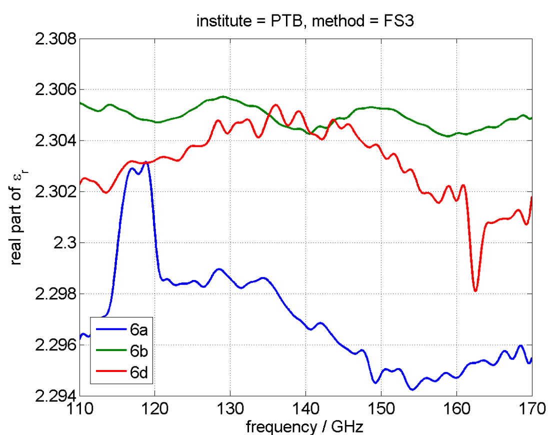

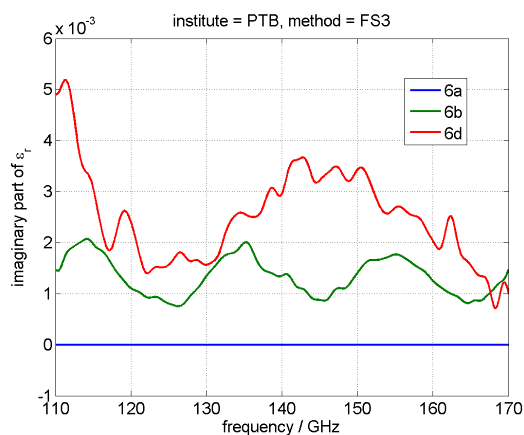

Figure 193: Material 6x (UHMW polyethylene), all samples measured by one institute.

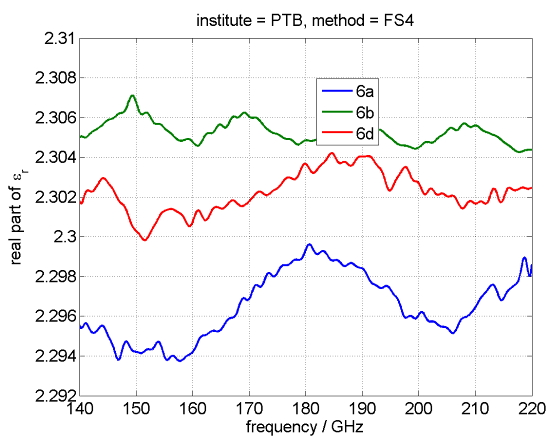

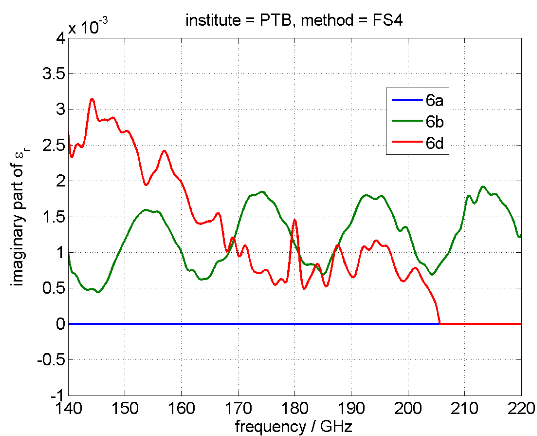

Figure 194: Material 6x (UHMW polyethylene), all samples measured by one institute.

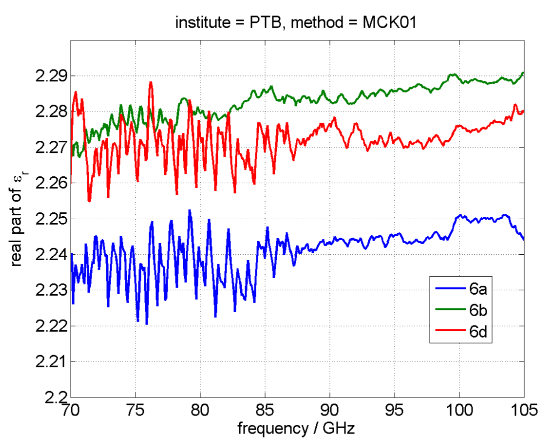

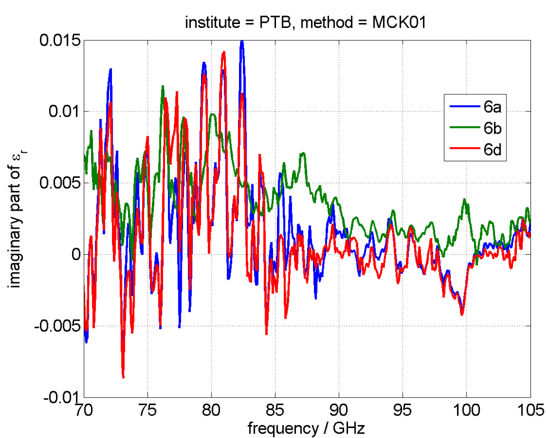

Figure 195: Material 6x (UHMW polyethylene), all samples measured by one institute.

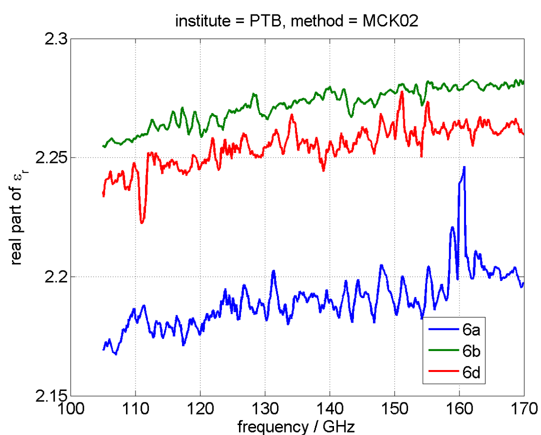

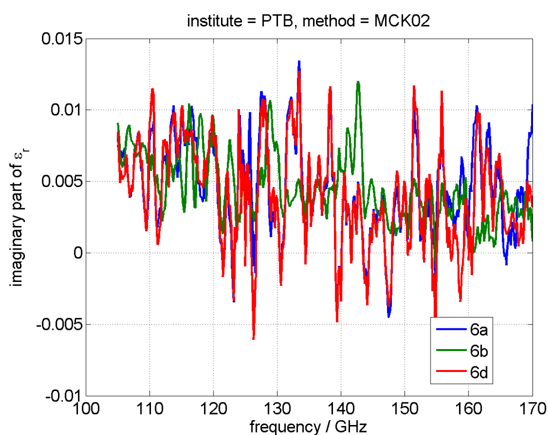

Figure 196: Material 6x (UHMW polyethylene), all samples measured by one institute.

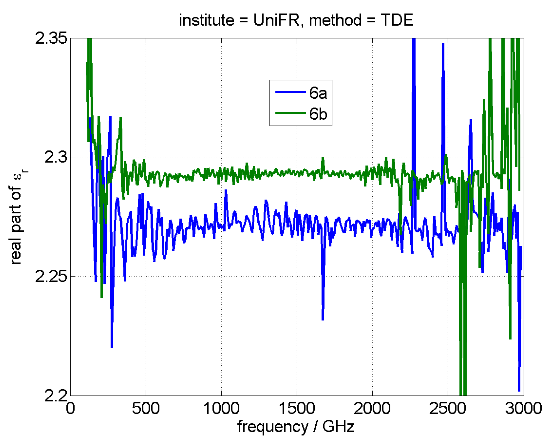

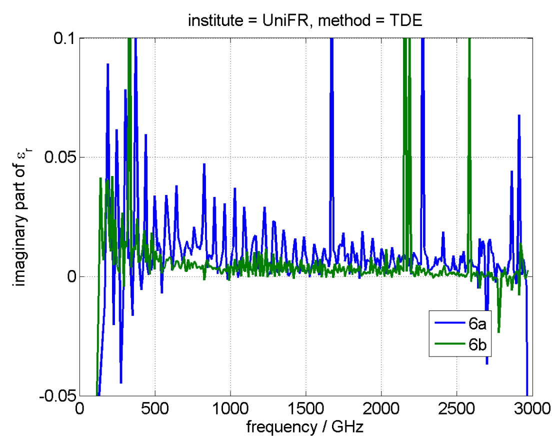

Figure 197: Material 6x (UHMW polyethylene), all samples measured by one institute.

6.4 Material doped silicon, both samples measured by one institute

This section shows a comparison of all doped silicon samples (material #7x, see Table 3) with different thicknesses. Please note that two different samples with different dopings were used, which were not cut from the same piece of bulk material.

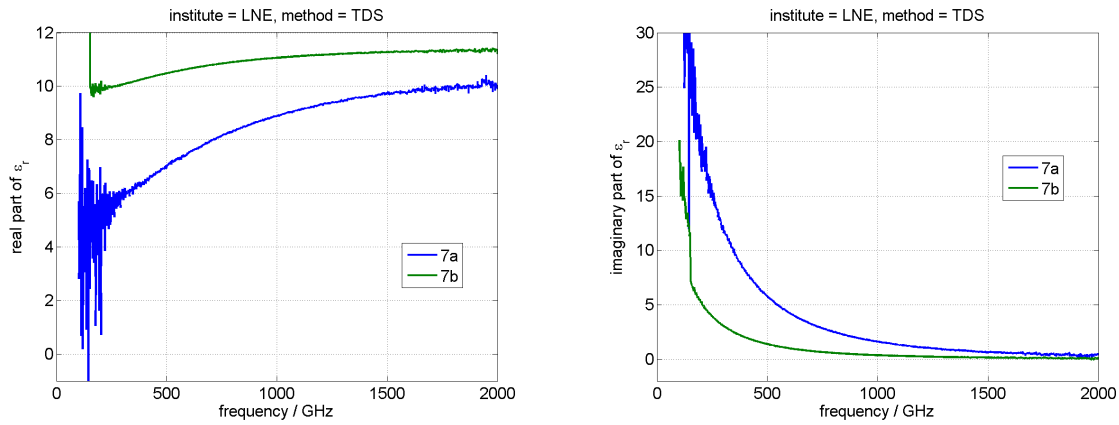

Figure 198: Material 7x (doped silicon), both samples measured by one institute.

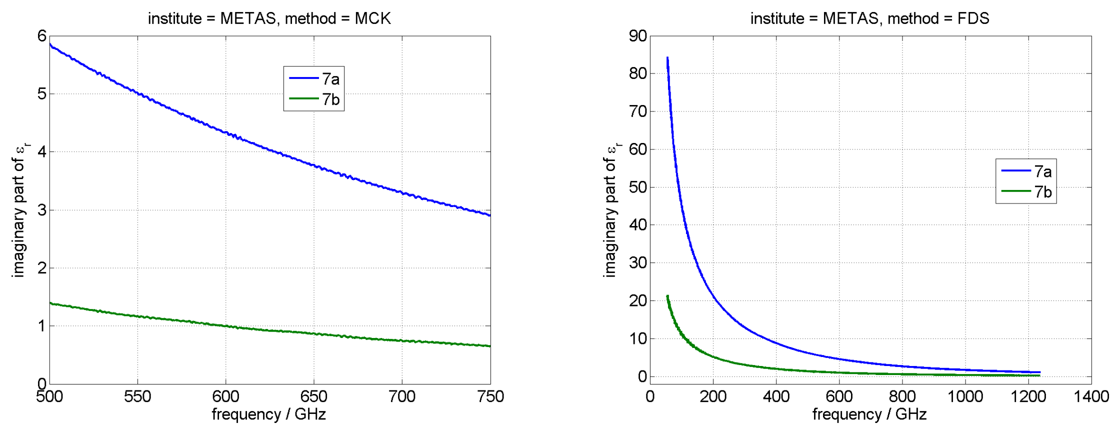

Figure 199: Material 7x (doped silicon), both samples measured by one institute.

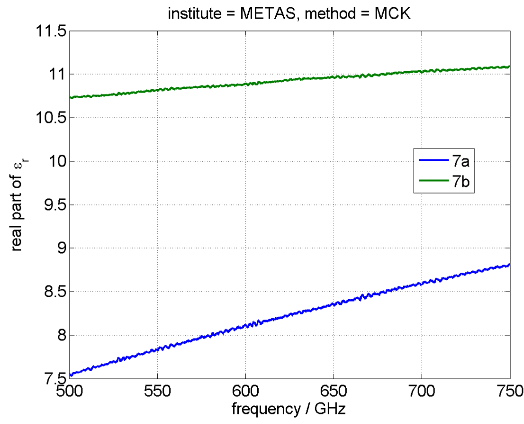

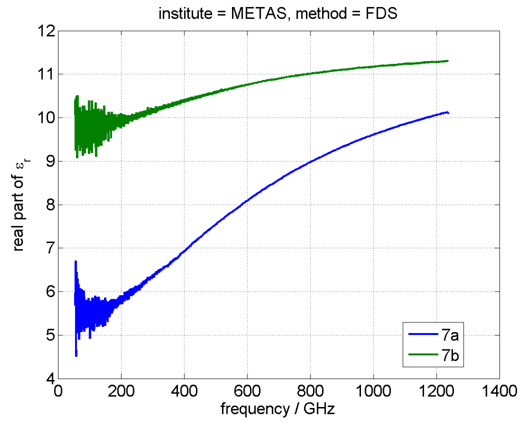

Figure 200: Material 7x (doped silicon), both samples measured by one institute.

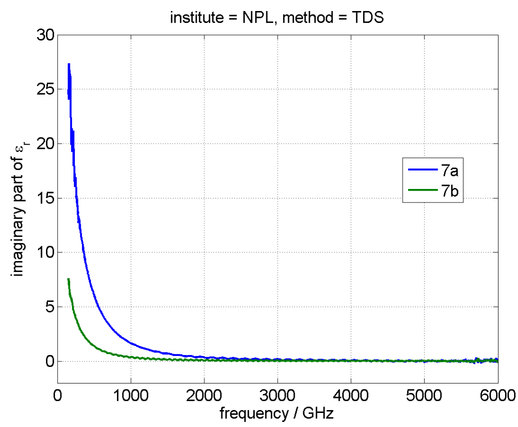

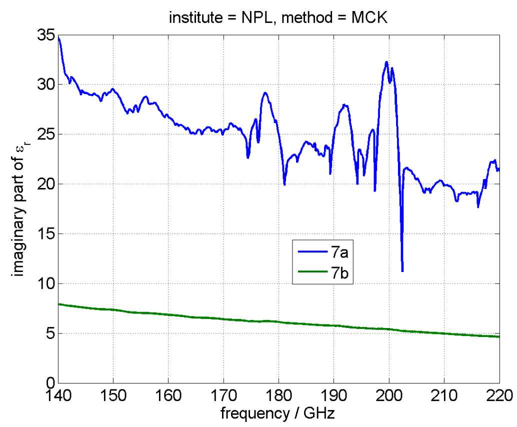

Figure 201: Material 7x (doped silicon), both samples measured by one institute.

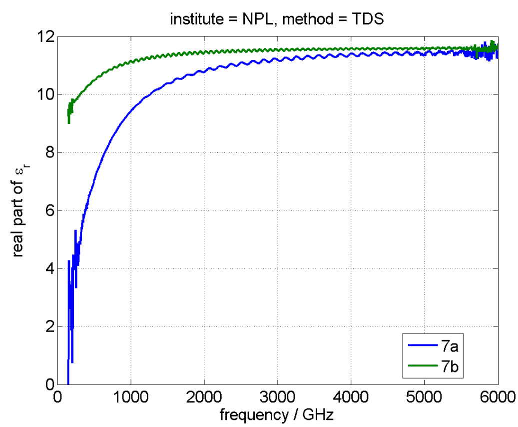

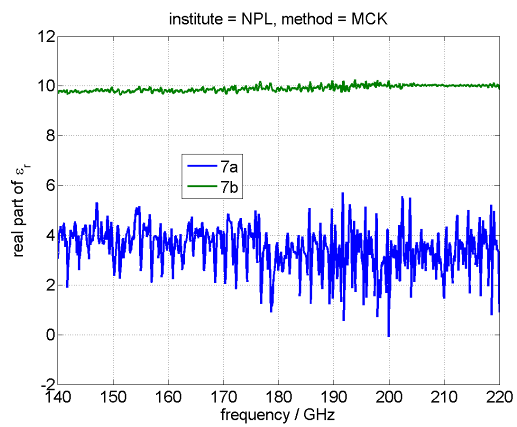

Figure 202: Material 7x (doped silicon), both samples measured by one institute.

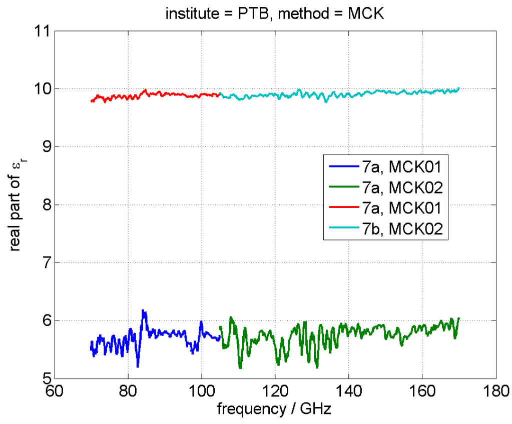

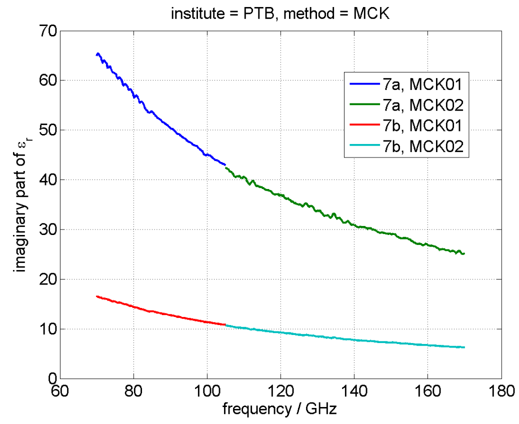

Figure 203: Material 7x (doped silicon), both samples measured by one institute.

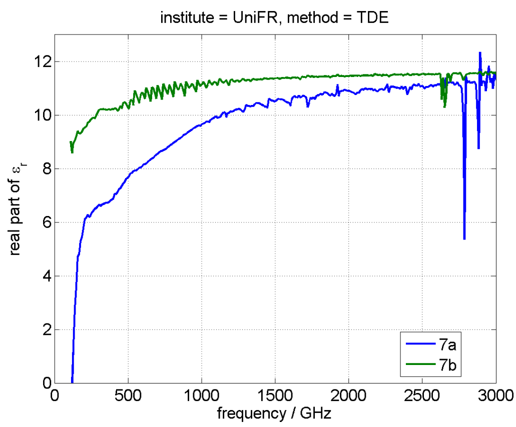

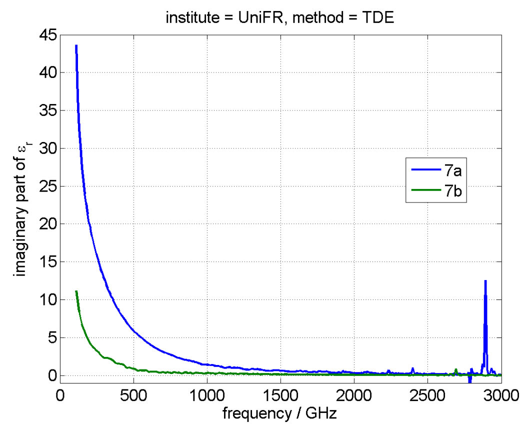

Figure 204: Material 7x (doped silicon), both samples measured by one institute.

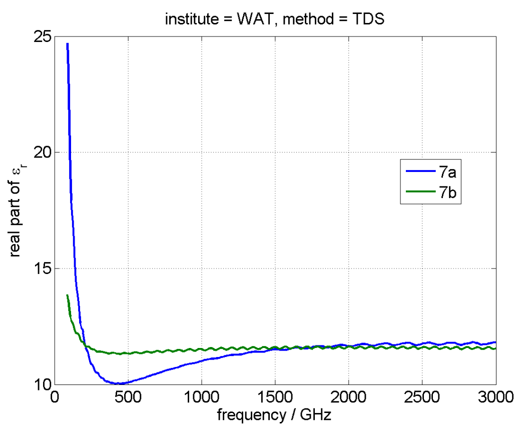

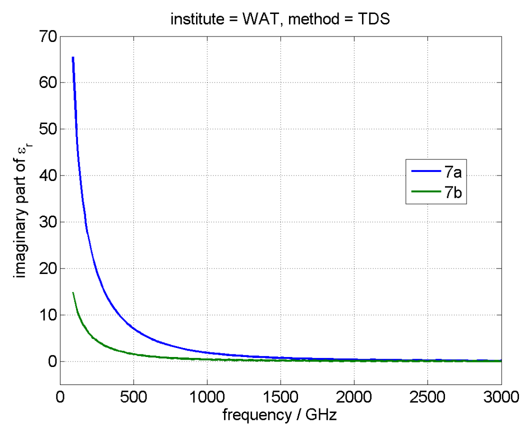

Figure 205: Material 7x (doped silicon), both samples measured by one institute.

6.5 Material AF32 Schott, both samples measured by one institute

This section shows a comparison of all AF32 Schott samples (material #8x, see Table 3) with different thicknesses.

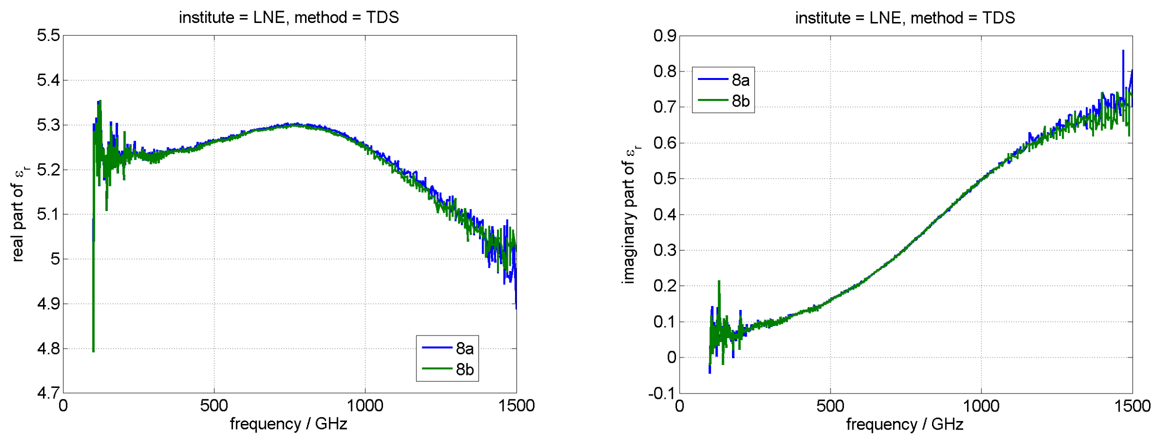

Figure 206: Material 8x (AF32 Schott glass), both samples measured by one institute.

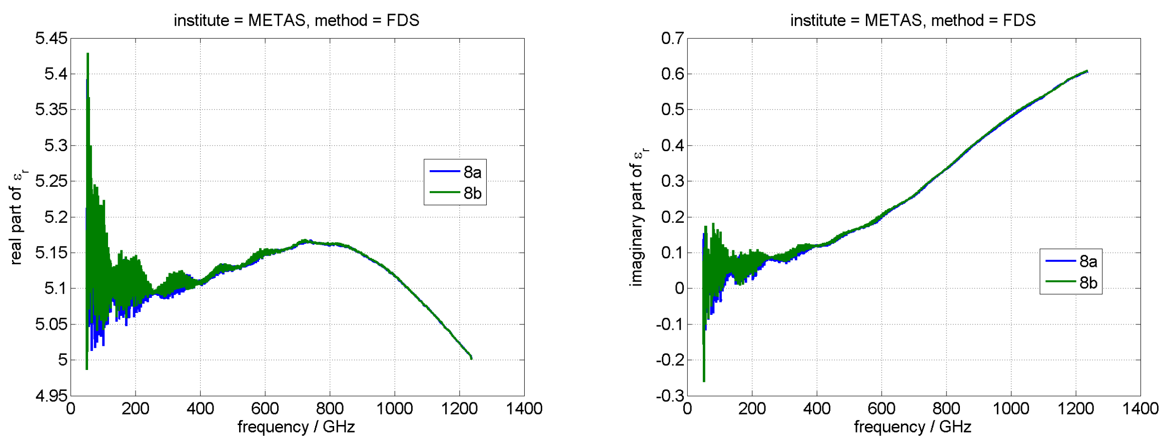

Figure 207: Material 8x (AF32 Schott glass), both samples measured by one institute.

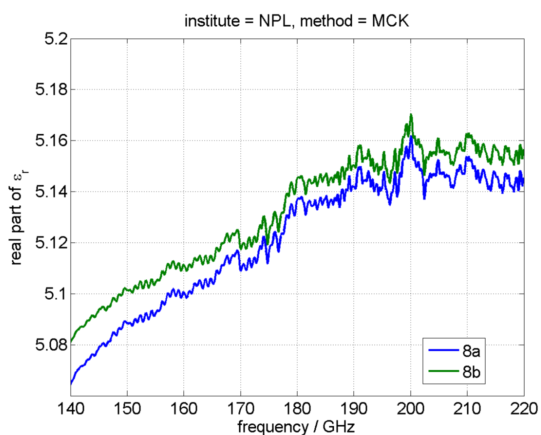

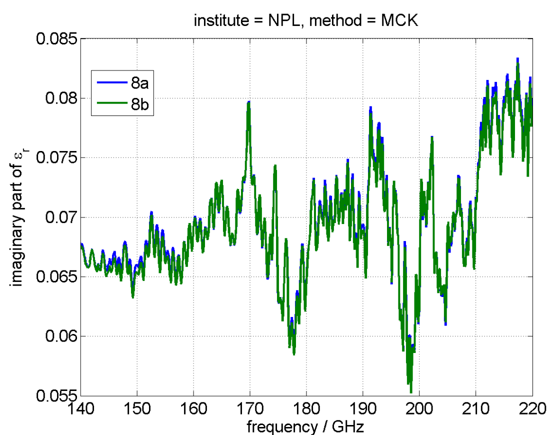

Figure 208: Material 8x (AF32 Schott glass), both samples measured by one institute.

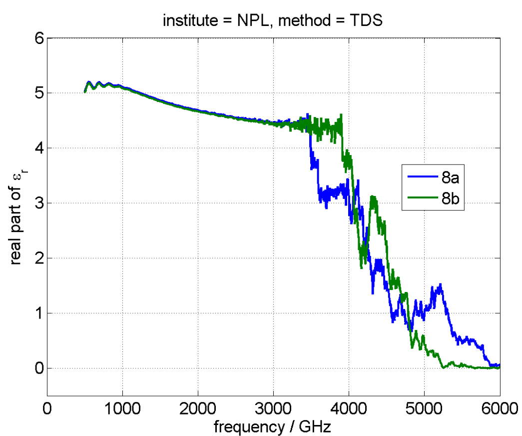

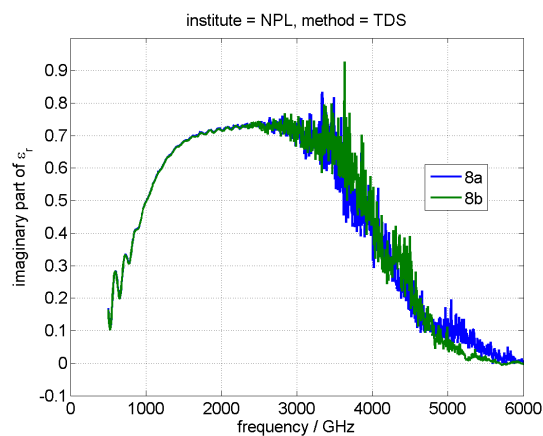

Figure 209: Material 8x (AF32 Schott glass), both samples measured by one institute.

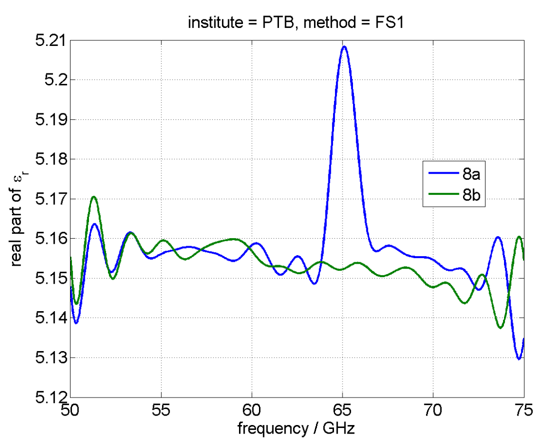

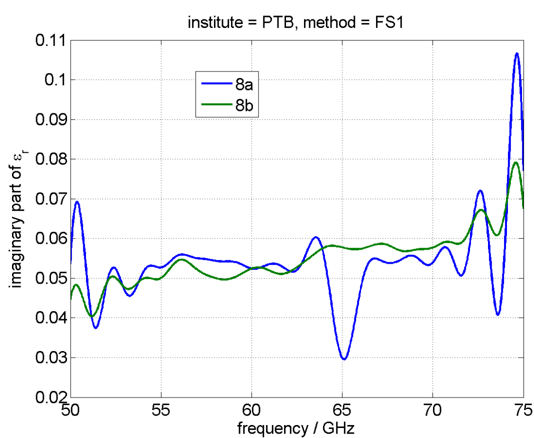

Figure 210: Material 8x (AF32 Schott glass), both samples measured by one institute.

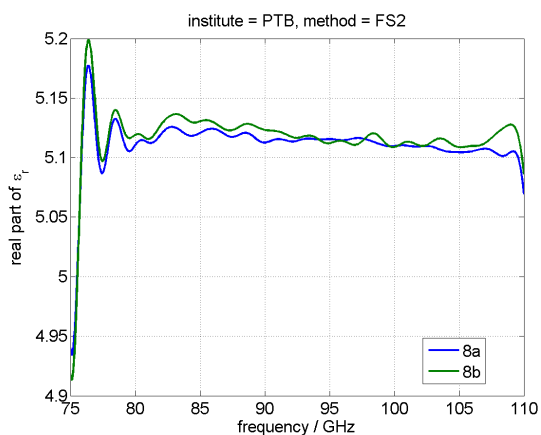

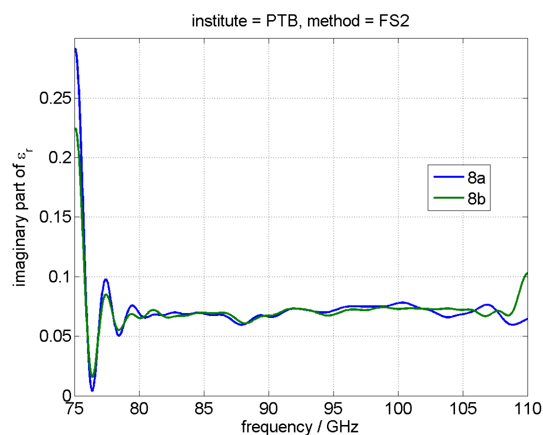

Figure 211: Material 8x (AF32 Schott glass), both samples measured by one institute.

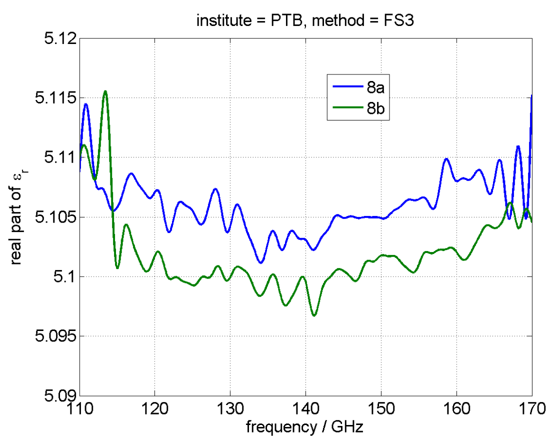

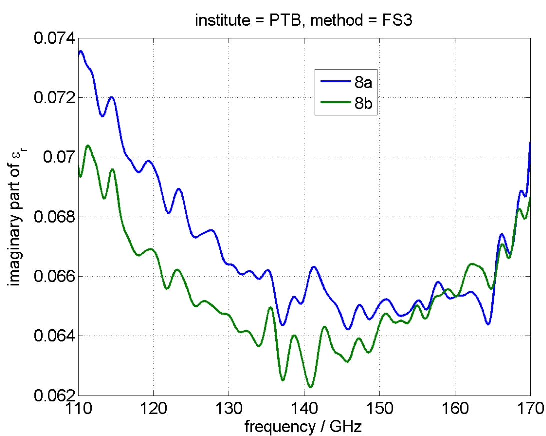

Figure 212: Material 8x (AF32 Schott glass), both samples measured by one institute.

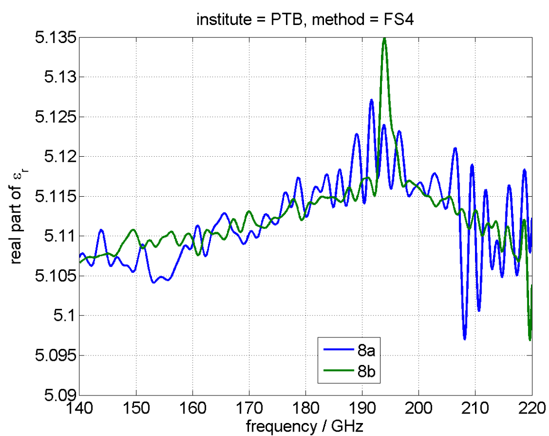

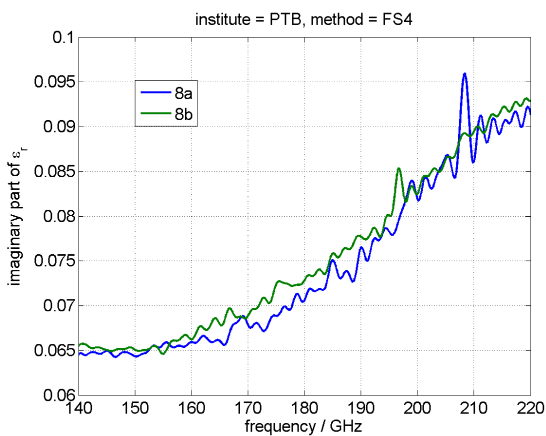

Figure 213: Material 8x (AF32 Schott glass), both samples measured by one institute.

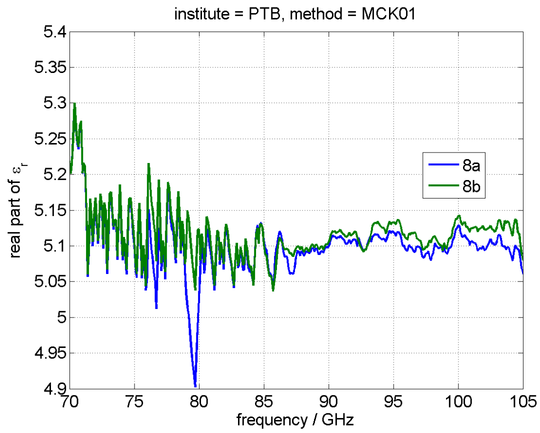

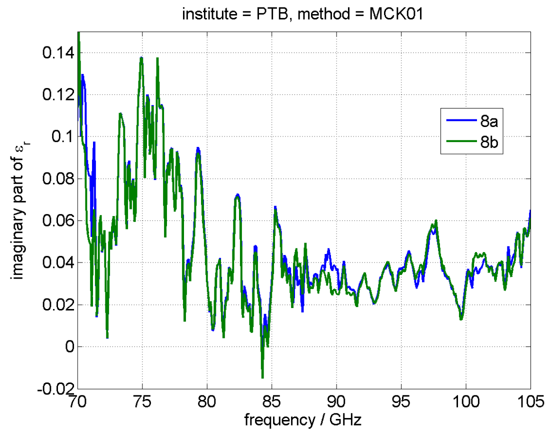

Figure 214: Material 8x (AF32 Schott glass), both samples measured by one institute.

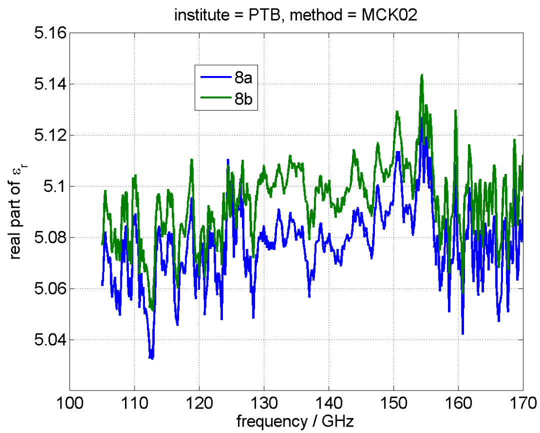

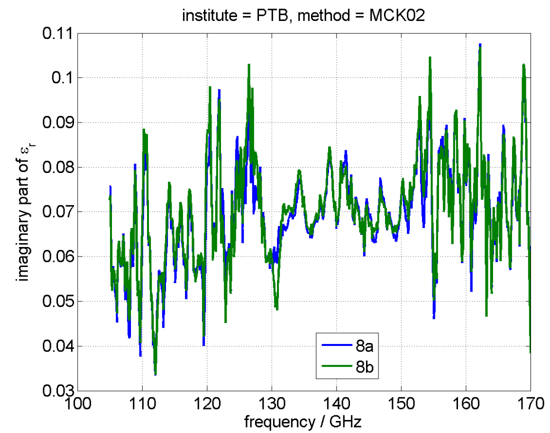

Figure 215: Material 8x (AF32 Schott glass), both samples measured by one institute.

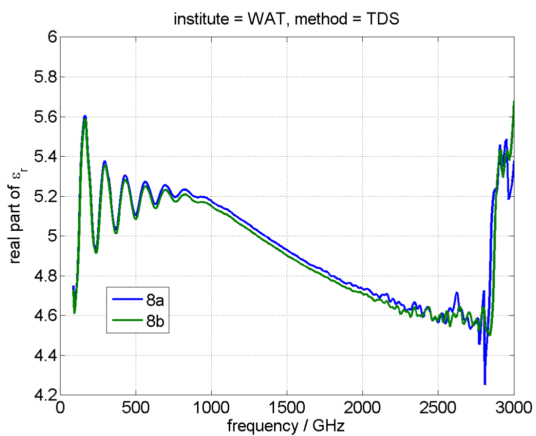

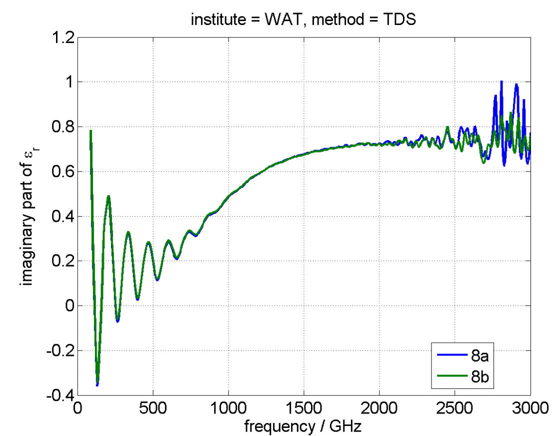

Figure 216: Material 8x (AF32 Schott glass), both samples measured by one institute.

6.6 Evaluation of measurement uncertainty

The measurement uncertainty evaluation procedure of particular partners is described in sections 5.1 to 5.8. Measurement uncertainty ($k = 2$) reported by institutes METAS (MCK) and NPL (open resonator) is given below in tabular form (constant value across the whole measured frequency range), see Table 5. The measurement uncertainty reported by institute PTB (free-space and MCK method) is variable and is given in form of graphs in Figure 217 to Figure 234 (only samples of the same material that have different thicknesses are plotted to see the influence of the thickness on the measurement uncertainty). Other participants of the comparison have not provided measurement uncertainty values.

Institute / Method	**Sample**	**U(re(ε_r'))**	**U(im(ε_r''))**
METAS / MCK (f = 500 - 750 GHz)	1	0.1	0.002
	2A1a	0.05	0.003
	2A2a	0.05	0.005
	2A2b	0.05	0.005
	2A3a	0.05	0.005
	3	0.07	0.03
	4	0.02	0.002
	5	0.1	0.005
	6a	0.025	0.0025
	6b	0.02	0.0015
	6d	0.025	0.0025
	7a	0.3	0.3
	7b	0.1	0.1
	8a	0.07	0.03
NPL / OR144 (f = 144 GHz)	2A2a	0.02	0.00049
	2A2b	0.01	0.00059
	2A3a	0.01	0.00040
	2A3b	0.02	0.00033
	6a	0.05	0.023
	6d	0.07	0.043
NPL / OR36 (f = 36 GHz)	2A1a	0.01	0.00092
	2A1b	0.01	0.00077
	5	0.04	0.13
	6a	0.03	0.0083
	6b	0.01	0.0018
	6d	0.02	0.0060

Table 5: Measurement uncertainty reported by participants for samples from Table 3.

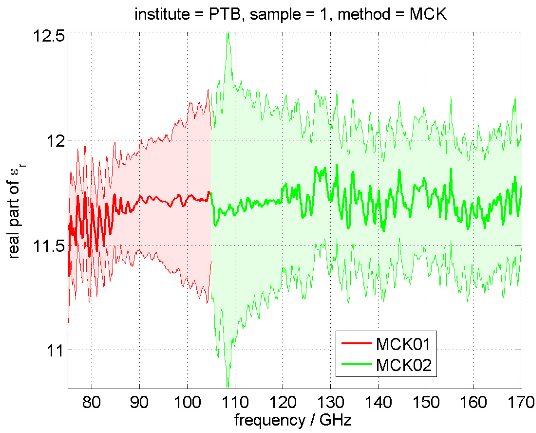

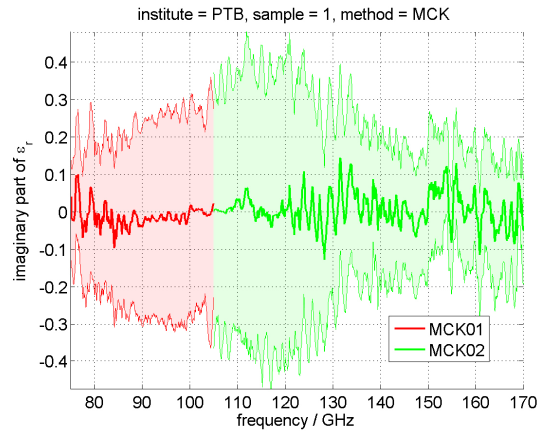

Figure 217: Sample 1 (high-resistivity silicon) measured by PTB, MCK method.

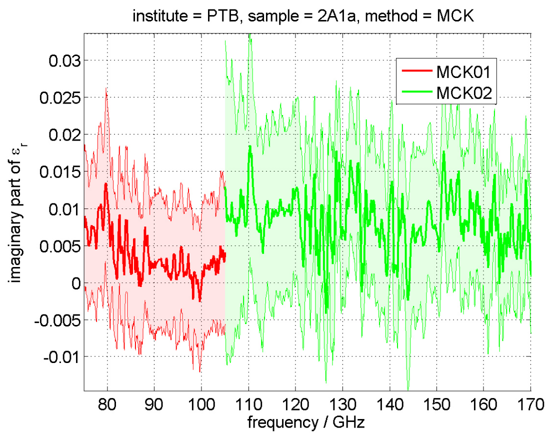

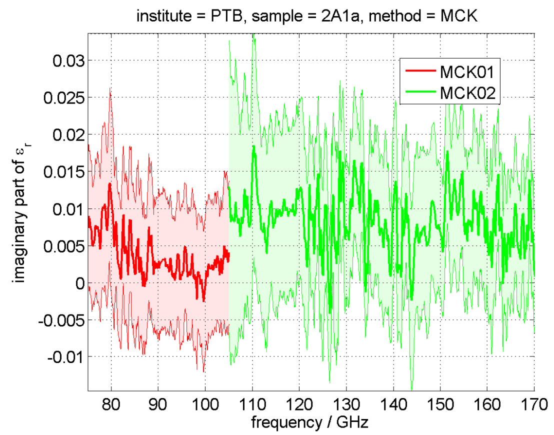

Figure 218: Sample 2A1a (Fused silica) measured by PTB, MCK method.

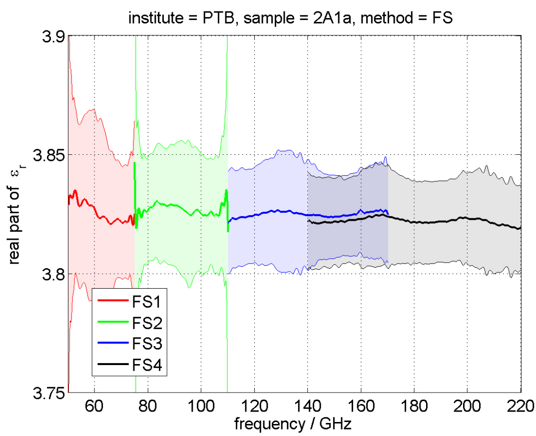

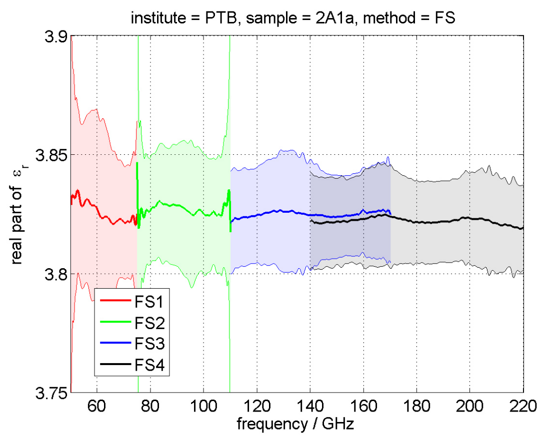

Figure 219: Sample 2A1a (Fused silica) measured by PTB, free-space method.

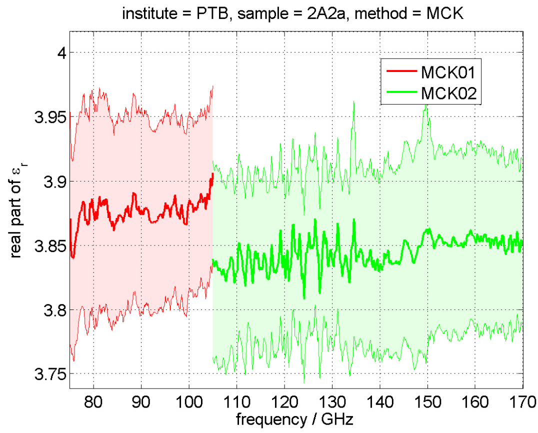

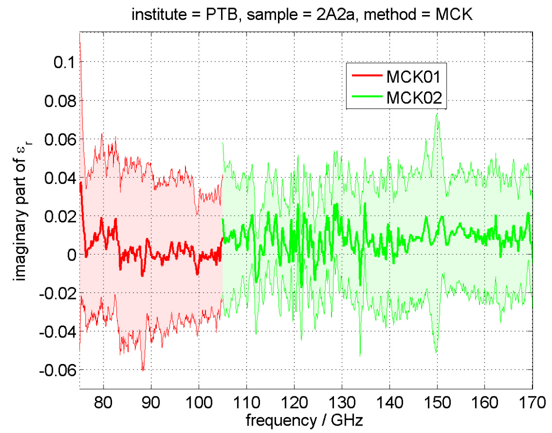

Figure 220: Sample 2A2a (Fused silica) measured by PTB, MCK method.

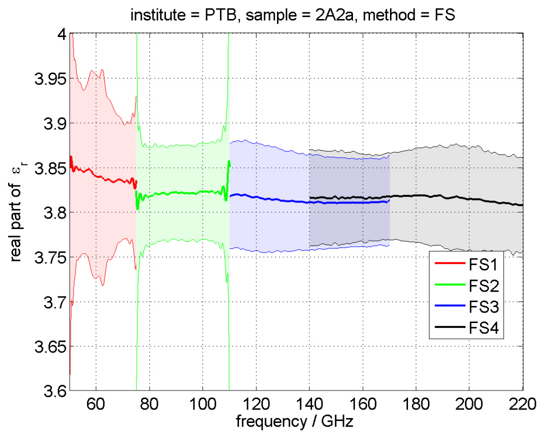

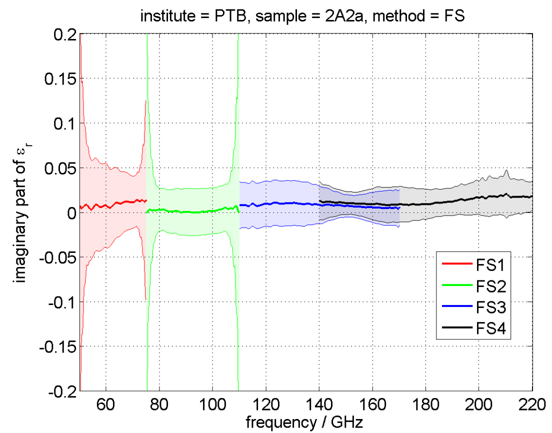

Figure 221: Sample 2A2a (Fused silica) measured by PTB, free-space method.

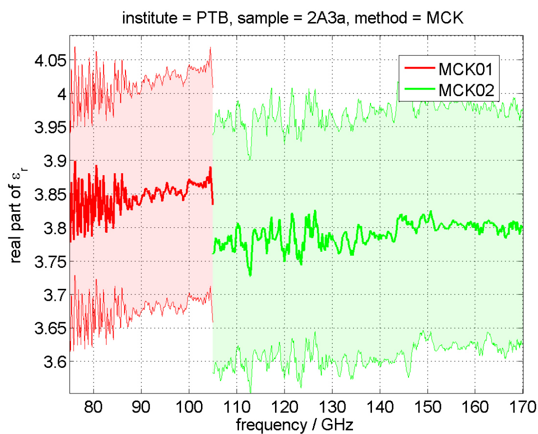

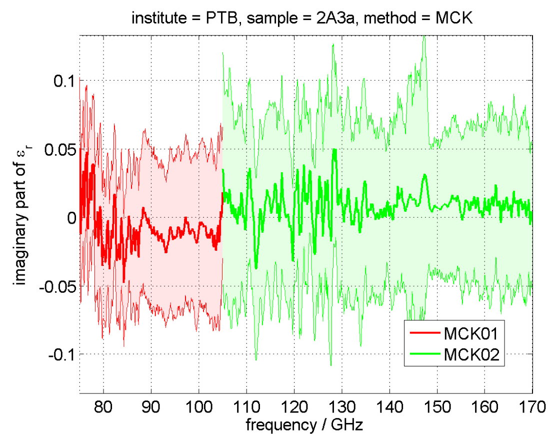

Figure 222: Sample 2A3a (Fused silica) measured by PTB, MCK method.

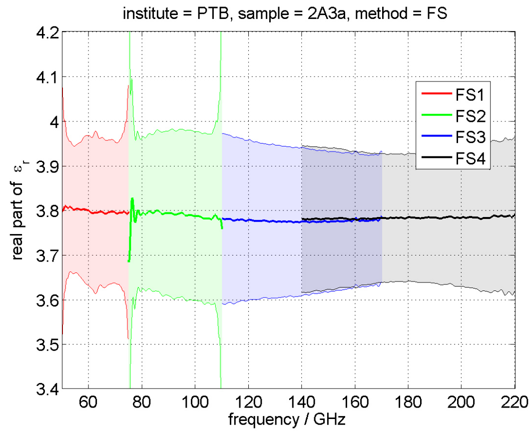

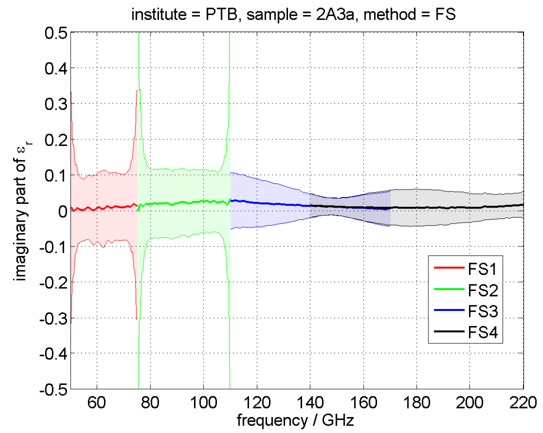

Figure 223: Sample 2A3a (Fused silica) measured by PTB, free-space method.

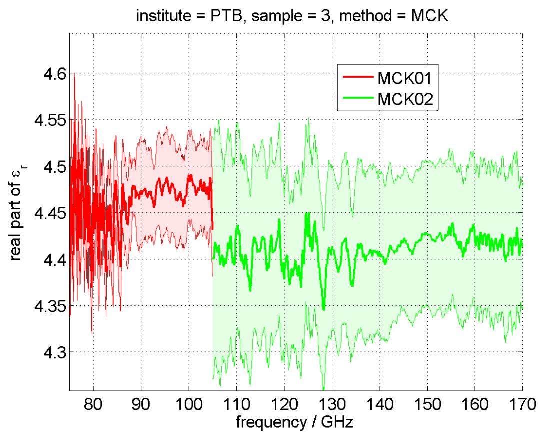

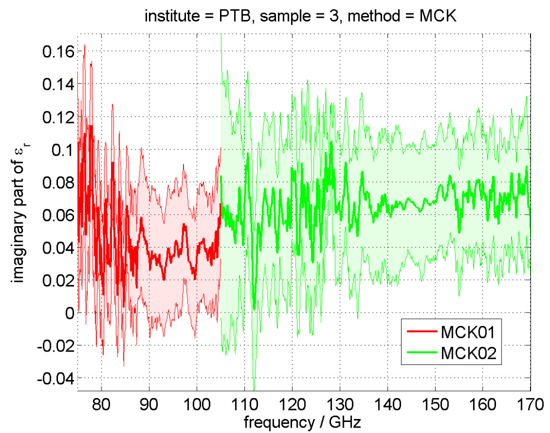

Figure 224: Sample 3 (borofloat) measured by PTB, MCK method.

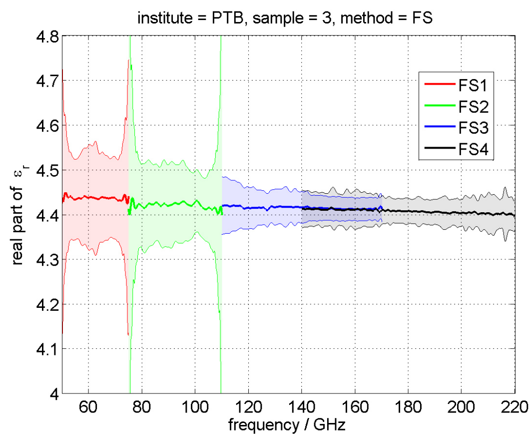

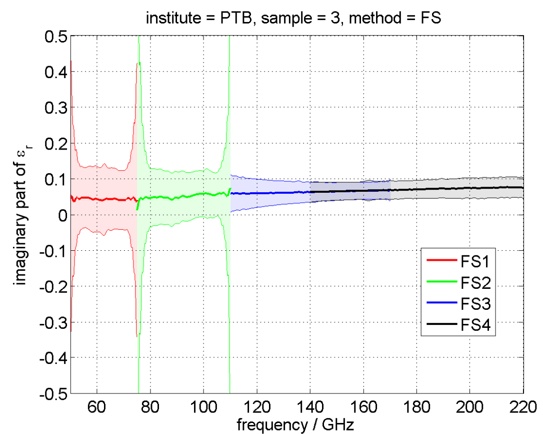

Figure 225: Sample 3 (borofloat) measured by PTB, free-space method.

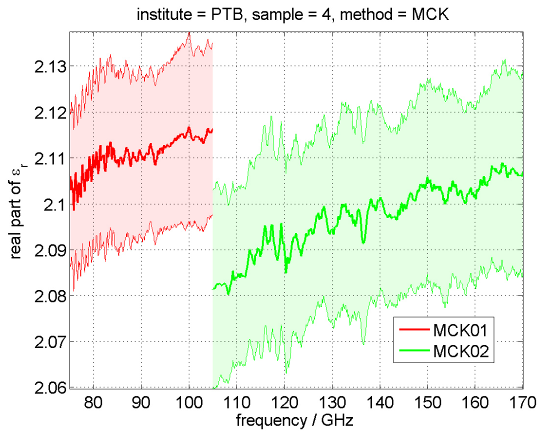

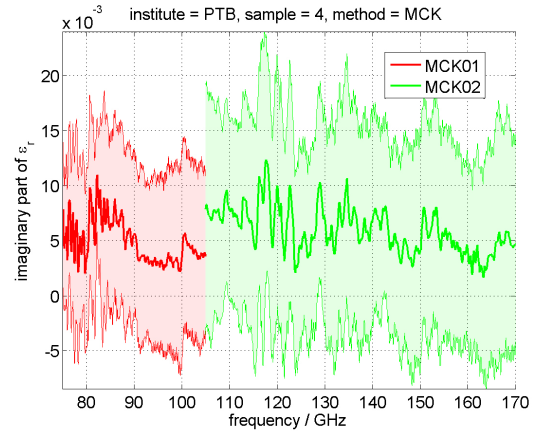

Figure 226: Sample 4 (TPX) measured by PTB, MCK method.

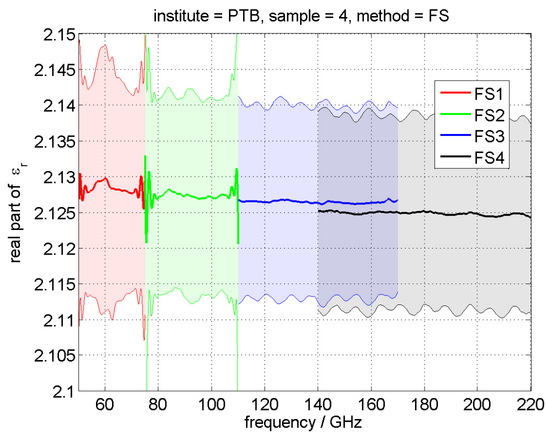

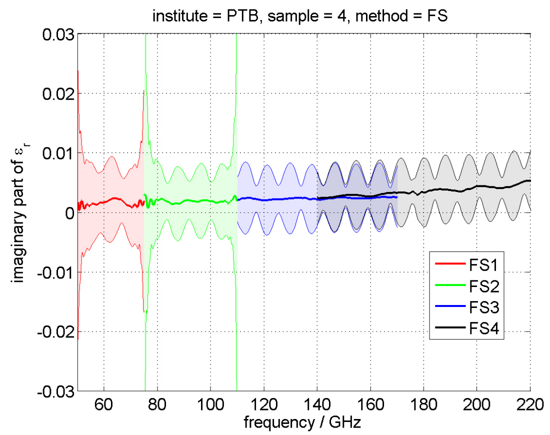

Figure 227: Sample 4 (TPX) measured by PTB, free-space method.

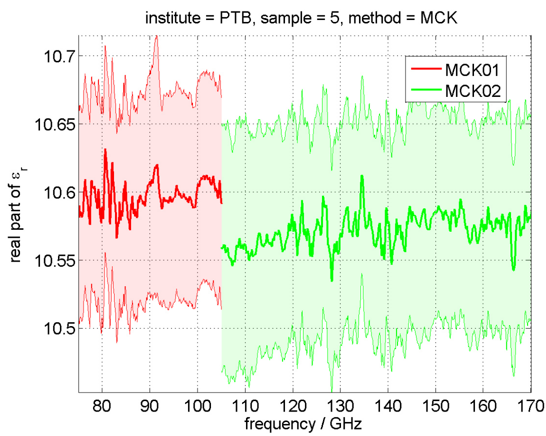

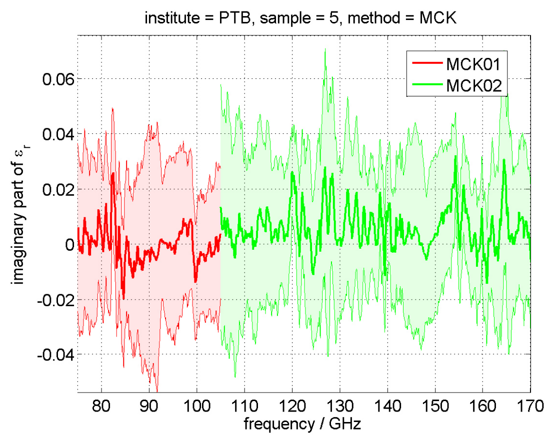

Figure 228: Sample 5 (YAG) measured by PTB, MCK method.

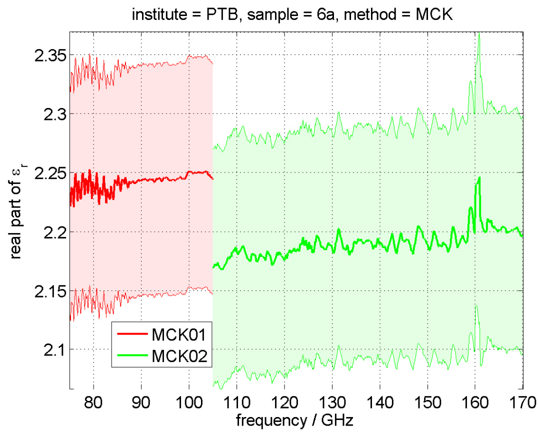

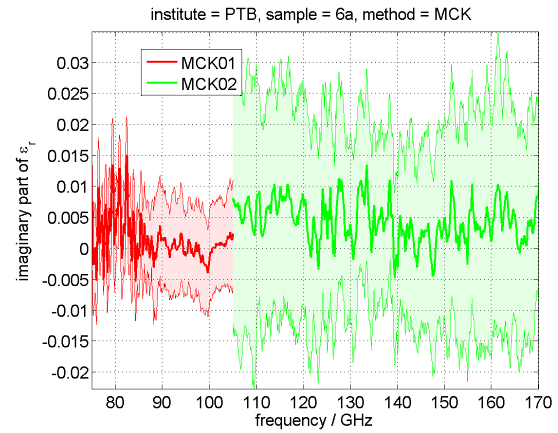

Figure 229: Sample 6a (UHMW polyethylene) measured by PTB, MCK method.

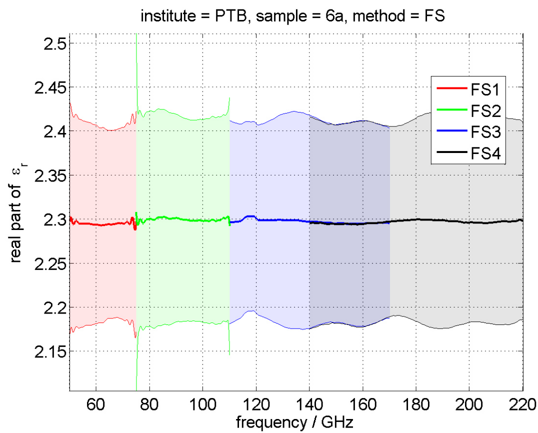

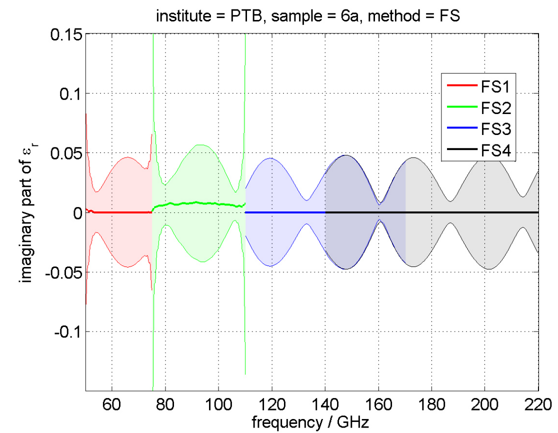

Figure 230: Sample 6a (UHMW polyethylene) measured by PTB, free-space method.

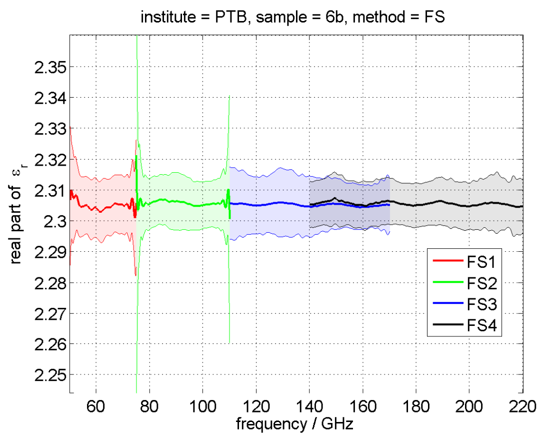

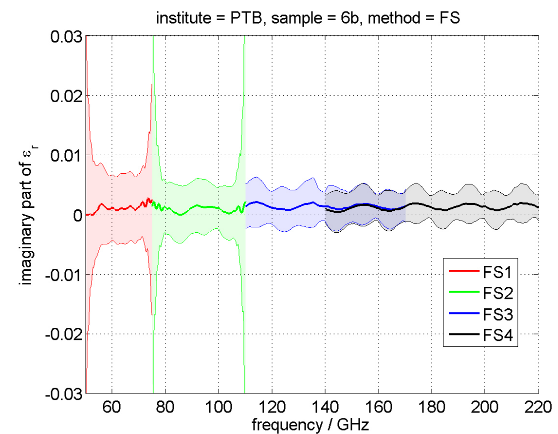

Figure 231: Sample 6b (UHMW polyethylene) measured by PTB, free-space method.

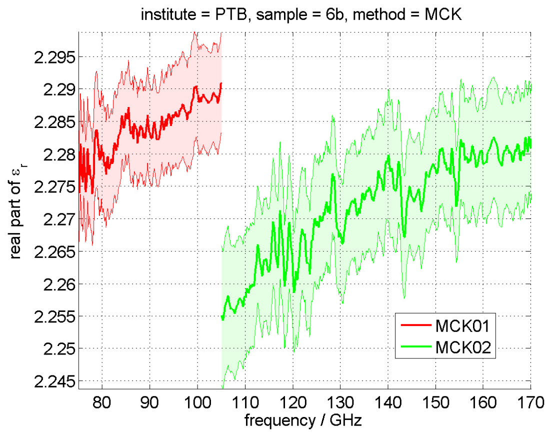

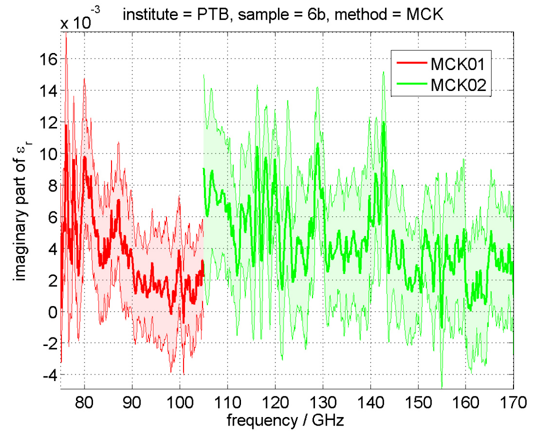

Figure 232: Sample 6b (UHMW polyethylene) measured by PTB, MCK method.

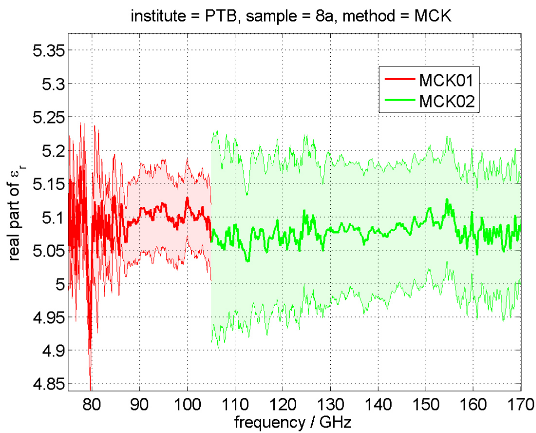

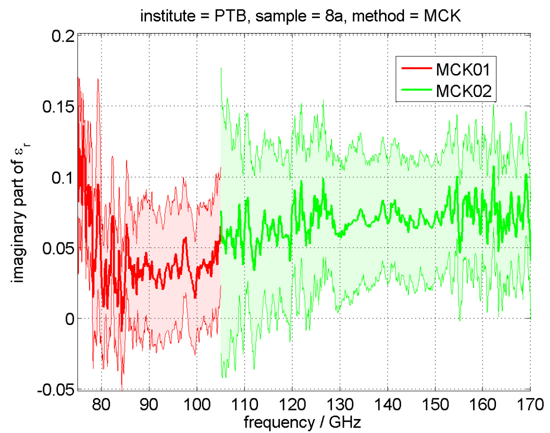

Figure 233: Sample 8a (AF32 Schott) measured by PTB, MCK method.

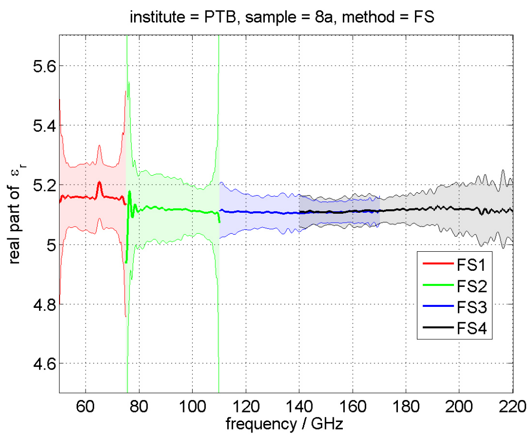

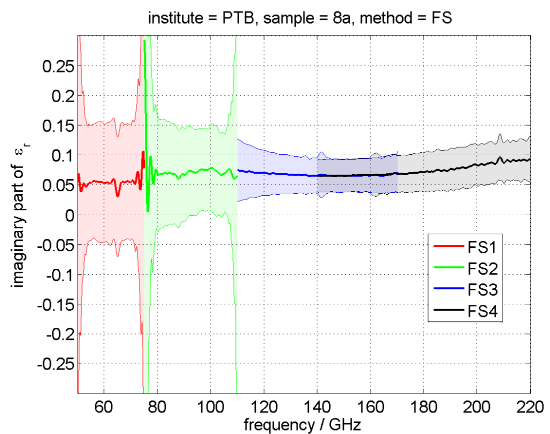

Figure 234: Sample 8a (AF32 Schott) measured by PTB, free-space method.

7 Discussion

Several samples from various materials (low-loss, lossy, thick, thin etc.) have been measured. The aim was to provide a comprehensive comparison between different set-ups and different parameter-extraction techniques over a very wide frequency band. From the complex transmission data and the previously determined specimen thickness values, the material parameters have been extracted via different methods for all materials. This is to get the complex refractive index and absorption coefficient, or alternatively, the real and imaginary part of permittivity. Results of the same batch of studied materials with different thicknesses (#2 Fused silica, #6 UHMW, #8 Schott-Glass) can help to find possible systematic errors in the setup calibration and extraction techniques, as well as the sensitivity, linearity and dynamic-range/noise limits of each set-up. For instance, the MCK measurements of Fused Silica (from the same batch, but with different thicknesses) show the reliability and consistency of the calibration techniques as well as parameter-extraction methods, see the graphs in Section 6.2. A good general agreement between different participants has been observed for many samples. However, for some materials like doped silicon, or very low loss samples like thin high-resistivity silicon and UHMW, the deviations are more visible. It is expected to get better results by applying better calibration methods and more "adapted" parameter-extraction techniques.

Acknowledgement

This work was supported by the 18SIB09 TEMMT (Traceability for Electrical Measurement at Millimeter-Wave and Terahertz Frequencies for Communications and Electronics Technologies) Project. TEMMT has received funding from the European Metrology Programme for Innovation and Research (EMPIR) Programme co-financed by the Participating States and from the European Union's Horizon 2020 Research and Innovation Programme.

References

[1] "Traceability for electrical measurements at millimetre-wave and terahertz frequencies for communications and electronics technologies (TEMMT)," http://projects.lne.eu/jrp-temmt/, Accessed: 2022-03-20.

[2] J. Baker-Jarvis, M. D. Janezic, J. H. Grosvenor, and F. G. Geyer, "Transmission/Reflection and Short-Circuit Line Methods for Measuring Permittivity and Permeability," NIST Technical Note 1355, 1992.

[3] J. Baker-Jarvis, E. J. Vanzura, and W. A. Kissick, "Improved technique for determining complex permittivity with the transmission/reflection method," *IEEE Trans. Microwave Theory Tech.*, vol. 38, no. 8, pp. 1096–1103, 1990.

[4] A.-H. Boughriet, C. Legrand, and A. Chapoton, "Noniterative stable transmission/reflection method for low-loss material complex permittivity determination," *IEEE Trans. Microwave Theory Tech.*, vol. 45, no. 1, pp. 52–57, 1997.

[5] A. Kazemipour, M. Hudlička, S.-K. Yee, M. A. Salhi, D. Allal, T. Kleine-Ostmann, and T. Schrader, "Design and calibration of a compact quasi-optical system for material characterization in millimeter/submillimeter wave domain," *IEEE Trans. Instrum. Meas.*, vol. 64, no. 6, pp. 1438–1445, 2015.

[6] A. Kazemiour, M. Wollensack, J. Hoffmann, M. Hudlicka, S.-K. Yee, J. Ruefenacht, D. Stalder, G. Gaeumann, and M. Zeier, "Analytical Uncertainty Evaluation of Mater-

ial Parameter Measurements at THz Frequencies," *J. Infrared Milli Terahz Waves*, vol. 49, pp. 1199–1217, 2020.

[7] Y. Wang, X. Shang, N. M. Ridler, T. Huang, and W. Wu, "Characterization of Dielectric Materials at WR-15 Band (50–75 GHz) Using VNA-Based Technique," *IEEE Trans. Instrum. Meas.*, vol. 69, no. 7, pp. 4930–4939, 2020.

[8] A. P. Gregory, "Q-factor Measurement by using a Vector Network Analyser," NPL Report MAT 58, 2021.

[9] R. G. Jones, "Precise dielectric measurements at 35 GHz using an open microwave resonator," *Proc. IEE*, vol. 123, no. 4, pp. 285—290, 1976.

[10] T. M. Hirvonen, P. Vainikainen, A. Lozowski, and A. V. Raisanen, "Measurement of dielectrics at 100 GHz with an open resonator connected to a network analyzer," *IEEE Trans. Instrum. Meas.*, vol. 45, no. 4, pp. 780–786, 1996.

[11] R. B. Marks, "A multiline method of network analyzer calibration," *IEEE Trans. Microwave Theory Tech.*, vol. 39, no. 7, pp. 1205–1215, 1991.

[12] D. C. DeGroot, J. A. Jargon, and R. B. Marks, "Multiline TRL revealed," in *60th ARFTG Conference Digest*, Washington, DC, USA, 2002, pp. 131–155.

[13] T. Nagashima and M. Hangyo, "Measurement of complex optical constants of a highly doped Si wafer using terahertz ellipsometry," *Appl. Phys. Lett.*, vol. 79, no. 24, pp. 3917–3919, 2001.

[14] P. Marsik, K. Sen, J. Khmaladze, M. Yazdi-Rizi, B. P. P. Mallett, and C. Bernhard, "Terahertz ellipsometry study of the soft mode behavior in ultrathin $SrTiO_3$ films," *Appl. Phys. Lett.*, vol. 108, pp. 052 901(1–5), 2016.

[15] B. P. P. Mallett, J. Khmaladze, P. Marsik, E. Perret, A. Cerreta, M. Orlita., N. Biškup, M. Varela, and C. Bernhard, "Granular superconductivity and magnetic-field-driven recovery of macroscopic coherence in a cuprate/manganite multilayer," *Phys. Rev. B*, vol. 94, p. 180503, 2016.

[16] K. Sen, P. Marsik, S. Das, E. Perret, R. de Andres Prada, A. Alberca, N. Biškup, M. Varela, and C. Bernhard, "Superconductivity and charge-carrier localization in ultrathin $La_{1.85}Sr_{0.15}CuO_4/La_2CuO_4$ bilayers," *Phys. Rev. B*, vol. 95, p. 214506, 2017.

[17] M. Yazdi-Rizi, P. Marsik, B. P. P. Mallett, K. Sen, A. Cerreta, A. Dubroka, M. Scigaj, F. Sanchez, G. Herranz, and C. Bernhard, "Infrared ellipsometry study of photogenerated charge carriers at the (001) and (110) surfaces of $SrTiO_3$ crystals and at the interface of the corresponding $LaAlO_3/SrTiO_3$ heterostructures," *Phys. Rev. B*, vol. 95, p. 195107, 2017.

[18] J. Humlicek and C. Bernhard, "Diffraction effects in infrared ellipsometry of conducting samples," *Thin Solid Films*, vol. 455-456, pp. 177–182, 2004.

[19] D. Ma, X. Shang, N. M. Ridler, and W. Wu, "Assessing the Impact of Data Filtering Techniques on Material Characterization at Millimeter-Wave Frequencies," *IEEE Trans. Instrum. Meas.*, vol. 70, no. 7, pp. 6 005 904(1–4), 2021.